

An Integrated Approach to Magnesium Hydroxide Use In Water and Wastewater Treatment

By

Nathaniel Barnes

Dissertation

Submitted to the Faculty of the
Graduate School of Vanderbilt University
in partial fulfillment of the requirements
for the degree of

DOCTOR OF PHILOSOPHY

in

Environmental Engineering

May 8, 2020

Nashville, Tennessee

Approved:

Alan Bowers, Ph.D.

Shihong Lin, Ph.D.

John Ayers, Ph.D.

Bridget Rogers, Ph.D.

Eugene LeBoeuf, Ph.D.

Copyright © 2020 by Nathaniel Barnes
All rights reserved

To my mother and father, for their endless compassion, tireless support, and unwavering belief in me. To sing the entirety of their praises would quadruple the length of this dissertation, but it is fair to say that without them, this entire enterprise would have devolved into a Sisyphean nightmare long ago.

ACKNOWLEDGMENTS

First and foremost, I would like to thank Dr. Alan Bowers for everything he has done to help me grow as a student, as an engineer, and as a person. His extraordinary knowledge of environmental chemistry never ceases to amaze me, nor does the the unfathomable depth of his patience. He has taught me a multitude of important things over the years, including that every tap, filter, pipe, and pump in the world should have his phone number on it, just in case.

I would also like to thank Premier Magnesia for its support of this research and the valuable insights its personnel provided into the industry. Special thanks belong to Matt Madolora for being an exceptionally friendly and valuable point of contact.

Lastly, I would like to express my sincere gratitude to everyone else who supported me on this endeavor. Friends, family, proofreaders (though I repeat myself), committee members, lab staff, fellow students, commiserating acquaintances, cooks in 24-hour restaurants, coffee, and all who constitute Vanderbilt University—I am forever grateful.

TABLE OF CONTENTS

	Page
COPYRIGHT	ii
DEDICATION	iii
ACKNOWLEDGMENTS	iv
LIST OF TABLES	vii
LIST OF FIGURES	x
CHAPTERS	
1 Introduction	1
1.1 Common Additives for pH and Alkalinity Control	1
1.2 Overview of Magnesium Hydroxide	2
2 A Probabilistic Approach to Modeling Struvite Precipitation with Uncertain Equilibrium Parameters	8
2.1 Chapter Summary	8
2.2 Introduction	8
2.3 Chemistry of Struvite Precipitation	11
2.4 Monte Carlo Model	16
2.5 Methods	25
2.6 Results	27
2.7 Conclusions	31
3 The Struvite Precipitation Index: A Practical Framework for Predicting Struvite Supersaturation in Water and Wastewater	33
3.1 Chapter Summary	33
3.2 Introduction	33
3.3 Uncertainty	35
3.4 Precipitation Potential	35
3.5 Equilibrium Chemistry	37
3.6 Methods	44

3.7	Laboratory Results	54
3.8	Precipitation in Field	65
3.9	Conclusions	69
4	Empirical Model for the Dissolution of Magnesium Hydroxide Slurries in Water and Wastewater Treatment	70
4.1	Introduction	70
4.2	Experimental Methods	81
4.3	Field Experiments	85
4.4	Selecting and Characterizing a Representative Slurry	86
4.5	Formulation of Kinetic Model	108
4.6	Lab and Computational Results	115
4.7	Field Results and Discussion	126
4.8	Kinetic Model Conclusions	134
5	Conclusions	135
	REFERENCES	137

LIST OF TABLES

Table		Page
1.1	Table of comparison between common sources of alkalinity used in municipal water and wastewater treatment. The hazard column was drawn from the safety data sheet (SDS) for brands common in the industry; however, these hazards may vary by manufacturer and concentration. If the SDS contained any hazard statements in the GHS Label elements, this component is marked “yes”. For the solids column, “S” represents the promotion of struvite formation and “C” represents the promotion of calcium carbonate formation as boiler scale due to an increase in constituent concentrations. Some of these additives may produce struvite, calcium carbonate, or other precipitates by creating localized zones of high pH; the additives that are most susceptible to this occurrence are labeled with a “Z”.	2
1.2	Comparison of properties between caustic, lime, and magnesium hydroxide slurries used in water and wastewater treatment (Shand, 2006). Values may vary between manufacturers, and the reported properties for each slurry are approximates. Note: Solubility is as the neat product, i.e. pH 14.0, 12.5, and 10.5 for NaOH, Ca(OH) ₂ , and Mg(OH) ₂ , respectively.	5
1.3	Results of a cost analysis for magnesium hydroxide and sodium hydroxide. The current Mg(OH) ₂ cost was taken as the price paid at each of the treatment plants used for case studies in this research (as of March 2020). The NaOH costs were estimated using 26 different bids from nine different suppliers given to treatment plants across the United States between 2017 and 2020. These estimates were calculated for the most common 50% NaOH solutions (as 25% NaOH is less economical). Note: the values in this table are subject to change and should only be used to gain a qualitative view of the current state of the industry.	5
2.1	Equilibrium constants from selected peer-reviewed sources and their respective characteristic values at 25 °C and $I = 0$. Values in the “Count” column are the number of constants included in the analysis that were reported for 25 °C and $I = 0$ and the number in the parentheses is the number of total values used in the analysis at all temperatures and ionic strengths. Data taken from IUPAC (2011); Goldberg et al. (2002); Hanhoun et al. (2011); Ohlinger et al. (1998); Linder & Little (1985). IUPAC (2011) and Goldberg et al. (2002) consists of a database using many peer-reviewed sources.	17
2.2	Number of published values of pK_{a2P} within given ranges of temperature (°C) and ionic strength ($M^{0.5}$).	17

2.3	Coefficients for the quadratic (Q) or linear (L) fits of each equilibrium constant and their associated R^2	20
2.4	Summary of 44 samples taken at the aeration basin influent (coupon set 1) over the two-week trial period. Note: seven more sets of data were collected at the other coupon locations.	30
3.1	Regression results for linear fixed effects model of measured $StrPI^*$ values described in Eq. (3.37). The p -value is calculated for a null hypothesis where the coefficient is equal to zero. Coefficients a and b apply to the binary I_x and G_x data, not I or G , and thus should not be used to estimate functionality. Instead, the estimates simply compare the change in $StrPI^*$ when I or G vary between their max and min values.	59
4.1	Published studies relevant to the dissolution kinetics, hydration kinetics, or surface chemistry of $Mg(OH)_2$ and MgO (in different forms). To date, no kinetic models have been published for commercial-grade $Mg(OH)_2$ slurry dissolution, and existing kinetic studies for other magnesia products are rarely performed in conditions relevant to water and wastewater treatment.	73
4.2	Fitted parameters for the fifth-order polynomial fit of the particle surface area analysis for four different magnesia slurries. All four equations follow the format: $A_{frac}(t) = p_1 \cdot FM(t)^5 + p_2 \cdot FM(t)^4 + p_3 \cdot FM(t)^3 + p_4 \cdot FM(t)^2 + p_5 \cdot FM(t) + p_6$. This fit was selected because it was the smallest order polynomial that sufficiently fit the data (especially at the boundary conditions). These fits are not an expansion of theory; rather, they are an efficient means of communicating slurry morphology information for use in future predictions.	106
4.3	The 14 synthetic wastewater scenarios used to calibrate and evaluate the model. These were run in triplicate in sealed beakers. The pH response of each scenario is shown in one of four succeeding figures, as indicated. The initial pH, magnesium dose, initial dissolved magnesium, and total dissolved inorganic carbon are given by pH_0 , Mg_a , Mg_0 , and C_T , respectively.	118
4.4	The fitted model parameters and approximate 95% confidence intervals calculated using a generic Monte Carlo simulation of residuals.	125
4.5	Approximate correlation matrix for the fitted parameters	126

4.6 Model parameters and predictions for the maximum and minimum dosages during Test 1 at the Chesapeake Bay treatment plant. Specifically, the left portion of the table reports initial conditions and the right portion shows the amount of time predicted to achieve different percentages of slurry dissolution. After slurry addition, the anoxic “plug-flow” collection system took approximately 280 minutes to reach the plant, resulting in a model prediction of between 97 and 83% slurry dissolution at the end of the pipe (depending on the sewage flow rate). Initial water conditions at the addition point were taken at the beginning of the 22-hour period. 128

4.7 Model parameters and predictions for the maximum and minimum dosages during Test 2 at the Chesapeake Bay treatment plant. Specifically, the left portion of the table reports initial conditions and the right portion shows the amount of time predicted to achieve different percentages of slurry dissolution. Note: After slurry addition, the anoxic “plug-flow” collection system took approximately 280 minutes to reach the plant, resulting in a model prediction of between 100 and 94% slurry dissolution at the end of the pipe. 130

4.8 Measured initial properties and magnesium dose for the jar tests of low-alkalinity North Carolina lake water (drinking water source). Note, initial pH was not altered from its original state. Slr_a represents the volume of slurry added to accomplish the dosage prescribed by Mg_a 131

LIST OF FIGURES

Figure	Page	
2.1	Comparison between published pK_{a_2P} values and the values generated by the quadratic fit at the same (T, I) pairs. The goodness-of-fit of the quadratic can be represented by the deviation of points from the line of perfect fit. Note: the cluster around a pK_{a_2P} of about 7.2 is a result of the high frequency in which the (T, I) pair of 25 °C and 0 M was reported in the literature.	19
2.2	Difference between published pK_{a_2P} values and the associated linear regression surface (residuals). The ‘count’ value represents the number of calculated residuals that fall within each bin.	21
2.3	Uniform distribution of regression residuals for pK_{a_2P} of phosphate. Probability is calculated such that the area under the curve is equal to 1.0.	22
2.4	Empirical distribution of regression residuals for pK_{a_2P} of phosphate.	23
2.5	Simplified flowchart of the Monte Carlo simulation.	24
2.6	Conditional solubility product predicted by the Monte Carlo model using both uniform and empirical distributions for the equilibrium constants. The discrete data points were taken from three prominent struvite studies that evaluated $K_{sp_{cond}}$ in the laboratory, and were included to lend credence to the model (Musvoto et al., 2000 ; Ohlinger et al., 2000). Note the lognormality of the vertical axis.	25
2.7	Omega values predicted by the Monte Carlo model using uniform (top) and empirical (bottom) distributions for the equilibrium constants. Mg_T , P_T , and N_T were set to 0.0013 M, 0.0046 M, and 0.0283 M, respectively; T = 25 °C, and I = 0.1M. The solid line represents the median value and the dashed lines are the 5th and 95th percentiles, leading to 90 percent confidence that precipitation will occur somewhere in Section B.	29
2.8	Omega values predicted at each point along the nitrification basin where a coupon was submerged, using an empirical distribution for the equilibrium constants. Mg_T , P_T , and N_T were input as lognormally distributed variables generated from the field sample concentrations; temperature and ionic strength were assumed constant at T = 25 °C and I = 0.1M. The central markers represent the median simulated Ω and the “error bars” represent the 5th and 95th percentiles at each distance, leading to 90 percent confidence that precipitation will occur between the two bars.	30

2.9	Uncertainty in final Ω (5%-95% envelope width) added by each equilibrium constant at pH 6, 7, and 8. For each bar, one constant was fixed at its regression surface value at $T = 25^\circ\text{C}$, and $I = 0.1\text{ M}$. Each value is compared to the Ω envelope at full uncertainty for that pH.	32
3.1	Median $pK_{sp_{cond}}$ predicted at 25°C and 0.1 M ionic strength by the uniform Monte Carlo model described in Barnes & Bowers (2017) . Curated datasets of nine published equilibrium parameters (K_{sp} , K_{a1P} , K_{a2P} , K_{a3P} , K_{a1N} , K_{1Mg} , K_{MgP} , K_{MgHP} , and K_{MgH2P}) were used to evaluate Eq. (3.6). The discrete data points used for comparison were taken from two prominent struvite studies that evaluated $K_{sp_{cond}}$ in the laboratory (Musvoto et al., 2000 ; Ohlinger et al., 2000).	41
3.2	Literature values for for the pK_{sp} of struvite from IUPAC (2011) , Hanhoun et al. (2011) , and Ohlinger et al. (1998) are plotted against their associated temperatures. The plotted data points were taken only from published constants measured in solutions of zero ionic strength, as such solutions are the most widely reported by a substantial margin (allowing for a larger dataset). Linear (solid line) and quadratic (dashed line) least-squares regressions had adjusted R-squared values of 0.131 and 0.257, respectively. Higher order polynomial regressions fit with similarly poor results. This degree of uncertainty in published pK_{sp} values precludes deeper insight into temperature functionality.	50
3.3	A schematic outlining the three phases of struvite formation (and accumulation) and their relative kinetic rates (Elimelech et al., 1998 ; Weber & DiGiano, 1996). The impactful wastewater properties are labeled for each phase.	51
3.4	Coupon fouled with struvite from field experiments. This specific coupon was submerged at a point 325 feet (99 meters) along a nitrification basin and removed after two weeks' contact time.	53
3.5	The calculated $StrPI^*$ vs. actual measured pH of precipitation for all synthetic struvite precipitation experiments included in the fixed effects model (77 points). The estimated bias, $intercept = 1.16$, and associated error bars were drawn from the synthetic experiments. Many of the data points are coincident or stratified as a result of identical duplicate pairs and the 0.10 unit resolution of pH measurements.	61
3.6	The normal probability plot of all measured $StrPI^*$ values generated from the synthetic precipitation experiments. The assumption of normality was supported by a one-sample Student's t-test ($\alpha = 0.05$).	62

3.7	The calculated $StrPI_c$ vs. measured pH of precipitation and associated error for all synthetic struvite precipitation experiments included in the fixed effects model (77 points). For (a), the calibration factor, C , is set to 0.90—two standard deviations below the least-squares estimate of C . This calibration was selected so there is 95% certainty that precipitation will occur when $StrPI_c > 0$ (reasonable for preventing precipitation). For (b), C is set to 1.42—two standard deviations above the least-squares estimate of C (reasonable for facilitating precipitation). Note, many of the data points are coincident or stratified as a result of the identical duplicate pairs and the 0.10 unit resolution of pH measurements.	64
3.8	The ratio of a calibrated StrPI model ($C = 1.16$) to an uncalibrated model ($C = 0$). On the upper subplot, the two $pK_{sp_{cond}}$ values were evaluated using the simplified $pK_{sp_{cond}}$ model outlined in Eq. (3.26) over the pH range of 6.5 to 8.5. This value is converted to the $K_{sp_{cond}}$ on the lower subplot.	65
3.9	Field results for eight coupons submerged along a 415-meter (1,360-ft) centrate nitrification basin, each evaluated for the existence of struvite precipitation. Temperature was 25 °C ($\pm 2^\circ\text{C}$). The dashed line denotes the expected point of precipitation for the calibrated model ($StrPI_c = 0$) using a C of 0.90 (empirical fit from lab experiments). Dotted lines denote a model confidence interval of \pm one standard deviation. The error bars depict the estimated range of the $StrPI_c$ over the two-week experiment, calculated using 10th and 90th percentile of measured pH, [Mg], [P], and [N] values. Both circular markers represent the $StrPI_c$ evaluated at the mean values of each set of pH, [Mg], [P], and [N]. . . .	67
4.1	Fraction of individual sulfide species versus solution pH. The gray area represents the pH range in typical sewers before magnesia is added.	72
4.2	A generalized form of the two-regime concept for the dissolution rate of a slurry dose (identical dose across all pHs). The morphology governed rate (Regime I) is not a function of pH, and is thus constant in this context. As this slurry dissolves and the surface area changes, this rate will not remain constant. Magnesium solubility, adjusted by an empirically fit exponential term (generally between 0 and 1), as represented by the dashed line, exerts more control over the initial slurry dissolution rate as the pH increases. In the transition region, usually between a solution pH of about 5.5 and 7.5, both regimes will contribute to the initial dissolution rate.	78
4.3	Mechanism for MgO hydration described in Amaral et al. (2011) ; Thomas et al. (2014) ; Stoltzenburg et al. (2015) ; Birchal et al. (2001) ; Rocha et al. (2004) . . .	81
4.4	Diagram of the modified Phipps and Bird jar test beaker used in the magnesium hydroxide dissolution experiments. The screw cap was opened to add reagents and take samples.	82

4.5	Oven analysis of bulk slurry. Temperatures of 105°C and 375°C were selected as they are slightly above the evaporation and dehydration temperatures of 100°C and 350°C, respectively.	92
4.6	Preliminary TGA for precipitated (homogeneous) particles (Slurry E). Note: As expected, the MgO core was found to be negligible when estimated using the method described in Equations 4.24 and 4.25 (in-house data).	93
4.7	Preliminary TGA for hydrated (layered) particles (Slurry A). Note: The fraction of dehydrated Mg(OH) ₂ was calculated using a 1:2.237 ratio by weight between water released and resulting MgO, as described in Equations 4.24 and 4.25. The tested solids were hydrated for one year (in-house data).	94
4.8	Preliminary diagram of particle dissolution. $r(0)$ is the initial radius of the full particle and $r(t)$ is the radius of the particle at time t . The density of each particle is represented by ρ , and is assumed homogeneous between particles and consistent as the particle dissolves. The total volume of the particle that has dissolved by time t is represented by $\Delta v(t)$. The total length of radius lost to dissolution over an elapsed period of time t is represented by $\Delta r(t)$	98
4.9	Measured percent volume by particle size for Slurry A. Values are binned log-normally.	101
4.10	Estimated surface area vs. the fraction of Slurry A that remains undissolved (normalized to 1 mol Mg(OH) ₂ added.) A fifth-degree polynomial was fit to the data to aid computational speed in modeling, shown as the gray line. Because the plots of the fitted and model data are nearly superimposed, the fitted line has been made bolder so it is visible. Note: The polynomial fit is simply an empirical method by which this slurry-specific data may be efficiently defined for use in the model; it is not an expansion of the underlying shrinking particle theory.	105
4.11	The fifth-order fitted polynomials for the characterization of the shrinking surface area of four different magnesia slurries alongside their underlying long-form model predictions. Again, less than about 0.001% of the variance of each remains unexplained, and the fits are near perfect. Because the plotted lines of the fitted and model data are nearly superimposed, the fitted lines have been made bolder so they are visible. Note: the polynomials are simply an empirical method by which to efficiently communicate this slurry-specific data; they are not an expansion of the underlying shrinking particle theory.	107
4.12	A conceptual outline of the dissolution model's computations. In summary, the MATLAB ode15s multistep (VSVO) solver is used to solve the system of first-order differential equations and calculate dissolved magnesium and total alkalinity after each variable time step.	114

4.13	The modeled (using values shown in Equation 4.6.1) and average measured pH responses to the addition of 3.2 mM (100 $\mu\text{L/L}$) of slurry to synthetic wastewater containing 8.3 mM of total carbon (0.7 g NaHCO_3/L) and no background magnesium, starting at different initial pH states. The slurries were mixed in a covered jar test beaker at a mean velocity gradient of 100 s^{-1} and an initial ionic strength of 0.01 M as NaCl.	119
4.14	The modeled (using values shown in Equation 4.6.1) and average measured pH responses to the addition of 3.2 mM (100 $\mu\text{L/L}$) of slurry to synthetic wastewater containing 16.7 mM of total carbon (1.4 g NaHCO_3/L) and no background magnesium, starting at different initial pH states. The slurries were mixed in a covered jar test beaker at a mean velocity gradient of 100 s^{-1} and an initial ionic strength of 0.01 M (as NaCl).	120
4.15	The modeled (using values shown in Equation 4.6.1) and average measured pH responses to the addition of 1.6 mM (50 $\mu\text{L/L}$) of slurry to synthetic wastewater containing 8.3 mM of total carbon (0.7 g NaHCO_3/L) and no background magnesium, starting at different initial pH states. The slurries were mixed in a covered jar test beaker at a mean velocity gradient of 100 s^{-1} and an initial ionic strength of 0.01 M (as NaCl).	121
4.16	The modeled (using values shown in Equation 4.6.1) and measured pH responses to the addition of 1.6 mM and 3.2 mM (100 and 50 $\mu\text{L/L}$, respectively) of slurry to synthetic wastewater containing 8.3 mM of total carbon (0.7 g NaHCO_3/L) and 5.0 mM of dissolved background magnesium, starting two different initial pH states. Magnesium concentrations in most treatment facilities are generally orders of magnitude less concentrated than this background dose, but even in the rare case that the concentrations are high and alkalinity is relatively low, such in Scenario N, background magnesium at these doses does not appear to have a significant effect on the equilibrium pH. Note: Scenario M appears to dissolve fully in the fast regime (surface saturation dominated), whereas Scenario N crosses into the slow regime (solution saturation dominated).	122
4.17	Subplot (a) shows the model (solid line) and average measured data (circles) for the pH response of Scenario K (3 total experiments, $pH_0 = 7.0$, $C_T = 8.3$ mM, $Mg_a = 1.6$ mM, and $Mg_0 = 0$ mM). The dashed line represents the expected equilibrium pH for the given slurry dose and water characteristics, i.e. at 100% dissolution. Subplot (b) shows the model (solid line) and the corresponding dissolved magnesium values as derived from the measured pH response data (white circles). The dashed line represents the total amount of magnesium added as $\text{Mg}(\text{OH})_2$. The red markers represent the measured undissolved magnesium at 40 minutes for each of the three experiments in the triplicate (two markers are superimposed at 0.84 and 0.85 mM). Subplot (c) contains the model values for the intermediate ϕ (black line) and ψ (blue line) terms.	123

- 4.18 Subplot (a) shows the model (solid line) and average measured data (circles) for the pH response of Scenario E (3 total experiments, $pH_0 = 7.5$, $C_T = 8.3$ mM, $Mg_a = 3.2$ mM, and $Mg_0 = 0$ mM). The dashed line represents the expected equilibrium pH for the given slurry dose and water characteristics, i.e. at 100% dissolution. Subplot (b) shows the model (solid line) and the corresponding dissolved magnesium values as derived from the measured pH response data (white circles). The dashed line represents the total amount of magnesium added as $Mg(OH)_2$. The red markers represent the measured undissolved magnesium at 40 minutes for each of the three experiments in the triplicate. Subplot (c) contains the model values for the intermediate ϕ (black line) and ψ (blue line) terms. 124
- 4.19 ICAP-MS measurements of magnesium for filtered and unfiltered samples for each Scenarios K and E triplicate, taken after 40 minutes of dissolution. Magnesium measured in filtered samples represents the mass of particles that have already dissolved by the 40-minute mark. Magnesium measured in unfiltered (and acidified) samples represents the accuracy of the initial slurry dosage. Data points that coincide with the blue 1:1 reference line have perfect agreement between measurements and predictions. Values from unfiltered samples that fall above 1.0 on the abscissa signify that the slurry was dosed at a higher concentration than intended. The outlier in the Scenario K filtered data may also be the result of filter failure. 125
- 4.20 Magnesium measurements (filtered and acidified vs. unfiltered and acidified) taken at the plant influent (collection system effluent) during Test 1. The 1:1 slope implies complete dissolution of the slurry. 127
- 4.21 Model predictions of the wastewater state over the 280 minute travel time in the collection system of the Chesapeake Bay treatment plant. The solid lines correspond to the left axis and depict model predictions of the percent of slurry still undissolved at time t . The dashed lines correspond to the right axis, and represent the predicted change in dissolved magnesium (ΔMg) as a function of time. The maximum and minimum values for both datasets represent an envelope of effective dosages caused by the variable flow rate in the sewer over the 22-hour experiment. 129
- 4.22 The model (solid line) and measured data (markers) for the pH response of Scenarios O-T run in sampled North Carolina lake water. In this case, the model was fit to all six data points. The pH data was not performed in triplicate and was taken every minute for the first 5 minutes (to better capture early pH functionality) and then once every 10 minutes after that. 132

4.23	The measured data (markers) for the pH response of Scenarios S and T run in sampled North Carolina lake water. The model (solid line) predicted the pH response of Scenarios S and T using parameters derived from only the Scenario O and P datasets (which use different slurry dosages than S and T). In other words, the model was fit using two jar test experiments and this fit was used to predict the results of two other jar test experiments. The pH data was not performed in triplicate and was taken every minute for the first 5 minutes (to better capture early pH functionality) and then once every 10 minutes after that.	133
5.1	Conceptual alkalinity (or pH) from the point of MgOH ₂ slurry addition to the plant effluent (with and without magnesia addition). Due to biological activity, alkalinity decreases in the sewer, aeration basins, and during nitrification/enhanced nutrient removal (ENR).	136

Chapter 1

Introduction

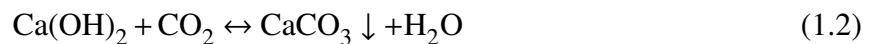
1.1 Common Additives for pH and Alkalinity Control

A variety of chemical additives are used in water and wastewater treatment for pH and alkalinity control. Typical additives to raise (or maintain) pH and alkalinity include caustic (NaOH), lime (CaO or Ca(OH)₂), sodium bicarbonate (NaHCO₃) and sodium carbonate (Na₂CO₃). Most commonly, NaOH or Ca(OH)₂ are used (Tchobanoglous et al., 2013).

However, many of these common additives hinder the performance or increase operating costs of downstream processes in the treatment plant. For example, the use of lime is often curtailed because it can cause temporary hardness that precipitates as calcium carbonate, which leads to nuisance boiler scale in drinking water. This calcium carbonate also forms additional inorganic solids for disposal in wastewater processes, especially as biodegradation occurs, or (Tchobanoglous et al., 2013; Hendricks, 2010):



and



where CaCO₃ ↓ indicates precipitation.

Further, most common additives rapidly supply their alkalinity after addition. While such immediate reactions can facilitate prompt modifications in operation, it also frequently requires alkalinity to be oversupplied in order to maintain optimal conditions over the course of the treatment regime. This can lead to an increase in chemical costs, odor production, and maintenance requirements. In other cases, the immediate increase in pH and alkalinity can cause localized consequences, including, for example, the precipitation of foulants such as struvite, MgNH₄PO₄ · 6H₂O, and

Alkalinity Source	Formula	Form	Hazard	Equivalence	Rate	Solids
Lime	CaO	Powder	Yes	2	Fast	C
Hydrated Lime	Ca(OH) ₂	Slurry	Yes	2	Fast	C
Sodium Hydroxide	NaOH	Aqueous	Yes	1	Instant	Z
Sodium Carbonate	Na ₂ CO ₃	Powder	Yes	2	Fast	Z
Sodium Bicarbonate	NaHCO ₃	Powder	Yes	1	Fast	Z
Magnesia	MgO	Powder	No	2	Slow	S
Hydrated Magnesia	Mg(OH) ₂	Slurry	No	2	Slow	S

Table 1.1: Table of comparison between common sources of alkalinity used in municipal water and wastewater treatment. The hazard column was drawn from the safety data sheet (SDS) for brands common in the industry; however, these hazards may vary by manufacturer and concentration. If the SDS contained any hazard statements in the GHS Label elements, this component is marked “yes”. For the solids column, “S” represents the promotion of struvite formation and “C” represents the promotion of calcium carbonate formation as boiler scale due to an increase in constituent concentrations. Some of these additives may produce struvite, calcium carbonate, or other precipitates by creating localized zones of high pH; the additives that are most susceptible to this occurrence are labeled with a “Z”.

vivianite, Fe₃(PO₄)₂, at the addition point or in transport and filtration systems (Benisch et al., 2000; Ohlinger et al., 1998; Mamais et al., 1994; Horenstein et al., 1990). Lastly, most common additives are supplied as concentrated and highly basic solutions, pellets, and suspensions. For plant operators, these hazardous additives raise safety concerns and may require additional training, equipment, worker compensation, transportation costs, and interaction with regulatory bodies. Table 1.1 provides a compilation and comparison of the basic properties of common alkalinity additives.

Although these costs and concerns may seem excessive to the outside observer, alkalinity control is essential to effective water and wastewater treatment, and additive selection is generally guided by identifying the least problematic choice. Consequently, as each of these common additives has been used for decades (and, in some cases, centuries), these problems will likely only be alleviated in the future by the introduction of new additives/processes.

1.2 Overview of Magnesium Hydroxide

The use of magnesium hydroxide slurries in water and wastewater treatment has recently attracted more attention due to pricing, increased availability, local sourcing, and the many process advantages these slurries have over the most common additives:

1. $\text{Mg}(\text{OH})_2$ adds permanent hardness, i.e., MgCO_3 is much more soluble than CaCO_3 , so there is no nuisance boiler scale or solids production in water or wastewater treatment (Lide, 1991).
2. Compared to caustic soda or lime, magnesium hydroxide is often preferred for treating acidic wastewater that is laden with industrial metals as it generally produces less sludge, which usually dewateres faster (Shand, 2006).
3. Compared to sodium, Na^+ , Mg^{2+} is a beneficial mineral with far fewer side effects, and is generally considered by health professionals to be an undersupplied nutrient for the majority of Americans (Rude et al., 2010a,b; Mason, 2011). In addition, Mg is a beneficial nutrient for bio-P uptake and anaerobic digestion of solids (Speece, 1996).
4. $\text{Mg}(\text{OH})_2$ can be added in excess (intentionally or accidentally) without accompanying pH spikes, as it is much less soluble than NaOH or $\text{Ca}(\text{OH})_2$. This gradual pH increase also produces more robust processes, as interruptions in additives have a less immediate effect on system pH (Shand, 2006).
5. The use of $\text{Mg}(\text{OH})_2$ provides a gradual increase in collection system alkalinity, which results in a more consistent elevated pH over several hours. An elevated pH (above 8.5) shifts the equilibrium of dissolved sulfides away from the corrosive and malodorous hydrogen sulfide, H_2S , and toward non-volatile bisulfide (HS^-). Combined with the nutritional supplementation of magnesium, this can lead to more effective odor and corrosion control in wastewater collection systems (Firer et al., 2008; Gutierrez et al., 2009; Talaiekhosani et al., 2016; Jensen, 1990). Further, alkalinity supplied in collection systems can carry over into treatment processes, where it maintains a more consistent influent pH and lowers total system costs.
6. $\text{Mg}(\text{OH})_2$ slurries are classified as non-hazardous and exhibit few to no safety concerns for workers. Similarly, as small chemical spills are relatively innocuous and abundant geologic/oceanic magnesium sources allow for sustainable mining and production practices, magnesia slurries have fewer environmental concerns than alternatives. This assessment

is further supported by the fact that milk of magnesia, the commercial form of $\text{Mg}(\text{OH})_2$, is consumed regularly by the public as a laxative and antacid. Though concentrations and secondary ingredients may differ between industrial and medicinal slurries, this familiarity may arouse less public contention than other additives have in the past.

7. When oversupplied, caustic soda and lime can raise solution pH to 14.0 and 12.5, respectively. Consequently, adding too much into a waste stream can be costly and damage treatment processes. Conversely, the low solubility and thermodynamic constraints of magnesia slurry prevent the pH of solutions from rising above 10.5. In practice, when magnesia is added to processes in excess, the pH limit is generally nearer to 9.0 and rarely exceeds pH 8.5 under normal operating conditions where acidic waste is neutralized. This means $\text{Mg}(\text{OH})_2$ inherently maintains an optimal pH for aerobic organic carbon removal and nitrification while it simultaneously prevents inadvertent pH spikes from destabilizing the biomass. Because the upper pH limit for water discharge to the environment prescribed by the 1976 Clean Water Act is also pH 9.0, this is especially significant.
8. If magnesium is supplied in excess in the collection system, it can persist throughout the treatment train and maintain an elevated pH where biological activity would otherwise lower it. Within nitrification processes, for example, 7.14 mg of alkalinity is consumed per mg of N oxidized. This saves money that would have otherwise been spent on an oversupply of another additive that has no beneficial downstream use.
9. The biological response to supplemental magnesium can have positive impacts on downstream systems. For example, it reduces biochemical oxygen demand (BOD) and generation of solids, which can result in reduced landfill costs and increased methane recovery. ([Talaiekhosravi et al., 2016](#)).
10. Although magnesia may reduce the production of nuisance precipitates by eliminating localized pH spikes around chemical addition points, an increase in dissolved magnesium can promote the recovery of struvite ($\text{MgNH}_4\text{PO}_4 \cdot 6\text{H}_2\text{O}$) as a high-value fertilizer or for

the sequestration of orthophosphates. This is particularly valuable where concentrations of magnesium are lower than those of ammonium and phosphate.

11. Magnesium hydroxide can neutralize more acid per pound than more conventional alkali additives. For example, it provides 27 and 37 percent more alkalinity than the same mass of caustic soda and hydrated lime, respectively (Shand, 2006). This results in lower transportation, storage, and pumping costs. See Table 1.2 for a more in-depth comparison. Subsequently, while raw material prices are subject to the bidding process and can vary between treatment plants, alkalinity from $Mg(OH)_2$ slurry is generally less expensive than NaOH. A price comparison of the two additives can be found in Table 1.3.

Table 1.2: Comparison of properties between caustic, lime, and magnesium hydroxide slurries used in water and wastewater treatment (Shand, 2006). Values may vary between manufacturers, and the reported properties for each slurry are approximates. Note: Solubility is as the neat product, i.e. pH 14.0, 12.5, and 10.5 for NaOH, $Ca(OH)_2$, and $Mg(OH)_2$, respectively.

Property	50% NaOH	30% $Ca(OH)_2$	63% $Mg(OH)_2$
% Hydroxide	42.5	45.9	58.3
Solubility in Water (g/100 ml)	42	0.185	0.0009
Reactive pH	14	12.5	9.0
Freezing Point ($^{\circ}F$)	61	32	32
Weight Equivalency	1.37	1.27	1

Table 1.3: Results of a cost analysis for magnesium hydroxide and sodium hydroxide. The current $Mg(OH)_2$ cost was taken as the price paid at each of the treatment plants used for case studies in this research (as of March 2020). The NaOH costs were estimated using 26 different bids from nine different suppliers given to treatment plants across the United States between 2017 and 2020. These estimates were calculated for the most common 50% NaOH solutions (as 25% NaOH is less economical). Note: the values in this table are subject to change and should only be used to gain a qualitative view of the current state of the industry.

$Mg(OH)_2$	NaOH		
	Price/lb alk	Mean price/lb of alk	Std. dev.
\$0.19	\$0.26	\$0.05	\$0.17 - \$0.33

12. Magnesia is by far the least hazardous of the commonly used alkalinity sources in municipal water and wastewater treatment. Per the Comprehensive Environmental Response, Com-

pensation, and Liability Act (CERCLA) and the subsequent Superfund Amendments and Reauthorization Act (SARA), it is not listed as a hazardous substance under 6NYCRR part 597, unlike the other additives in Table 1.1. This not only eliminates costs associated with worker safety and equipment but also eliminates the need for special containment walls, dikes, and special storage facilities. Large spills can be mitigated by shoveling/pumping the material and transporting it to a landfill, with no need of an environmental cleanup service. Since magnesium hydroxide is a weak base, it does not have an exothermic reaction when introduced to water. If it comes in contact with skin, it can simply be washed off.

There is a paucity of data and case studies documenting the performance of magnesia slurries as $\text{MgO}/\text{Mg}(\text{OH})_2$ have only recently gained acceptance for pH/alkalinity control. Moreover, the:

- absence of case studies and definitive kinetic/equilibrium models
- disagreement in published equilibrium constants (for example, where struvite is concerned)
- difference in manufacturing methods and slurry properties between magnesia suppliers
- effects of slurry aging and storage methods, and
- the perpetual variability of municipal water/wastewater compositions

instill significant levels of uncertainty into any comprehensive magnesia study.

Although the scientific literature of magnesium hydroxide is somewhat lacking in depth and breadth, that has not stopped many American municipalities, factories, and even several breweries from introducing it into their processes. This rapid acceptance has outpaced our understanding of the environmental and material chemistry associated with the use of magnesium hydroxide. Its adoption by more conservative plant operators and managers is impeded by this lack of research. Specifically, there are two areas where further exploration would likely elucidate discussions and eliminate concerns associate with magnesia use.

Firstly, as most wastewater streams exhibit relatively low concentrations of magnesium, the use of magnesia slurry and its associated rise in pH may increase the possibility of struvite

($\text{MgNH}_4\text{PO}_4 \cdot 6\text{H}_2\text{O}$) precipitation. Struvite is a nuisance precipitate that can cost plants hundreds of thousands of dollars every year in maintenance (Benisch et al., 2000) by fouling mixers, pipes, and other equipment with hard, pale crystals. When reclaimed, however, it can be useful in orthophosphate recovery, or even sold as a valuable fertilizer (Durrant et al., 1999). Unfortunately, the precipitation of struvite has not been modeled effectively, and not in a way that is accessible and useful to treatment plant operators. As a result, many municipalities have decided that avoiding magnesium altogether is the safer option. The first part of this research seeks to alleviate these concerns by developing an intuitive, calibratable model for struvite precipitation that is robust enough to handle the variability and uncertainty inherent in wastewater treatment.

The second reason that many treatment plant engineers have been reluctant to adopt magnesia slurries is that the slow dissolution of these slurries has not been adequately described. Simply put, a source of delayed release alkalinity is far more useful when its effects on downstream pH and alkalinity can be predicted and engineered. As a result, an effective magnesia slurry dissolution model would have immediate value for the growing industry.

This work examines $\text{Mg}(\text{OH})_2$ for use in water and wastewater treatment, evaluates and produces predictive models of struvite production, quantifies uncertainties emerging from both theoretical and practical sources, and models the kinetics of magnesia slurry dissolution. For each topic, models and insights were specifically tailored for efficient and robust application by engineers and operators in municipal treatment plants—an underrepresented but crucial facet of academic environmental research. This application-focused approach was accomplished by performing both lab experiments and case studies to produce simple, calibratable models.

Chapter 2

A Probabilistic Approach to Modeling Struvite Precipitation with Uncertain Equilibrium Parameters

2.1 Chapter Summary

The precipitation and accumulation of struvite ($MgNH_4PO_4 \cdot 6H_2O$) within anaerobic processes has been a costly problem for wastewater facilities. To anticipate and mitigate struvite buildup, solubility models have been developed that employ equilibria software for the evaluation of equilibrium equations. Unfortunately, these programs run under the assumption that chemical equilibrium constants are single, universally accepted values when, in reality, a wide range of values have been published for these constants.

In this study, a struvite solubility model was developed in which the equilibrium constants were treated as empirically distributed variables within a Monte Carlo simulation. This clarified the effect of uncertainty on precipitation potential over a range of pH (6 to 8.5), temperature (0 to 60°C), and ionic strength (0 to 1 M). Using field conditions measured at a struvite-afflicted treatment plant as model input parameters, the resulting uncertainty in the struvite supersaturation ratio was found to be highly consequential: the 90 percent confidence interval spanned well over an order of magnitude. Moreover, a sensitivity analysis performed on the model identified the third orthophosphate equilibrium constant and the struvite solubility product as the most significant sources of uncertainty.

This chapter has been published in a peer-reviewed journal, as cited by [Barnes & Bowers \(2017\)](#).

2.2 Introduction

Precipitation and subsequent accumulation of struvite ($MgNH_4PO_4 \cdot 6H_2O$) within sludge digestion and postdigestion processes has been a costly and enigmatic problem for wastewater facilities. Struvite crystals commonly form on the surface of pipes, mixers, and submerged mechanical equipment, limiting system efficacy and necessitating frequent maintenance. Fouling is often so extensive

that processes are rendered inoperable and entire pipe systems have to be replaced (Ohlinger et al., 1998; Mamais et al., 1994; Horenstein et al., 1990). Benisch et al. estimated that maintenance and capacity reduction related to struvite deposits could cost a midsize (95 MLD/25 MGD) plant more than \$100,000 per year (Benisch et al., 2000).

Though conditions of struvite supersaturation within a wastewater stream often promote fouling, they can also be ideal for the extraction of struvite for phosphorus recovery. Extracted struvite has proven to be of commercial use, as the phosphate and ammonia-rich crystals have been shown to be an effective slow-release fertilizer (Durrant et al., 1999).

Accurate prediction of the precipitation of struvite is tantamount to efficient and cost-effective design and operation of wastewater plants. More specifically, it is necessary to have an accurate model of struvite solubility that can be adapted to the highly variable conditions within a wastewater stream (Ohlinger et al., 2000). Similar considerations must be made when intentionally precipitating struvite for environmental or agricultural purposes.

2.2.1 Uncertainty

The efficacy of a deterministic model for struvite solubility is diminished by three unique sources of uncertainty — a problem that has not been adequately evaluated. These sources of uncertainty — wastewater composition, measurement errors, and equilibrium parameters — all affect struvite prediction in different ways.

2.2.1.1 Uncertainty in Concentrations

In struvite precipitation modeling, representative concentrations — usually a grab sample or an average of several grab samples — are commonly selected for each wastewater constituent (Ohlinger et al., 1998; Doyle & Parsons, 2002). Then, predictions are made using single, deterministic values under the pretense that average inputs will give an average output. This method, though simple and straightforward, does not evaluate the spatial and temporal variability of the constituents. Variability may be more prevalent in some constituents than others, and its effect on the conditional solubility product at different pHs, temperatures, and ionic strengths may be unevaluated.

While existing struvite equilibrium models are used for solutions of known/fixed concentrations, this idealized scenario is uncommon in wastewater. Instead, concentrations are in constant flux, rendering any deterministic predictions made from single or averaged values insufficient and obsolete the moment they are made.

The range of variability of constituent concentrations and wastewater properties are plant- and process-specific, so these must be evaluated on a case-by-case basis. As such, site-specific data must be collected to adequately characterize the spatial and temporal uncertainties.

2.2.1.2 Uncertainty Due to Errors in Measurement

All things measured physically, i.e. evaluation of concentrations and equilibrium constants, are affected by measurement error. However, for struvite, measurement errors accrued in the modern laboratory are rendered inconsequential compared to the uncertainty introduced by reported literature values. For example, the errors expected from different methods of measuring total phosphorus concentrations were all less than 0.05 mg/L (Rice et al., 2012, pg. 440). This is inconsequential compared to concentrations in wastewater streams on the order of 100 mg/L (Doyle & Parsons, 2002; Ali & Schneider, 2008). Measurement errors for orthophosphate, ammonia, total nitrogen, total magnesium, pH, and temperature were similarly insignificant, especially when compared to the uncertainty of equilibrium parameters for struvite. Therefore, the uncertainty due to measurement error was considered negligible.

2.2.1.3 Uncertainty in Equilibrium Parameters

Several models for struvite precipitation have been developed using chemical equilibria and solubility, including, for example, those outlined by Ohlinger et al. (1998) and Doyle & Parsons (2002). Equilibria software such as MINEQL+ and MINTEQA2 are regularly employed in chemical modeling. Unfortunately, this software assumes that equilibrium constants for the speciation and solubility of constituents are single, universally accepted values. This assumption is further promoted by reference materials that report only a single selected, or "critical," stability constant for each reaction: Smith & Martell (1996), for example. In reality, each of these constants (K_{sp} , K_{a1P} , K_{a2P} ,

K_{a_3P} , K_{a_1N} , K_{1Mg} , K_{MgP} , K_{MgHP} , and K_{MgH_2P}) is associated with a variety of published values—many with substantial differences—so they are not explicitly known. This lack of agreement in the values of published constants adds a level of uncertainty to the models that has not been investigated or quantified for struvite. For example, [Snoeyink & Jenkins \(1980\)](#), [Stumm & Morgan \(1994\)](#), [Mamais et al. \(1994\)](#), and [Loewenthal. et al. \(1994\)](#) reported a struvite solubility product, pK_{sp} , of 12.6; [Buchanan et al. \(1994\)](#) reported 12.36; and [Ohlinger et al. \(1998\)](#) and [Ali & Schneider \(2008\)](#) found a value of 13.26. In addition, [Borgerding \(1972\)](#) found a pK_{sp} of 9.41 for struvite solids resuspended in an ammonium acetate solution.

With almost four orders of magnitude difference, this uncertainty threatens the validity of struvite precipitation calculations. Furthermore, the significance of each constant depends on the pH and constituent concentrations of the waste stream (all variable over time) as well as the values of other constants. It is important to understand under which circumstances this uncertainty will be problematic and invalidate solubility predictions.

The purpose of this study was to develop a struvite solubility model in which the equilibrium constants could be treated with uncertainty (Monte Carlo variables) in order to understand the effects of uncertainty on struvite precipitation estimation. In addition, a sensitivity analysis was performed to identify which uncertainties have the most effect on equilibrium solubility predictions.

2.3 Chemistry of Struvite Precipitation

Struvite precipitation is dependent on the available concentrations of magnesium, ammonium, and phosphate, and forms as follows:



When concentrations of dissolved Mg^{2+} , NH_4^+ , and PO_4^{3-} exceed the struvite solubility limit, precipitation may occur. The equilibrium precipitation of struvite has been considered by a variety of researchers and can be described as follows ([Stumm & Morgan, 1994](#); [Ohlinger et al., 1998](#); [Doyle & Parsons, 2002](#); [Snoeyink & Jenkins, 1980](#); [Ali & Schneider, 2008](#)):

$$K_{sp} = [Mg^{2+}][NH_4^+][PO_4^{3-}] = [Mg_f][N_f][P_f](\alpha_{Mg^{2+}})(\alpha_{NH_4^+})(\alpha_{PO_4^{3-}}) \quad (2.2)$$

$$K_{sp_{cond}} = \frac{K_{sp}}{\alpha_{Mg^{2+}} \cdot \alpha_{NH_4^+} \cdot \alpha_{PO_4^{3-}}} \quad (2.3)$$

where K_{sp} is the solubility product of struvite at equilibrium, $K_{sp_{cond}}$ is the pH-conditional solubility product, Mg_f , N_f , and P_f are the free (water-based) magnesium, ammonia, and orthophosphate concentrations, and α_i denotes the fraction for each component described generically by:

$$\alpha_i = \frac{\text{free ion concentration}}{\text{concentration of water-based complexes}} \quad (2.4)$$

For struvite, the free ion concentrations consist of NH_4^+ , Mg^{2+} , and PO_4^{3-} . The concentration of all water based complexes, given by Mg_f , N_f , and P_f , represent the free magnesium, ammonia and orthophosphate species, respectively.

For ammonia/ammonium, the free and total species are identical, given by:

$$N_f = N_t = NH_3 + NH_4^+ \quad (2.5)$$

Free (water-based) magnesium and orthophosphate species are given by:

$$Mg_f = Mg^{2+} + MgOH^+ + Mg(OH)_2 + Mg(OH)_3^- \quad (2.6)$$

$$P_f = H_3PO_4 + H_2PO_4^- + HPO_4^{2-} + PO_4^{3-} \quad (2.7)$$

The total dissolved species concentrations include magnesium phosphate species, and are represented by:

$$Mg_T = Mg_f + MgPO_4^- + MgHPO_4 + MgH_2PO_4^+; \quad (2.8)$$

and,

$$P_T = P_f + MgPO_4^- + MgHPO_4 + MgH_2PO_4^+; \quad (2.9)$$

In conjunction with the mass balance equations above, precipitation is controlled by the following equilibria:

$$K_{a_1P} = \frac{[H^+][H_2PO_4^-]}{[H_3PO_4]} \quad (2.10)$$

$$K_{a_2P} = \frac{[H^+][HPO_4^{2-}]}{[H_2PO_4^-]} \quad (2.11)$$

$$K_{a_3P} = \frac{[H^+][PO_4^{3-}]}{[HPO_4^{2-}]} \quad (2.12)$$

$$K_{a_1N} = \frac{[H^+][NH_3]}{[NH_4^+]} \quad (2.13)$$

$$K_{1Mg} = \frac{[Mg^{2+}][OH^-]}{[MgOH^+]} \quad (2.14)$$

$$K_{MgP} = \frac{[Mg^{2+}][PO_4^{3-}]}{[MgPO_4^-]} \quad (2.15)$$

$$K_{MgHP} = \frac{[Mg^{2+}][HPO_4^{2-}]}{[MgHPO_4]} \quad (2.16)$$

$$K_{MgH_2P} = \frac{[Mg^{2+}][H_2PO_4^-]}{[MgH_2PO_4^+]} \quad (2.17)$$

The ionization fraction of these components and, subsequently, the availability of magnesium, ammonium, and phosphate to form struvite, is highly pH-dependent. More specifically, over the

operating pH range of typical wastewater treatment plants (6.0 - 8.5), struvite solubility decreases significantly as pH increases.

Sometimes when struvite precipitates, it can do so rapidly and in localized areas of a treatment system. [Borgerding \(1972\)](#) observed that struvite formed preferentially on surfaces within low-pressure zones such as pipe bends, venturis, and areas where pump suction creates localized pH increases from CO_2 volatilization. Similarly, in this work, localized struvite precipitation has been observed on the surfaces of mixing blades and caustic discharge tubes, seemingly due to localized elevation of pH. This phenomenon, while important to the prevention of struvite precipitation, is not considered here.

In highly saline waters, chlorine/magnesium complexes such as $MgCl^+$ may interfere with precipitation calculations. However, in examining literature values for $Mg - Cl$ equilibria in dilute systems where $[Cl^-] \leq 0.1M$ and $[Mg^{2+}] \leq 2 \cdot 10^{-3}M$, less than 1 percent of total magnesium would be as $MgCl^+$ ([Smith & Martell, 1996](#); [IUPAC, 2011](#)). Sulfides and other lesser ions will be disregarded for similar reasons, but should any of their concentrations be uncharacteristically high in a waste stream, they would need to be considered.

2.3.1 Ionization Fractions

Any model requires the formulation of equations for the individual ionization fractions. For use in calculating the struvite precipitation potential, this is only necessary for the three ions of interest: ammonium, orthophosphate, and magnesium. These are described as a function of pH as follows:

$$\alpha_{NH_4^+} = \frac{[H^+]}{[H^+] + K_{a1N}} \quad (2.18)$$

$$\alpha_{PO_4^{3-}} = \frac{PO_4^{-3}}{P_f} = \frac{K_{a1P} \cdot K_{a2P} \cdot K_{a3P}}{[H^+]^3 + (K_{a1P} \cdot [H^+]^2) + (K_{a1P} \cdot K_{a2P} \cdot [H^+]) + (K_{a1P} \cdot K_{a2P} \cdot K_{a3P})} \quad (2.19)$$

$$\alpha_{Mg^{2+}} = \frac{Mg^{2+}}{Mg_f} = \frac{1}{1 + K_{1Mg} \cdot [OH^-]} \quad (2.20)$$

2.3.2 Precipitation Potential

Once the available fractions of $[Mg^{2+}]$, $[NH_4^+]$, $[PO_4^{3-}]$ are evaluated at fixed pH, Equations 2.10 through 2.20, they can be combined with the struvite solubility product, Equation 2.2, to calculate the pH-conditional struvite solubility product, K_{spcond} , Equation 2.3.

The formation and precipitation of struvite is dependent on the difference between the chemical potential of the salt in the supersaturated solution, μ_s , and the chemical potential of the salt at equilibrium, μ_∞ (Bouropoulos & Koutsoukos, 2000). This difference, $\Delta\mu$, can be described by:

$$\begin{aligned}\Delta\mu &= \mu_\infty - \mu_s \\ &= [\mu_\infty^0 + kT \ln(\alpha_{Mg^{2+}} \cdot \alpha_{NH_4^+} \cdot \alpha_{PO_4^{3-}})_\infty^{1/3}] \\ &\quad - [\mu_s^0 + kT \ln(\alpha_{Mg^{2+}} \cdot \alpha_{NH_4^+} \cdot \alpha_{PO_4^{3-}})_s^{1/3}]\end{aligned}\quad (2.21)$$

where k is the Boltzmann constant and T is absolute temperature. Assuming that the chemical potentials of the two standard states are equal, or $\mu_\infty^0 = \mu_s^0$, then

$$\Delta\mu = kT \ln \left[\frac{(\alpha_{Mg^{2+}} \cdot \alpha_{NH_4^+} \cdot \alpha_{PO_4^{3-}})_\infty^{1/3}}{(\alpha_{Mg^{2+}} \cdot \alpha_{NH_4^+} \cdot \alpha_{PO_4^{3-}})_s^{1/3}} \right] = -\frac{kT}{3} \ln(\Omega) \quad (2.22)$$

where Ω is the supersaturation ratio as developed by Bouropoulos and Koutsoukos (2000) and given by

$$\Omega = \frac{Mg_f \cdot N_f \cdot P_f}{K_{spcond}} \quad (2.23)$$

In theory,

$$\Omega > 1 \Rightarrow \text{supersaturation (precipitation occurs)} \quad (2.24)$$

$$\Omega < 1 \Rightarrow \text{undersaturation (precipitation does not occur)}$$

Use of the Ω factor makes it possible to determine whether struvite will or will not precipitate.

Most published struvite research uses similar constitutive equations for equilibrium calculations (Stumm & Morgan, 1994; Ohlinger et al., 1998; Doyle & Parsons, 2002; Snoeyink & Jenkins, 1980; Ali & Schneider, 2008). The kinetic models were less consistent between sources, but kinetics are not modeled in this paper. While free energy equilibriums could be derived and used in a precipitation model, use of the selected model is common with both practitioners and researchers. This ubiquity is especially relevant as the uncertainty calculations can be indirectly applied to many similar models already in use.

2.4 Monte Carlo Model

2.4.1 Equilibrium Constant Distributions

In the Monte Carlo framework, the equilibrium constants in Equations 2.18, 2.19, and 2.20 were treated as random rather than fixed variables. The probability distribution of each variable was established from numerous constants reported in peer-reviewed sources; their variability was used to dictate uncertainty.

Considering all relevant equilibrium constants, every literature value was reported along with the solution ionic strength and temperature. These values and their respective distributions are presented for $I = 0$ and $T = 25^\circ\text{C}$ in Table 2.1. It is important to note that much of the literature data was taken from the International Union of Pure and Applied Chemistry database (IUPAC, 2011), as well as several published compendiums such as Goldberg et al. (2002) and Hanhoun et al. (2011).

Some constants, such as pK_{a_1P} and pK_{a_1N} , have relatively little variation within the published values. This led to a narrow distribution and minimal uncertainty. On the other hand, the uncertainty of pK_{sp} and pK_{1Mg} led to distributions with significant standard deviations.

2.4.2 Effects of Temperature and Ionic Strength

The equilibrium constants relevant to struvite solubility calculations are highly dependent on the temperature (T) of the solution (Aage et al., 1997; Hanhoun et al., 2011; Bhuiyan et al., 2007). For

Table 2.1: Equilibrium constants from selected peer-reviewed sources and their respective characteristic values at 25 °C and $I = 0$. Values in the “Count” column are the number of constants included in the analysis that were reported for 25 °C and $I = 0$ and the number in the parentheses is the number of total values used in the analysis at all temperatures and ionic strengths. Data taken from IUPAC (2011); Goldberg et al. (2002); Hanhoun et al. (2011); Ohlinger et al. (1998); Linder & Little (1985). IUPAC (2011) and Goldberg et al. (2002) consists of a database using many peer-reviewed sources.

Equilibria	Mean pK(SD)	Lit. Range	Count
$H^+ + H_2PO_4^- \Leftrightarrow H_3PO_4$	2.139 (0.011)	2.120-2.151	16(72)
$H^+ + HPO_4^{2-} \Leftrightarrow H_2PO_4^-$	7.196 (0.036)	7.050-7.224	20(133)
$H^+ + PO_4^{3-} \Leftrightarrow HPO_4^{2-}$	12.254 (0.177)	11.848-12.390	19(53)
$NH_3(aq) + H^+ \Leftrightarrow NH_4^+$	9.240 (0.016)	9.215-9.290	23(93)
$Mg^{2+} + PO_4^{3-} \Leftrightarrow MgPO_4^-$	5.390 (0.870)	4.800-6.590	6(12)
$Mg^{2+} + HPO_4^{2-} \Leftrightarrow MgHPO_4$	2.784 (0.260)	2.428-3.086	6(18)
$Mg^{2+} + H_2PO_4^- \Leftrightarrow MgH_2PO_4^+$	1.000 (0.513)	0.450-1.510	5(12)
$Mg^{2+} + OH^- \Leftrightarrow MgOH^+$	2.535 (0.132)	2.210-2.600	8(19)
$Mg^{2+} + NH_4 + PO_4^{3-} + 6H_2O \Leftrightarrow MgNH_4PO_4 \cdot 6H_2O(s)$	12.955 (0.309)	12.360-13.360	15(31)

most constants described by Equations 2.10-2.17, the number of published constants are insufficient to develop individual distributions at temperatures other than 25 °C. Modeling the influence of ionic strength (I) on the equilibrium constants is similarly impaired, as the literature focuses heavily on solutions of zero ionic strength. Table 2.2 highlights the extent of this problem using pK_{a_2P} as a representative example.

Table 2.2: Number of published values of pK_{a_2P} within given ranges of temperature (°C) and ionic strength ($M^{0.5}$).

T, °C	Count of reported pKs				
50 - 60	8	0	0	0	0
40 - 50	10	0	0	0	0
30 - 40	12	6	1	1	0
20 - 30	26	21	5	4	14
10 - 20	8	1	0	0	1
0 - 10	5	0	0	0	0
\sqrt{I}	0 - 0.2	0.2 - 0.4	0.4 - 0.6	0.6 - 0.8	0.8 - 1.0

Fortunately, for phosphate, magnesium, and ammonium, as well as the struvite solubility, there are more than enough equilibrium constants reported at various (T, I) pairs to construct a three-dimensional regression across temperature and ionic strength. Assuming that the regression

surfaces adequately describe the mean of the underlying distribution at any (T, I) pair over the temperature range of 0-60°C, each literature value can be translated into its deviation from the mean. To simplify, by combining the information from all of the literature with respect to temperature and ionic strength, the variability of all the reported constants can be analyzed together as the residuals from the regression surface.

As described extensively by [Blandamer et al. \(1982\)](#), there are many methods by which the effects of temperature and ionic strength on equilibrium constants can be modeled. While some of these equations may be more widely accepted than others, a simple quadratic regression fit the literature data for struvite and associated equilibria. Figure 2.1 shows a comparison between literature values and the associated three-dimensional regression surface for pK_{a_2P} as a representative example (Equation 2.11). The polynomial regression was fitted with respect to the inverse of temperature and the square root of ionic strength, as is standard practice ([Blandamer et al., 1982](#)).

The quadratic fit described by Equation 2.25 was used for all equilibrium values except in the case of pK_{MgP} and pK_{MgH_2P} . For these two exceptions, the variety and number of (T, I) literature pairs reported were insufficient to support a quadratic fit. Therefore, a linear fit, Equation 2.26, was used for these two cases. The coefficients associated with these fits are shown in Table 2.3.

$$pK_{fit} = a + b(1/T) + c\sqrt{I} + d(1/T)\sqrt{I} + e(1/T)^2 + fI \quad (2.25)$$

$$pK_{fit} = a + b(1/T) + c\sqrt{I} \quad (2.26)$$

These regression surfaces allow the uncertainty provided by all of the literature values to be incorporated into the Monte Carlo model at any temperature and ionic strength from T = 0 to 60°C and I = 0 to 1.0 M considering interference due to chlorides. A probability distribution was fit to the regression residuals for each constant. For each realization of the Monte Carlo, a residual was taken from the distribution as a random variable and added to the mean pK at any (T, I) pair as calculated by the regression equation. This distributional input was used for all constants in Equations 2.2-2.20

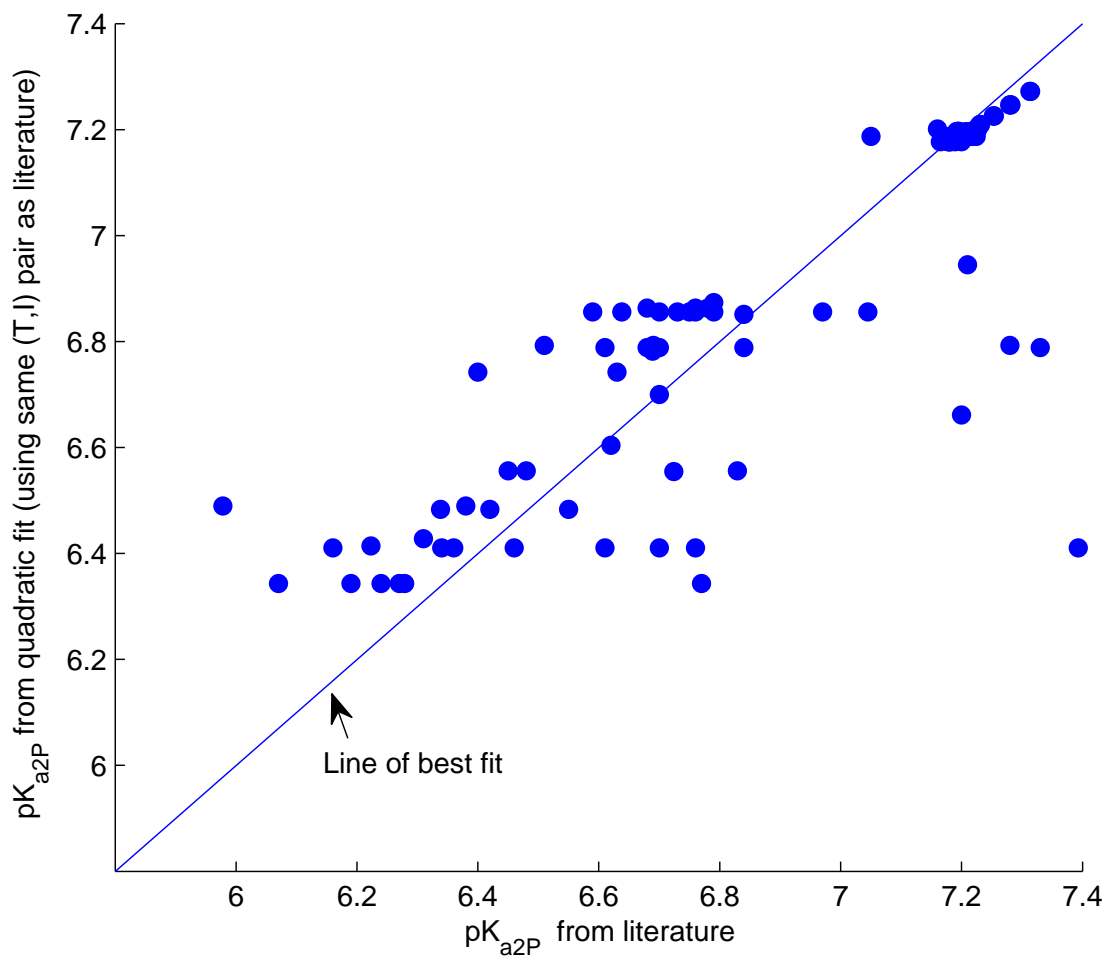


Figure 2.1: Comparison between published pK_{a_2P} values and the values generated by the quadratic fit at the same (T, I) pairs. The goodness-of-fit of the quadratic can be represented by the deviation of points from the line of perfect fit. Note: the cluster around a pK_{a_2P} of about 7.2 is a result of the high frequency in which the (T, I) pair of 25 °C and 0 M was reported in the literature.

Table 2.3: Coefficients for the quadratic (Q) or linear (L) fits of each equilibrium constant and their associated R^2 .

Constant	Fit	a	b	c	d	e	f	R^2
pK_{a1P}	Q	11.36	-5113	7.25	-2327.09	703577	0.24	0.52
pK_{a2P}	Q	11.91	-2954	-0.77	-120.75	460605	0.40	0.77
pK_{a3P}	Q	184.06	-104884	-14.16	3753.46	15991713	0.54	0.70
pK_{a1N}	Q	-1.36	3610	-0.19	65.93	-133053	0.12	0.88
pK_{1Mg}	Q	-20.97	15492	-1.57	0	-2527493	1.51	0.70
pK_{MgP}	L	6.57	-229	-6.12	-	-	-	0.63
pK_{MgHP}	Q	21.21	-10642	-4.82	466.43	1543299	1.40	0.88
pK_{MgH2P}	L	-0.81	595	-0.55	-	-	-	0.32
pK_{sp}	Q	186.81	-106249	-4.05	0	16228818	3.69	0.48

to produce a probabilistic output for Ω vs. pH at any (T, I) pair using Equation 2.23. As is apparent in the pK_{a2P} histogram shown in Figure 2.2, the residuals are not normal, nor do they fit any other common distribution. This is also true for all nine equilibrium constants involved, which often display bimodal or otherwise incongruous behavior.

2.4.3 Input Distributions for Equilibrium Constants

For modeling, two separate input distributions, uniform and empirical, were considered to properly represent equilibrium constant uncertainty. These two distributions were used for comparison, and the choice to use one over the other cannot be made on purely statistical criteria. Rather, the choice relies heavily on the purpose of the model, how conservative the predictions must be, and assumptions on the development of verisimilitude.

2.4.3.1 Uniform Distribution

In previous struvite precipitation models, K or pK values were drawn from different, individual sources (see [Ohlinger et al. \(1998\)](#); [Ali & Schneider \(2008\)](#), and [Hanhoun et al. \(2011\)](#)). Under the conservative assumption that each peer-reviewed source is equally valid, a uniform distribution can be used to encapsulate the full envelope of uncertainty ([Johnson & Balakrishnan, 1995](#)). The distribution ranges from the minimum of the residuals to the maximum of residuals, or in the case

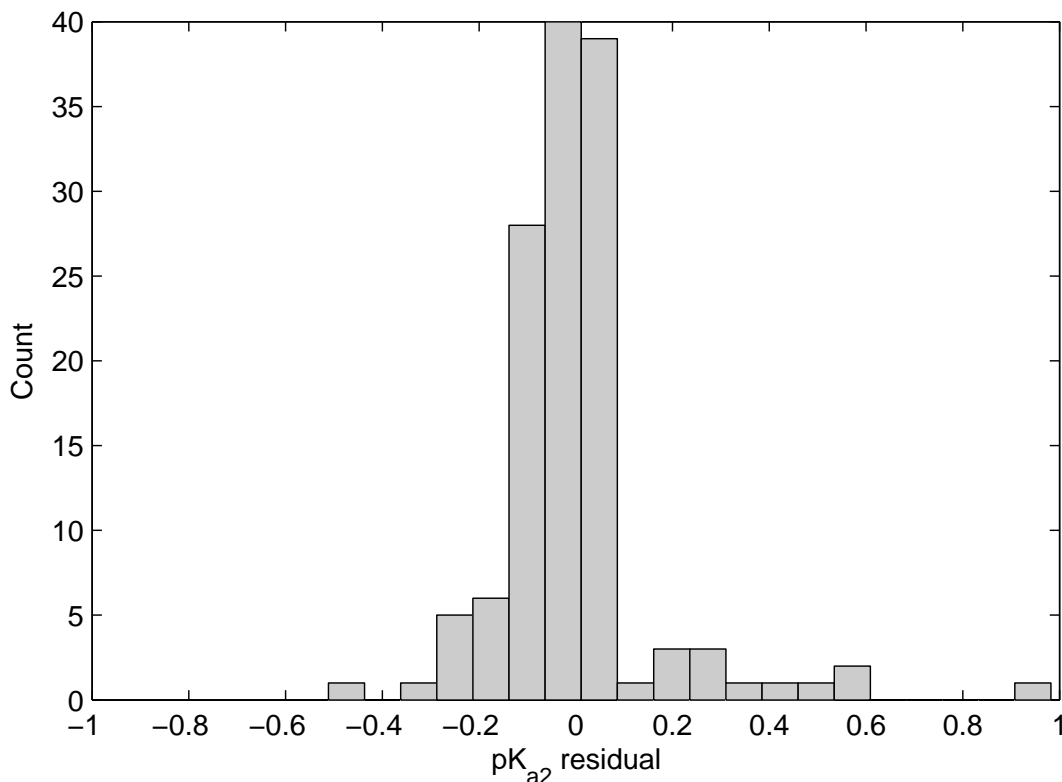


Figure 2.2: Difference between published pK_{a2P} values and the associated linear regression surface (residuals). The ‘count’ value represents the number of calculated residuals that fall within each bin.

of pK_{a2P} shown in Figure 2.3, -0.512 to +0.983. Anything within this range is assumed to have equal probability of being the actual underlying equilibrium constant. As this is on a log scale, this distribution covers nearly 1.5 orders of magnitude. Then, the use of uniform distributions as the input makes it possible to assess a "worst-case scenario" for Ω uncertainty.

2.4.3.2 Empirical Distribution

A uniform distribution assumes the location of a literature value relative to all other published values for that constant has no weight on its validity. That is, under the conservative assumptions of a uniform distribution, a value that is three standard deviations from the mean of all literature values is considered equally valid as one that is exactly at the mean. On the one hand, this assumption makes sense as multiple labs could have discerned their values using the same, less accurate method,

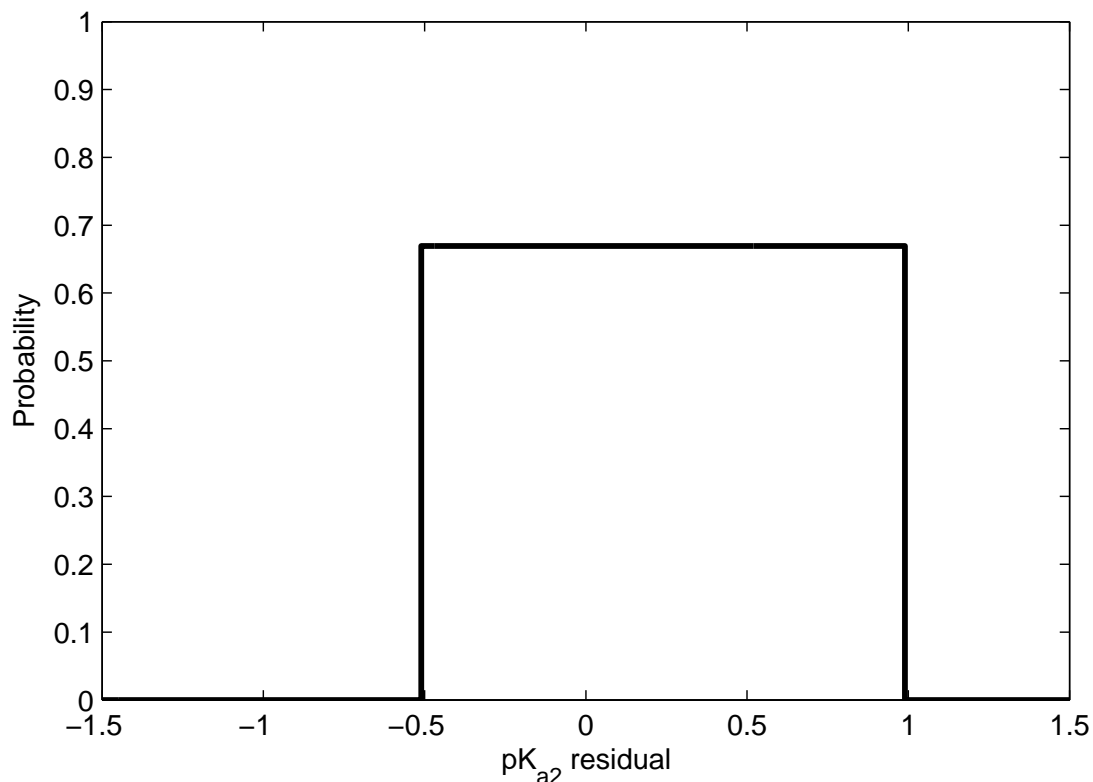


Figure 2.3: Uniform distribution of regression residuals for pK_{a2P} of phosphate. Probability is calculated such that the area under the curve is equal to 1.0.

and this agreement does not make the results more correct. On the other hand, peer review is predicated on the idea that consensus is an indicator of correctness. As such, empirical distributions were also used for the distribution of equilibrium constants.

In an empirical distribution, the actual literature pKs are the only values used in the simulation. More simply put, each time the Monte Carlo simulation runs one of 10,000 iterations, a specific literature value is selected at random (equal weight to each published value) and used for the entirety of that realization (Thomopoulos, 2012). After all iterations, the distribution of pKs looks nearly identical to a scaled histogram of the literature values. For example, Figure 2.2 becomes Figure 2.4 once it is scaled to a probability density function.

While the empirical distribution accurately reflects the uncertainty inherent in the literature, it does not represent experimental error caused by the determination of the individual equilibrium

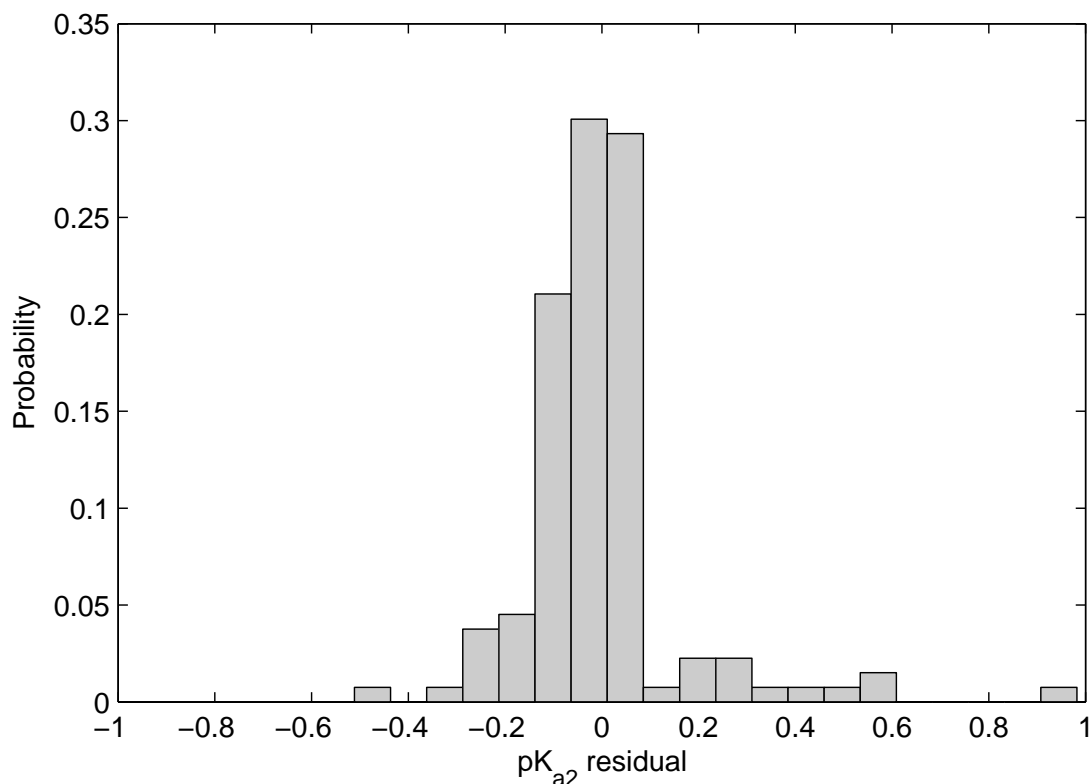


Figure 2.4: Empirical distribution of regression residuals for $pK_{a2}P$ of phosphate.

constants. With perfect information, the underlying equilibrium constants would be single, unchanging values. In addition, uncertainty caused by dissimilar literature values is not the only source of uncertainty. Temporal variability of pH, T, I, and the three input constituents as well as the rate of reaction and choice of background matrix could all add to the uncertainty; however, this effort is limited to evaluating the magnitude of uncertainty within the literature. The use of an empirical, data-driven distribution rather than a selected theoretical model in a stochastic simulation is common practice in risk assessment, most notably by the United States Environmental Protection Agency (Bennett et al., 2001).

2.4.4 Model Summary

Using Equations 2.2 to 2.23 and the equilibrium constant regression data, a MATLAB model was created using inputs of pH, temperature, and ionic strength as well as total magnesium,

phosphorus, and nitrogen concentrations (Mg_T , P_T , N_T). This returns a probabilistic envelope for the precipitation potential, Ω . The Monte Carlo simulations proceed as described in Figure 2.5.

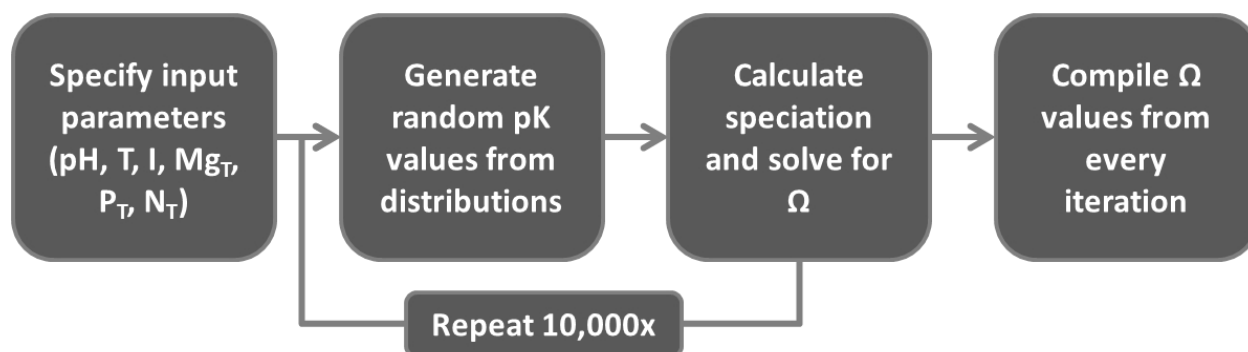


Figure 2.5: Simplified flowchart of the Monte Carlo simulation.

The Ω value was calculated from $K_{sp_{cond}}$ (Equation 2.3). The α values (Equation 2.3) were calculated by evaluating the free magnesium and orthophosphate species given by Equations 2.6 and 2.7, and the ionization fractions for each component ion as outlined by Equations 2.18, 2.19, and 2.20. As these equations require circular referencing, an optimization routine was written to find values for Mg_f , N_f , and P_f that satisfied the mass balances given by Equations 2.8, 2.5, and 2.9.

2.4.5 Comparison to the Literature

In order to effectively mitigate struvite buildup or design a phosphorus recovery process, a wastewater utility needs to have an accurate model for predicting and analyzing constituent concentrations and struvite precipitation within the waste stream. Unfortunately, the underlying uncertainty of published equilibrium constants threatens the validity of conclusions drawn from deterministic models.

To demonstrate the validity of the model, the conditional solubility product, as $\log(K_{sp_{cond}})$, was simulated from pH 6.0 to 10.0 using both uniform and empirical distributions. The resulting plot of the conditional solubility product versus pH can be seen in Figure 2.6 along with experimental values of $K_{sp_{cond}}$ published by [Musvoto et al. \(2000\)](#) and [Ohlinger et al. \(2000\)](#). The model and

the literature data show excellent agreement (all of the data fit within the uniform envelope of uncertainty, and most within the empirical values) and validates the need for probability analysis.

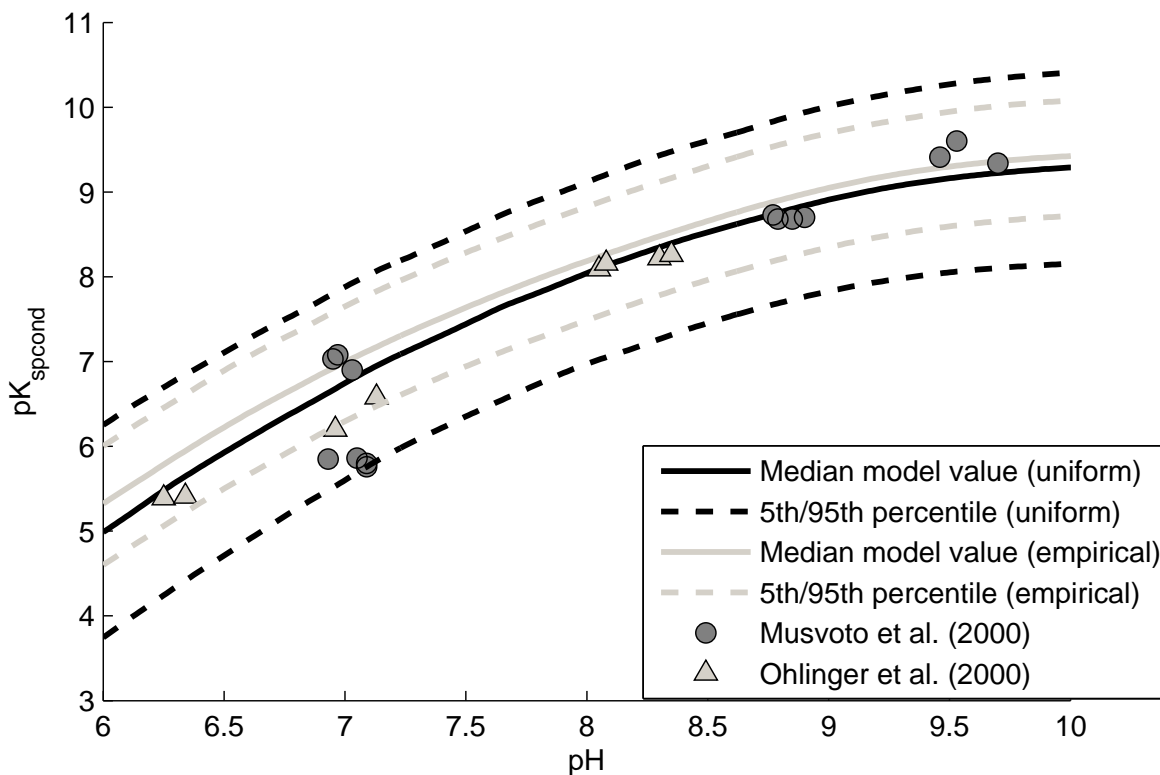


Figure 2.6: Conditional solubility product predicted by the Monte Carlo model using both uniform and empirical distributions for the equilibrium constants. The discrete data points were taken from three prominent struvite studies that evaluated K_{spcond} in the laboratory, and were included to lend credence to the model (Musvoto et al., 2000; Ohlinger et al., 2000). Note the lognormality of the vertical axis.

2.5 Methods

2.5.1 Field Experimentation

Depending on the uncertainty of limiting constituents at the selected pH, temperature, and pressure, the final uncertainty in Ω varies widely. To best highlight this uncertainty, a field test was performed in the centrate aeration basins at a metropolitan wastewater treatment facility that has experienced problems with struvite precipitation.

Metal coupons (steel, aluminum, and epoxy painted) were placed around a conventional aeration basin (plug-flow configuration) at key locations. Additionally, grab samples were taken several times per day at each of these locations. These basins—totaling 415 meters (1,360 ft) long with an average residence time of approximately 2 days—treat centrate from anaerobically digested wastewater sludge containing both primary and secondary solids. This process is performed to nitrify ammonia to carry over into a conventional aerobic wastewater treatment plant. Concentrations of the main constituents of struvite (typically: $NH_4^+ > PO_4^{3-} > Mg^{2+}$) were seen to vary greatly over time due to inconsistency in the centrate source.

Struvite formed in the basins due to localized increases in pH from stripping of CO_2 under vigorous aeration and the addition of caustic ($NaOH$) to maintain a suitable pH for nitrification to occur (pH 7-8 preferred). Due to the plug-flow nature of the basins, the addition of caustic resulted in a localized region of higher pH, which caused struvite to precipitate onto mixers and other equipment suspended in the basins. The influent to the basins consisted of the anaerobic sludge centrate, flow from the main aeration basins (bacterial seed), and recycle from the tail end of the centrate basins (about 1 MGD each).

The solid precipitates that accumulated onto the metal coupons were dissolved in acid and the constituents were analyzed using an Inductively Coupled Argon Plasma Mass Spectrometer (ICAP-MS). In all cases, the magnesium-to-calcium ratio always exceeded 100:1, leaving the calcium species as an insignificant fraction. Chlorine was also measured and found to be similarly negligible. In addition, the Mg:P ratio indicated struvite as the major precipitate.

To verify these findings, X-ray powder diffraction (XRD) was performed on samples of foulant crystals taken from a submerged mixer near the front of the nitrification basin. The XRD measurements were performed using a Scintag XGEN-4000 X-ray diffractometer with a $CuK\alpha$ ($\lambda = 0.154$ nm) radiation source. The resulting diffraction patterns were then visually compared to literature data (International Union of Crystallography database) to determine the structure. The scans were run from 10-80 degrees in 2Θ with a 0.1 degree step size and 10 second dwell time, and the sample was found to be almost exclusively struvite.

For other systems outside this study that exhibit higher concentrations of calcium or chloride, further analysis may be required to determine the solid phases formed. Modifying the model described in this article to include any other impactful species would be straightforward, requiring only the collection of pertinent equilibrium constants and the inclusion of the species in the equilibrium equations.

2.5.2 Evaluation of Field Parameters

The constituent concentrations for the first sample point (early in the nitrification process) were averaged to find a prototypical set of constituent concentrations that will be used in forthcoming example simulations for simplicity. More specifically, for total magnesium, orthophosphate, and ammonia, these values were 0.0013 M, 0.0046 M, and 0.0283 M, respectively. Measurements of ammonia and phosphate were performed on site using a LaMotte 1200 Colorimeter, with a sensitivity of 0.05 ppm $NH_3 - N$ and 0.05 ppm $PO_4^{3-} - P$. Magnesium measurements were measured using an ICAP Q ICP-MS in accordance with [Rice et al. \(2012\)](#), which exhibit a sensitivity many orders of magnitude less than the concentrations being evaluated.

The temperature was measured to be approximately 25 °C with only minor variability. The average ionic strength was estimated using Equation 2.27 ([Sposito, 2008](#)) and electrical conductivity (EC) measurements, and was found to be approximately 0.1 M (conductivity was measured five times, with variability of less than 20 percent between samples).

$$\log I = 1.159 + 1.009 \log EC \quad (2.27)$$

valid for $I \leq 0.3$ M.

2.6 Results

2.6.1 Field Results

The effect of parameter uncertainty on the model's ability to predict precipitation potential is enormous, as is apparent in Figure 2.7. These simulated Ω plots are broken up into three regions:

A, B and C. Systems that fall under Section A have >95% confidence that precipitation would not occur; those in Section C have >95% confidence that it would occur; and, in between, there is 90% confidence that precipitation would occur in Section B. Ideally, if the ranges of published constants were much smaller (narrower Section B), these plots could be used to predict the pH at which precipitation should occur by simply finding where $\Omega > 1$. However, with parameter uncertainty included, there is only 90 percent confidence that struvite will precipitate somewhere in zone B, i.e., between pH 6.28 and 7.68 using the uniform distribution (Figure 2.7 - top) and pH 6.36 and 7.22 using the empirical distribution (Figure 2.7 - bottom). These pH ranges exist well within the typical range of operations, i.e., pH 6.0 to 8.0.

2.6.2 Precipitation Prediction: Field Case

During the two-week field trial, coupons were submerged in the waste stream at eight points as described previously. Samples were collected and analyzed (P, N, Mg, pH, temperature, and ionic strength) at each coupon station several times per day.

The occurrence of precipitation upon the coupons was determined first with simple visual confirmation. Struvite crystallization was easily recognizable as it was visible against the metal surface of the coupons, but the crystals were dissolved and evaluated with the ICAP Q ICP-MS to verify struvite by the presence of Mg/P.

The Monte Carlo model was run using lognormally distributed input concentrations (Mg, N, P, and pH) derived from the field sampling to predict struvite precipitation. It is important to note that these parameters were not considered as distinct single values by the final precipitation model, but were instead input as distributions so that their uncertainty could also be evaluated within the Monte Carlo framework. Table 2.4 contains a brief statistical overview of the samples taken from the basin at the first coupon (first sample point in the waste stream, just inside the influent pipe). It is important to note that concentrations and pH were generally higher near the start of the aeration train, as was struvite precipitation, so this table adequately showcases the breadth of variability that could be expected.

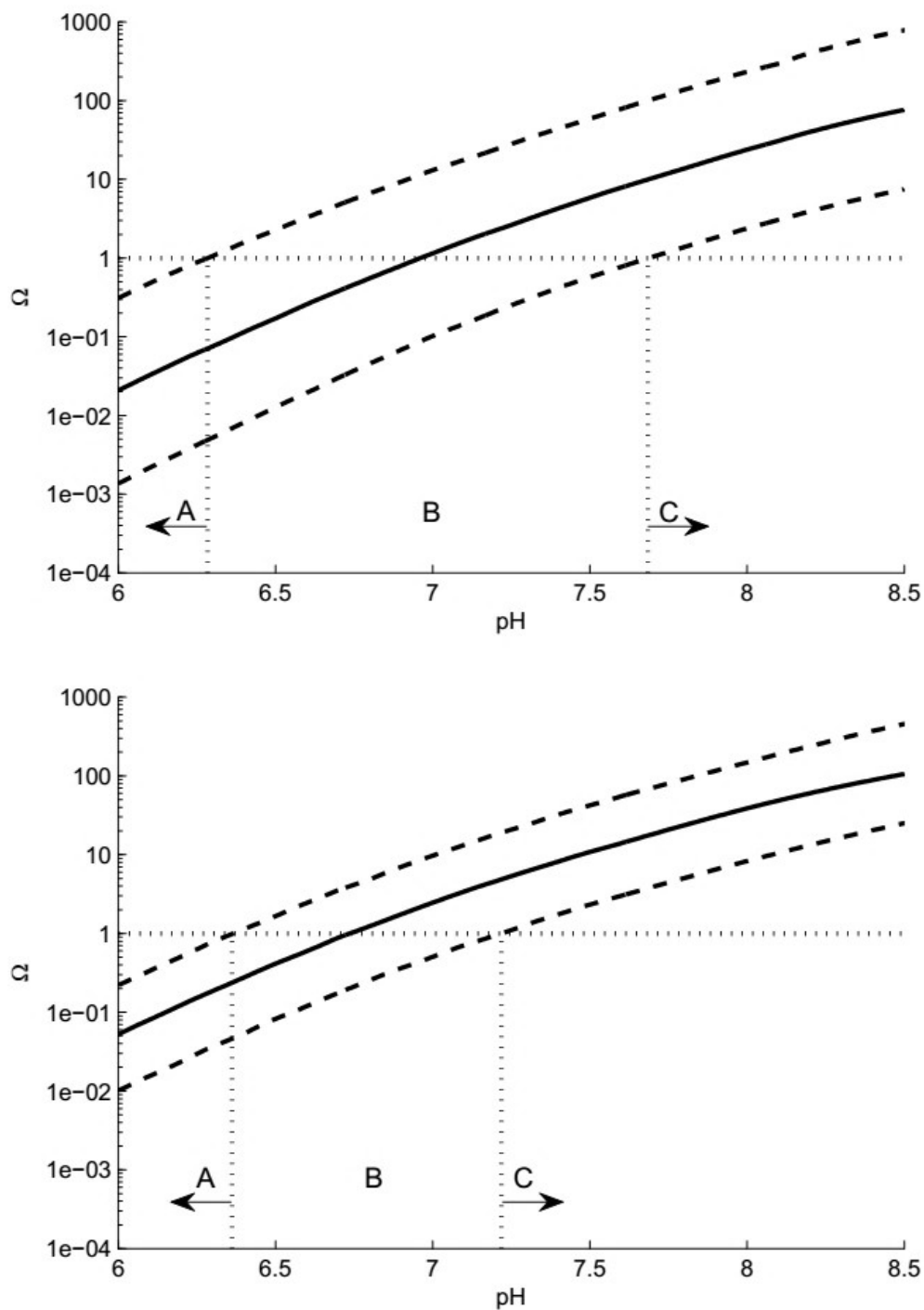


Figure 2.7: Omega values predicted by the Monte Carlo model using uniform (top) and empirical (bottom) distributions for the equilibrium constants. Mg_T , P_T , and N_T were set to 0.0013 M, 0.0046 M, and 0.0283 M, respectively; $T = 25^\circ\text{C}$, and $I = 0.1\text{M}$. The solid line represents the median value and the dashed lines are the 5th and 95th percentiles, leading to 90 percent confidence that precipitation will occur somewhere in Section B.

Table 2.4: Summary of 44 samples taken at the aeration basin influent (coupon set 1) over the two-week trial period. Note: seven more sets of data were collected at the other coupon locations.

	pH	Mg	P	N
		mg/L	mg/L	mg/L
Mean	7.57	26.3	140.0	588.1
Standard Deviation	0.12	9.6	46.5	460.5

The consideration of concentration variability differentiates this model from the models run in the previous sections when only literature uncertainty was being highlighted. The results of this simulation are depicted in Figure 2.8.

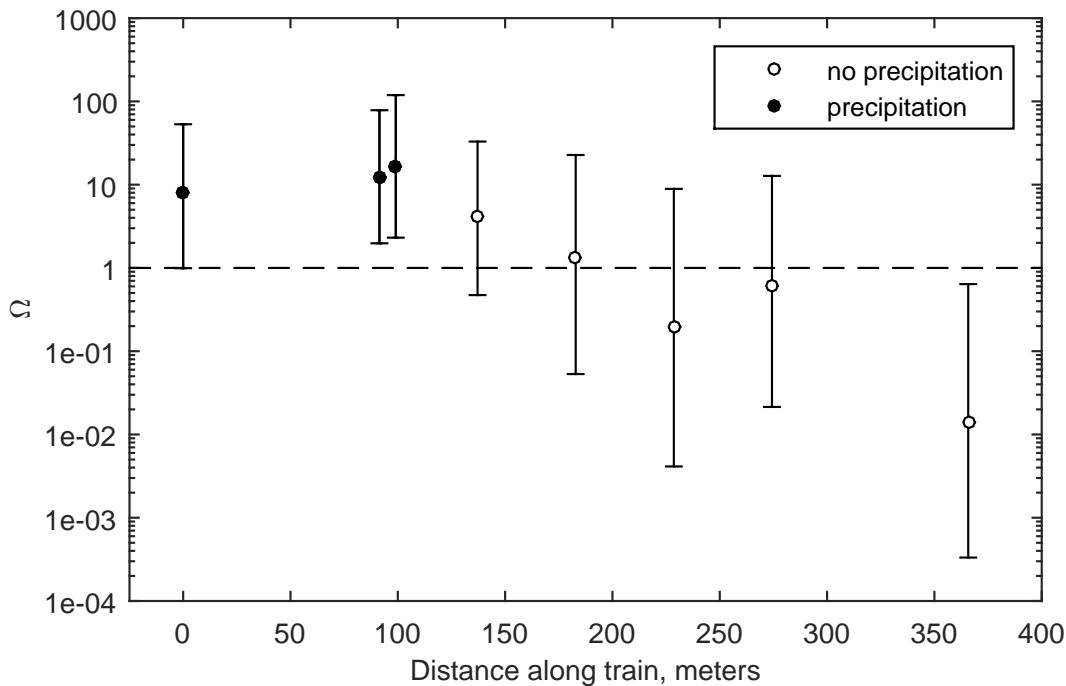


Figure 2.8: Omega values predicted at each point along the nitrification basin where a coupon was submerged, using an empirical distribution for the equilibrium constants. Mg_T , P_T , and N_T were input as lognormally distributed variables generated from the field sample concentrations; temperature and ionic strength were assumed constant at $T = 25^\circ\text{C}$ and $I = 0.1M$. The central markers represent the median simulated Ω and the “error bars” represent the 5th and 95th percentiles at each distance, leading to 90 percent confidence that precipitation will occur between the two bars.

As is apparent in Figure 2.8, the model accurately predicted where precipitation would occur. The envelopes of the first three reactor locations fall exclusively above $\Omega = 1$, giving at least 95 percent confidence that precipitation would occur, and it did. The simulation predicted no precipitation on the coupon at 366 meters, and was again correct. For envelopes that straddled the supersaturation line, predictions for the coupons at 130, 183, 229, and 274 meters were less certain. None of them exhibited struvite buildup at the end of the two-week trial period, a result that fits within the model predictions. It is possible that over the two weeks the solution alternated between supersaturation and undersaturation due to changes in wastewater composition. Precipitation may have occurred at some time, only to redissolve later due to below-average concentrations in the waste stream.

Altogether, the field case appears to support the validity of the Monte Carlo model and highlight the importance of considering uncertainty when predicting precipitation under variable conditions.

2.6.3 Sensitivity Analysis

A sensitivity analysis was performed on the Monte Carlo model. Using the field data and a fixed pH, the effects of the uncertainty for each equilibrium constant were evaluated by running the simulation nine times, removing the uncertainty from a different equilibrium constant each time. More specifically, the parameter in question was set to the value given by its three-dimensional quadratic fit. By holding one parameter constant while allowing the others to exhibit their uncertainty, the width of the resulting Ω was compared to the Ω at full uncertainty (with the uncertainty of all constants). The difference between these two Ω envelopes quantified the uncertainty for each equilibrium constant. The results of a sensitivity analysis at pH 6.0, 7.0, and 8.0 can be seen in Figure 2.9. Clearly, K_{a3P} and K_{sp} dominate the uncertainty in predicting struvite precipitation for pH 6.0 to 8.0.

2.7 Conclusions

The equilibrium parameters involved in struvite precipitation are not strictly known, and the variability in the literature values leads to substantial uncertainty in equilibrium predictions. The

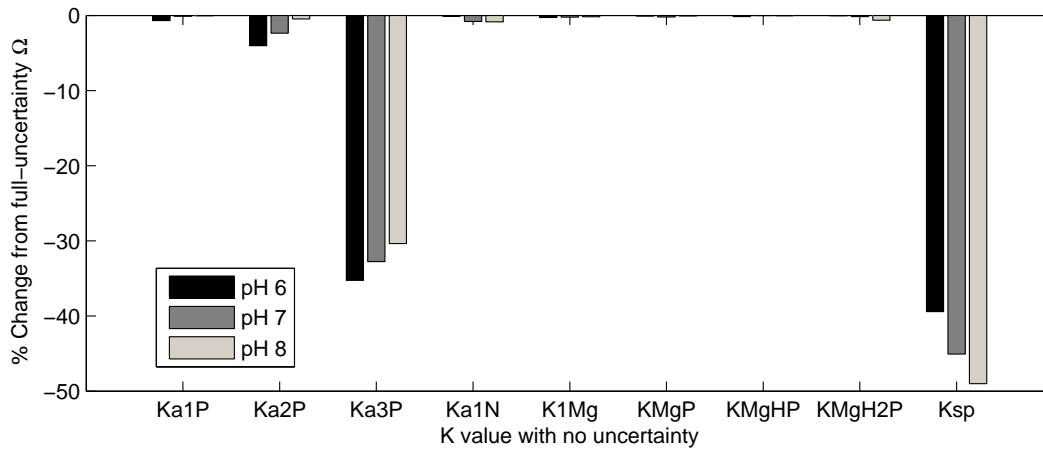


Figure 2.9: Uncertainty in final Ω (5%-95% envelope width) added by each equilibrium constant at pH 6, 7, and 8. For each bar, one constant was fixed at its regression surface value at $T = 25^\circ\text{C}$, and $I = 0.1\text{ M}$. Each value is compared to the Ω envelope at full uncertainty for that pH.

Monte Carlo simulations performed in this research show that deterministic models, despite their prevalence in contemporary studies, are insufficient for the accurate prediction of solubility. Due to this uncertainty of inputs, there is an inherent limit to the predictive power of generalized struvite precipitation models, as evidenced by a 90% confidence interval for Ω of over an order of magnitude in width (Figure 2.7). This uncertainty is most heavily dependent on the orthophosphate K_{a3P} and on the solubility product for struvite, K_{sp} .

Results of the Monte Carlo model show that despite the underlying uncertainty, precipitation can be accurately modeled within a range of values. Field data drawn from a representative, struvite-heavy wastewater environment confirm this conclusion and offer a real-world example of the utility of uncertainty modeling.

The use of deterministic models and single equilibrium constants without considering uncertainty has been shown to be insufficient for struvite precipitation prediction. Furthermore, though limited to struvite, the findings of this research warrant the evaluation of uncertainty for solubility in general.

Chapter 3

The Struvite Precipitation Index: A Practical Framework for Predicting Struvite Supersaturation in Water and Wastewater

3.1 Chapter Summary

In wastewater facilities, struvite ($\text{MgNH}_4\text{PO}_4 \cdot 6\text{H}_2\text{O}$) precipitation and subsequent accumulation within sludge processing can be either an expensive nuisance or a pathway to orthophosphate reclamation and beneficial reuse. Predictive solubility models developed in the past have been computationally intensive and highly conservative, and have employed uncertain equilibrium constants for the evaluation of solution saturation. The StrPI (Struvite Precipitation Index) developed in this study is a new, computationally light framework for predicting struvite precipitation based on saturation pH. The model permits process-specific calibration (i.e. StrPI plus a correction pH) to deal with the highly variable characteristics of wastewater streams and to eliminate the pH-independent overprediction inherent in existing solubility models. Verification of this model was performed across a range of waste compositions, ionic strengths, and root-mean-square velocity gradients using data from both synthetic laboratory experiments and field tests. The StrPI framework was found to be an effective and uncomplicated predictor of struvite precipitation in both environments.

This chapter has been published in a peer-reviewed journal, as cited by [Barnes et al. \(2018\)](#).

3.2 Introduction

Struvite ($\text{MgNH}_4\text{PO}_4 \cdot 6\text{H}_2\text{O}$) is one of the most prevalent and expensive nuisance precipitates within digestion and postdigestion processes in municipal wastewater treatment. Crystals will readily form on pipes, mixers, and submerged equipment, often costing plants hundreds of thousands of dollars per year in replacement parts and maintenance costs ([Ohlinger et al., 1998](#); [Mamais et al., 1994](#); [Horenstein et al., 1990](#); [Benisch et al., 2000](#)). Recent technologies such as the OstarTM and AirPrex[®] processes have been developed to intentionally precipitate struvite for phosphate and nitrogen recovery, which provides a means to produce a high-value, slow-release fertilizer ([Melia](#)

et al., 2017; Ye et al., 2017). Whether struvite is considered a nuisance or an opportunity, highly variable concentrations and uncertain equilibrium parameters make modeling struvite precipitation an academically and computationally rigorous endeavor, as was explored in Barnes & Bowers (2017). While moderately effective at predicting precipitation within a range of uncertainty, existing models are highly conservative. As shown in Barnes & Bowers (2017), this conservatism often underestimates the pH of precipitation by more than an order of magnitude. As a result, operators waste resources in an effort to keep pH, magnesium, phosphate, or ammonia at unnecessarily low levels.

In most municipal wastewater plants, day-to-day processes are monitored and controlled by operators on site. These operators are expected to change plant operating parameters to react to variable conditions within the processes, be it increasing/decreasing additive doses, mixer speeds, flow rates, etc. While often highly skilled in their field, plant operators are not expected to have the necessary chemistry and engineering background to execute complex precipitation models to consider uncertainties.

As wastewater stream composition often fluctuates—sometimes rapidly—operators need an efficient method to predict struvite precipitation. Such a method should be readily translated into adjustments of operating parameters such as pH and alkalinity, both of which are easily controllable, similar to the Langelier Saturation Index for calcium carbonate (Tchobanoglous et al., 2013).

This study proposes and evaluates a struvite precipitation metric, the StrPI (Struvite Precipitation Index), to evaluate the actual pH of struvite saturation. In its simplest form, this proposed metric is defined as:

$$StrPI = pH - pH^* \quad (3.1)$$

where pH is the current solution pH and pH^* is the pH of struvite saturation. Then, $StrPI > 0$ implies supersaturation, < 0 implies undersaturation (where struvite does not precipitate), and 0 implies struvite is at equilibrium.

3.3 Uncertainty

As discussed in depth in [Barnes & Bowers \(2017\)](#), the three primary sources of model uncertainty—variable wastewater composition, measurement errors, and disagreement between published equilibrium parameters—have a marked effect on the certainty and predictive bounds of equilibrium models. Concentrations measured from individual grab samples are commonly used in predictive wastewater models ([Ohlinger et al., 1998](#); [Doyle & Parsons, 2002](#)), as is common in academic analyses. However, operational predictions of struvite precipitation require a site-specific understanding of the variability of solution pH and concentrations of magnesium, orthophosphate, and ammonium.

In [Barnes & Bowers \(2017\)](#), an equilibrium model that accounted for waste-stream variability and known uncertainty was found to be effective, though slightly conservative, in predicting struvite precipitation onto metal coupons placed within a conventional centrate nitrification basin. This method, while valuable, requires a level of plant-specific statistical nuance and computational analysis that would be untenable in normal day-to-day operations. Models that rely on empirical calibration and grab-sample data may be less comprehensive, but they allow rapid, informed analysis to be readily applied to active treatment facilities. The struvite precipitation index was developed to be robust enough to maintain predictive power across variable waste streams, but simple enough to be used in day-to-day operations.

3.4 Precipitation Potential

Precipitation of struvite is the result of a difference in the chemical potential of the salt in a supersaturated solution, μ_s , and the chemical potential of the salt at equilibrium, μ_∞ . This difference, $\Delta\mu$, can be given as:

$$\begin{aligned}
\Delta\mu &= \mu_\infty - \mu_s \\
&= [\mu_\infty^0 + kT \ln(\alpha_{Mg^{2+}} \cdot \alpha_{NH_4^+} \cdot \alpha_{PO_4^{3-}})_\infty^{1/3}] \\
&\quad - [\mu_s^0 + kT \ln(\alpha_{Mg^{2+}} \cdot \alpha_{NH_4^+} \cdot \alpha_{PO_4^{3-}})_s^{1/3}]
\end{aligned} \tag{3.2}$$

where k is the Boltzmann constant, T is absolute temperature, and α_i is the ion fraction of each component (Bouropoulos & Koutsoukos, 2000). More specifically:

$$\alpha_i = \frac{\text{free ion concentration}}{\text{concentration of water-based species}} \tag{3.3}$$

Assuming that the standard state chemical potentials are equal, or $\mu_\infty^0 = \mu_s^0$, then

$$\Delta\mu = kT \ln \left[\frac{(\alpha_{Mg^{2+}} \cdot \alpha_{NH_4^+} \cdot \alpha_{PO_4^{3-}})_\infty^{1/3}}{(\alpha_{Mg^{2+}} \cdot \alpha_{NH_4^+} \cdot \alpha_{PO_4^{3-}})_s^{1/3}} \right] = -\frac{kT}{3} \ln(\Omega) \tag{3.4}$$

where Ω is the supersaturation ratio as developed by Bouropoulos & Koutsoukos (2000):

$$\Omega = \frac{Mg_f \cdot N_f \cdot P_f}{K_{spcond}} \tag{3.5}$$

where Mg_f , N_f , and P_f are molar concentrations of free magnesium, ammonia (as N), and orthophosphate (as P), respectively, and α_i is the ion fraction for each component. K_{sp} is the solubility product for struvite, and K_{spcond} is the pH-conditional struvite solubility product, given by Stumm & Morgan (1994), Ohlinger et al. (1998), Doyle & Parsons (2002), Snoeyink & Jenkins (1980), and Ali & Schneider (2008):

$$K_{spcond} = \frac{K_{sp}}{\alpha_{Mg^{2+}} \cdot \alpha_{NH_4^+} \cdot \alpha_{PO_4^{3-}}} \tag{3.6}$$

Following the theory,

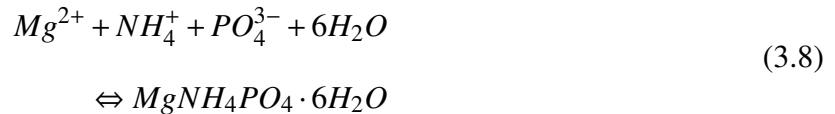
$$\begin{aligned}\Omega > 1 &\Rightarrow \text{supersaturation} \\ \Omega < 1 &\Rightarrow \text{undersaturation}\end{aligned}\tag{3.7}$$

Disregarding any limiting kinetics, a supersaturated solution (i.e. $\Omega > 1$) implies that precipitation will occur. This Ω factor is the method by which the StrPI is calculated in this study; however, Ω is simply a diagnostic ratio and carries no inherent probabilistic information. Expectations attributed to Ω must be derived empirically on a case-by-case basis due to dissimilarities between wastewater streams and kinetic inconsistencies between processes.

When evaluating struvite precipitation using Ω calculations, plants may determine and maintain a buffer zone (e.g. keep Ω below 0.5 rather than 1.0 to eliminate precipitation). However, this correction does not scale with solution pH and cannot be applied consistently across variable waste streams. The introduction of a pH-based struvite precipitation index, a parameter more easily calculated and conceptualized than Ω , will simplify plant operations. Further, pH is usually the only parameter that is readily within operator control and thus is a superior unit for model predictions (and calibrations)—as exemplified by the industrywide ubiquity of the Langelier Saturation Index for calculating calcium carbonate saturation ([Tchobanoglous et al., 2013](#)).

3.5 Equilibrium Chemistry

Struvite precipitation occurs in solutions where available magnesium, ammonium, and phosphate ions exceed the struvite solubility limit at a given pH, or:



Several studies have investigated struvite solubility at equilibrium, and all generally agree on the form of the struvite solubility product ([Ohlinger et al., 1998](#); [Barnes & Bowers, 2017](#); [Doyle &](#)

Parsons, 2002; Stumm & Morgan, 1994; Snoeyink & Jenkins, 1980; Ali & Schneider, 2008):

$$K_{sp} = [Mg_f][N_f][P_f](\alpha_{Mg^{2+}})(\alpha_{NH_4^+})(\alpha_{PO_4^{3-}}) \quad (3.9)$$

where K_{sp} is the struvite solubility product at equilibrium and $K_{sp_{cond}}$ is the pH-conditional solubility product. For ammonium, orthophosphate, and magnesium, the ionization fractions are described as a function of pH as follows:

$$\alpha_{NH_4^+} = \frac{[H^+]}{[H^+] + K_{a1N}} \quad (3.10)$$

$$\alpha_{PO_4^{3-}} = \frac{PO_4^{-3}}{P_f} = \frac{K_{a1P} \cdot K_{a2P} \cdot K_{a3P}}{[H^+]^3 + (K_{a1P} \cdot [H^+]^2) + (K_{a1P} \cdot K_{a2P} \cdot [H^+]) + (K_{a1P} \cdot K_{a2P} \cdot K_{a3P})} \quad (3.11)$$

$$\alpha_{Mg^{2+}} = \frac{Mg^{2+}}{Mg_f} = \frac{1}{1 + K_{1Mg} \cdot [OH^-]} \quad (3.12)$$

The total dissolved species concentrations (Mg_T , N_T , and P_T) are:

$$Mg_T = Mg_f + MgPO_4^- + MgHPO_4 + MgH_2PO_4^+; \quad (3.13)$$

$$N_T = N_f = NH_3 + NH_4^+ \quad (3.14)$$

and,

$$P_T = P_f + MgPO_4^- + MgHPO_4 + MgH_2PO_4^+; \quad (3.15)$$

which includes:

$$Mg_f = Mg^{2+} + MgOH^+ + Mg(OH)_2 + Mg(OH)_3^- \quad (3.16)$$

$$P_f = H_3PO_4 + H_2PO_4^- + HPO_4^{2-} + PO_4^{3-} \quad (3.17)$$

where Mg_f and P_f represent the free magnesium and orthophosphate species, respectively, and K_{sp} ,

K_{a_1P} , K_{a_2P} , K_{a_3P} , K_{a_1N} , K_{1Mg} , K_{MgP} , K_{MgHP} , and K_{MgH_2P} are experimentally derived equilibrium constants reported in the literature.

These ionization fractions are highly pH-dependent. Over the operating range of a typical wastewater treatment plant, from pH 6.0 to 8.5, struvite solubility decreases significantly as pH increases. In addition to full reactor supersaturation, struvite may precipitate in localized areas of a treatment process. This may occur around caustic discharge tubes or due to localized pH increases from CO₂ volatilization in low-pressure zones around venturis, pipe bends, and mixing blades. The StrPI may be uniquely useful in mitigating precipitation in these zones if they are characterized individually, as operators can check the pH of their processes against a set of localized pH constraints.

In highly saline water (ionic strength > 1.0 M), Eq. (3.12) may not be representative of field conditions as chloride/magnesium complexes such as MgCl⁺ may form. In typical wastewater, however, where [Cl⁻] ≤ 0.5 M and [Mg²⁺] ≤ 0.1 M, these complexes would comprise less than 2% of total magnesium and may subsequently be disregarded as negligible. Where magnesium and chloride concentrations are high, MgCl⁺ can form; consequently, struvite may precipitate more sparingly than predicted.

3.5.1 Equilibrium Constants

In addition to the struvite equilibrium constant, K_{sp} , precipitation is controlled by eight equilibrium equations that together define the speciation of the three principal constituents, PO₄³⁻, NH₄⁺, and Mg²⁺. These eight equilibrium constants are given by:

$$K_{a_1P} = \frac{[H^+][H_2PO_4^-]}{[H_3PO_4]} \quad (3.18)$$

$$K_{a_2P} = \frac{[H^+][HPO_4^{2-}]}{[H_2PO_4^-]} \quad (3.19)$$

$$K_{a_3P} = \frac{[H^+][PO_4^{3-}]}{[HPO_4^{2-}]} \quad (3.20)$$

$$K_{a_1N} = \frac{[H^+][NH_3]}{[NH_4^+]} \quad (3.21)$$

$$K_{1Mg} = \frac{[Mg^{2+}][OH^-]}{[MgOH^+]} \quad (3.22)$$

$$K_{MgP} = \frac{[Mg^{2+}][PO_4^{3-}]}{[MgPO_4^-]} \quad (3.23)$$

$$K_{MgHP} = \frac{[Mg^{2+}][HPO_4^{2-}]}{[MgHPO_4]} \quad (3.24)$$

$$K_{MgH_2P} = \frac{[Mg^{2+}][H_2PO_4^-]}{[MgH_2PO_4^+]} \quad (3.25)$$

Similar constitutive equations for equilibrium calculations are employed in most published struvite research, but generally use individual, deterministic equilibrium constants (Ohlinger et al., 1998; Doyle & Parsons, 2002; Stumm & Morgan, 1994; Snoeyink & Jenkins, 1980; Ali & Schneider, 2008). Values reported in literature for the nine equilibrium constants vary widely, and the effects of these inconsistencies on model uncertainty were found to be nontrivial.

Barnes & Bowers (2017) developed a Monte Carlo uncertainty model for struvite, which included associated probability evaluations of plant-specific field data. These results were used to inform the development of the StrPI. However, as variation between waste streams precludes the application of uncertainty calculations from one treatment plant to the next, the struvite precipitation index was developed without the incorporation of the data-driven uncertainty analyses that have characterized former studies. Instead, a generalized method to integrate plant-specific uncertainty into the StrPI is proposed and evaluated.

3.5.2 Solubility Product Simplifications

Once the available fractions of aqueous $[Mg^{2+}]$, $[NH_4^+]$, $[PO_4^{3-}]$ are evaluated at solution pH, these fractions can then be used to calculate the pH-conditional struvite solubility product, $K_{sp_{cond}}$, as described in Eq. (3.6). Because plant and process-specific uncertainties prohibit the formulation of a general probabilistic solution, the conditional solubility product was calculated as a deterministic value derived from published equilibrium constants. Specifically, as outlined in Barnes & Bowers

(2017), the published literature constants described in Eqs. (3.9)-(3.25) were used as uniformly distributed Monte Carlo inputs, and Eq. (3.6) was simulated to evaluate all equilibrium constant uncertainties. The median model value from this simulation can be seen as the dashed line in Fig. 3.1. The $pK_{sp_{cond}}$ is derived from theory and published laboratory data—not field measurements—so it can be standardized for all processes. The quality of this fit can be seen when compared to two prominent struvite studies that evaluated $K_{sp_{cond}}$ in the laboratory (Musvoto et al., 2000; Ohlinger et al., 2000).

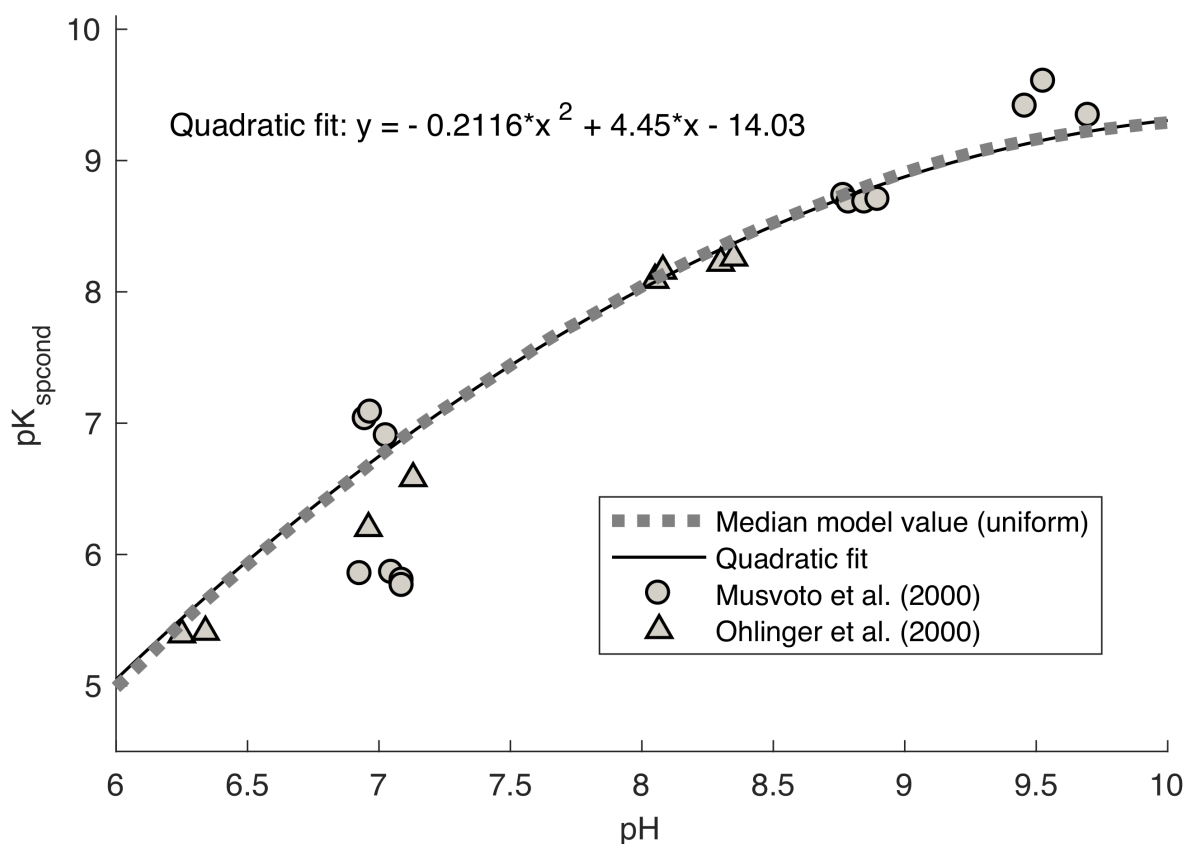


Figure 3.1: Median $pK_{sp_{cond}}$ predicted at 25°C and 0.1 M ionic strength by the uniform Monte Carlo model described in Barnes & Bowers (2017). Curated datasets of nine published equilibrium parameters (K_{sp} , K_{a1P} , K_{a2P} , K_{a3P} , K_{a1N} , K_{1Mg} , K_{MgP} , K_{MgHP} , and K_{MgH2P}) were used to evaluate Eq. (3.6). The discrete data points used for comparison were taken from two prominent struvite studies that evaluated $K_{sp_{cond}}$ in the laboratory (Musvoto et al., 2000; Ohlinger et al., 2000).

A quadratic polynomial, shown in Fig. 3.1 as a solid line, was fit to the simulated $pK_{sp_{cond}}$. As this quadratic fit demonstrated exceptional agreement with the calculated $pK_{sp_{cond}}$ and significantly

reduces the computational power and theoretical knowledge necessary for StrPI estimations, it was selected as a simplification of the equilibrium model. This pH-dependent quadratic fit is given by:

$$pK_{sp_{cond}} = -0.2116pH^2 + 4.45pH - 14.03 \quad (3.26)$$

where $pK_{sp_{cond}}$ is the negative base-10 logarithm of $K_{sp_{cond}}$. Coefficients have been truncated for readability and ease of use, and the effects of these truncations were found to be negligible when compared to model precision. The maximum deviation of the quadratic fit from the comprehensive model of [Barnes & Bowers \(2017\)](#) over pH 6.0 to 8.5 occurs at pH 6.0, and the $pK_{sp_{cond}}$ estimate deviates by less than 1 percent—a more than sufficient fit given other uncertainties. The use of $pK_{sp_{cond}}$ instead of $K_{sp_{cond}}$ to develop the fit avoids human and machine computational problems with the use of small decimal coefficients. It also maintains graphical readability.

The model, as described in Eq. (3.26), was developed for solutions at 25°C and 0.1 M ionic strength. The robustness of this simplification over different temperatures and ionic strengths is explored later.

3.5.3 Struvite Precipitation Index

The Ω supersaturation ratio, given by Eq. (3.5), may now be rewritten to incorporate the quadratic approximation of $K_{sp_{cond}}$:

$$\Omega = \frac{Mg_T \cdot N_T \cdot P_T}{10^{(0.2116pH^2 - 4.450pH + 14.03)}} \quad (3.27)$$

To formulate a general equation for the StrPI model, Eq. (3.27) must be reorganized to identify the pH at which Ω equals exactly 1.0, defined in this paper as pH^* . More specifically, pH^* is defined by the theoretical point of saturation (where $Mg_T \cdot N_T \cdot P_T = K_{sp_{cond}}$). The conversion between water-based species (Mg_f, N_f, P_f) and total dissolved species (Mg_T, N_T, P_T) is possible because over the fitted pH range, magnesium phosphate species are negligible (thus making the free and total dissolved concentrations equivalent). Without the computational expense of a rigorous $K_{sp_{cond}}$

model, pH^* can be easily calculated. First, set $\Omega = 1$ and rearrange Eq. (3.27), or:

$$0 = 0.2116pH^{*2} - 4.450pH^* + 14.03 - \log_{10}(Mg_T \cdot N_T \cdot P_T) \quad (3.28)$$

then employ the quadratic equation and simplify.

$$pH^* = 10.52 - 2.363 \sqrt{7.928 + 0.8464 \log_{10}(Mg_T \cdot N_T \cdot P_T)} \quad (3.29)$$

Combining Eq. (3.29) with Eq. (3.1), we can calculate the theoretical, or uncalibrated, struvite precipitation index (*StrPI*) as:

$$StrPI = pH - 10.52 + 2.363 \sqrt{7.928 + 0.8464 \log_{10}(Mg_T \cdot N_T \cdot P_T)} \quad (3.30)$$

where pH is the current solution pH and Mg_T , N_T , and P_T are total dissolved magnesium, ammonia (as N), and orthophosphate (as P) concentrations measured in mol/L in a filtered wastewater sample. As with pH, the units of the StrPI are dimensionless.

Eq. (3.30) is considered uncalibrated as it consistently returns values significantly above zero when precipitation is observed in both the lab and the field. This is simply a translation of the significant—but pH- and concentration-independent—conservative overprediction seen in the underlying Ω model. This over-prediction may be due to uncertainties in equilibrium constants, impacts of non-ideal temperatures and ionic strengths, the kinetics of precipitation, or a combination of all three. Eq. (3.30) can be further expanded to incorporate concentrations as mg/L (as opposed to M), the more common units of water and wastewater operations:

$$StrPI = pH - 10.52 + 2.363 \sqrt{-3.095 + 0.8464 \cdot \log_{10}(Mg_{mg/L} \cdot N_{mg/L} \cdot P_{mg/L})} \quad (3.31)$$

where $Mg_{mg/L}$, $N_{mg/L}$, and $P_{mg/L}$ are total dissolved magnesium, ammonia (as N), and orthophosphate (as P) concentrations measured in mg/L in a filtered wastewater sample.

In theory, the calculated *StrPI* predictions should be evaluated as:

$$\begin{aligned}
StrPI > 0 &\Rightarrow \text{precipitation} \\
StrPI < 0 &\Rightarrow \text{no precipitation}
\end{aligned}
\tag{3.32}$$

However, because of the uniform, conservative bias exhibited across all $StrPI$ values (using C as a correction factor between theory and field observations),

$$\begin{aligned}
StrPI > 0 + C &\Rightarrow \text{precipitation} \\
StrPI < 0 + C &\Rightarrow \text{no precipitation}
\end{aligned}
\tag{3.33}$$

where C is a calibration term applied uniformly to all $StrPI$ values. Preliminary experiments suggested a C value near 1.0; however lab- and field-based estimations of C (and, thus, Ω over-prediction) are discussed later in terms of a calibrated StrPI. This final corrected model, $StrPI_c$, incorporates the C term and thus may be calibrated for any system (including T , I , slow kinetics, or other uncertainty). That this calibration is necessary may be attributable to the kinetic effects that maintain a supersaturated solution, inaccurate equilibrium constants as explored in [Barnes & Bowers \(2017\)](#), or even a system of more complex precipitation dynamics. This study does not investigate the source of this uniform correction (C); however, it does seek to quantify and utilize it in the StrPI model.

3.6 Methods

Described in Eq. (3.30), the StrPI uses a basic polynomial fit to represent the complexities of struvite solubility in a form that can be readily evaluated during regular treatment operations. This research draws its value from its accuracy in predicting struvite precipitation within the range of potential wastewater composition/complexity. However, as shown in field tests performed by [Barnes & Bowers \(2017\)](#), the existing models for struvite precipitation (i.e. those derived from the Ω model from [Bouropoulos & Koutsoukos \(2000\)](#)) are highly conservative in practice, i.e., overpredict precipitation.

Preliminary bench-scale experimentation also exhibited this overprediction. This suggested that a full-scale analysis of struvite precipitation across a representative range of potential wastewaters would serve to confirm the veracity of the StrPI framework's representation of the $K_{sp_{cond}}$. Such a study would also allow for an analysis of the conservative inaccuracy of existing models and development of a possible correction factor/technique/method.

Full-scale analysis was performed using data from both synthetic laboratory experiments and from field data. Synthetic wastewater allowed the $StrPI/StrPI_c$ to be tested against a wider range of wastewater compositions in a more controlled environment, while field sampling tested the model's efficacy *in situ* and helped identify any practical limitations.

3.6.1 Methods for Synthetic Solutions

Synthetic aqueous solutions were prepared in a Phipps and Bird PB-900 Series programmable jar tester with square, 2-liter jar-test beakers. Use of these jar testers, an industry standard across American water and wastewater facilities, allow the following experiments to be repeated by utilities using site-specific wastewater compositions. These beakers and associated metal stirrers are designed to create a fully mixed environment with a known velocity gradient curve (Lai et al., 1975; Cornwell & Bishop, 1975). This ensures mixation at predetermined root-mean-squared velocity gradients, G , s^{-1} .

Room temperature (approximately 25°C) deionized water and various concentrations of ammonia, phosphate, and magnesium were added as ammonium chloride, potassium phosphate, and magnesium chloride, respectively, to create conditions that led to a $StrPI$ near zero at various potential wastewater pH levels. Sodium chloride was also added in different concentrations to simulate background ionic strength, and the jar-tester mixing speed was varied to evaluate the impact of the velocity gradient.

Constituents were weighed and added in powder form. This was necessary since constituent solubility at high concentrations made the use of stock solutions less feasible using 2-liter beakers. After sodium chloride was added to the deionized water and fully dissolved for background ionic

strength, ammonium chloride and potassium phosphate were then added, as they dissolve more slowly than magnesium chloride. The pH was then modified to 6.50 using dilute 0.1 N NaOH. Solutions with higher phosphate alkalinity required the addition of a higher volume of base to achieve the same pH change. This consequently introduced slightly elevated ionic strengths in high-phosphate synthetic solutions compared to other solutions at the same *StrPI*. This difference was assumed to be negligible, although ionic strength impacts will be addressed later. Once the pH was set at 6.50, magnesium chloride was added.

After all constituents dissolved, the pH was increased by increments of 0.10 units using 0.1 N NaOH until precipitation was observed. In cases where precipitation occurred at intermediate pH values (not multiples of 0.10) ascribed to partial or imprecise NaOH additions, the pH of precipitation was recorded to two decimal places.

When added dropwise to a phenolphthalein indicator solution mixed at $G = 100 \text{ s}^{-1}$ and a pH of 8.0, 0.1 N NaOH did not create pinkish plumes. This was not always true for 1 N NaOH, for which pinkish plumes ($\text{pH} > 9$) were observed. Solutions that did not create pinkish plumes were assumed to be sufficiently mixed without localized areas of elevated pH (high transient values of *StrPI* > 0). This assumption was also evaluated at $G = 18 \text{ s}^{-1}$, with similar results.

If the solution was highly supersaturated by a pH change, struvite usually precipitated heavily within the first minute; however, solutions near saturation occasionally took several minutes to show signs of precipitation, possibly due to nucleation kinetics. Each unprecipitated solution state was therefore allowed to mix for 10 minutes at each pH step. Filtered samples were taken prior to precipitation to confirm concentrations of added constituents, and after precipitation to confirm an equal reduction in molar concentration of each constituent (as is expected with struvite).

In these experiments where synthetic wastewater was used, struvite precipitation was treated as a binary condition (precipitated/not precipitated), where precipitates were identified visually or by the formation of turbidity using a HACH 2100P portable turbidimeter. Precipitation was further confirmed by a distinct drop in pH caused by equilibration as phosphate, PO_4^{3-} , was removed to form struvite. These results were then verified using ICAP-MS on filtered and unfiltered acidified

samples to confirm that an equal molar ratio of magnesium and phosphate were removed from the aqueous system.

Dried-sample X-ray powder diffraction (XRD) was conducted to confirm that the precipitate was entirely struvite. The XRD measurements were performed using a Scintag XGEN-4000 X-ray diffractometer with a $CuK\alpha$ ($\lambda = 0.154$ nm) radiation source. The molecular structure was then determined by comparing the diffraction patterns to literature data (International Union of Crystallography database). The scans were run from 10-80 degrees in 2Θ with a 0.1 degree step size and 10 second dwell time, and all samples were found to be exclusively struvite.

A series of these precipitation experiments was run to examine the effects of constituent concentrations on struvite solubility. Jars were prepared using concentrations ranging from 1×10^{-3} to 1×10^{-1} M as Mg, P, and N. These concentration limits addressed individual solubility limitations: constituent additions greater than 1×10^{-1} M approach saturation and tend not to fully dissolve. Moreover, concentrations of less than 1×10^{-3} M meant that the change in turbidity/concentrations/pH could not be evaluated consistently in the jar-tester. These concentration ranges encompass the vast majority of potential scenarios within municipal wastewater facilities. Within this envelope, the constituent concentrations were each evaluated at semi-regular intervals of 1×10^{-3} M, 2.5×10^{-3} M, 3.5×10^{-3} M, 5×10^{-3} M, 8×10^{-3} M, 1×10^{-2} M, 2.5×10^{-2} M, 3.5×10^{-2} M, 5×10^{-2} M, 8×10^{-2} M, and 1×10^{-1} M. As a result of the nonlinear pH response of struvite precipitation, the use of regular measurement intervals resulted in clustered StrPI vs. pH data. These semi-regular intervals were selected to permit the thorough evaluation of the StrPI across the range of typical wastewater concentrations and pHs .

Magnesium was not added above a concentration of 5×10^{-2} M because of concerns about magnesium chloride solubility and the influence of concentrated chloride and magnesium ions on ionic strength. Since Mg^{2+} is often the limiting reactant for struvite formation in municipal waste, as measured in [Barnes & Bowers \(2017\)](#) and [Doyle & Parsons \(2002\)](#), this will likely have no effect on the applicability and evaluation of the model.

The three constituents were added in a variety of triplicates to simulate a wide range of waste

compositions and to confirm the conclusion of [Bouropoulos & Koutsoukos \(2000\)](#) that no particular constituent(s) contributed disproportionately when they were present in more than the 1:1:1 stoichiometric ratio. Both the $StrPI_c/StrPI$ and the underlying Ω model of [Bouropoulos & Koutsoukos \(2000\)](#) rely on this assumption when solubility is calculated as a function of the product of $[Mg]$, $[P]$, and $[N]$.

Constituent triplicates were added following one of seven templates:

1. Equal molar concentrations: $[Mg] = [P] = [N]$
2. $[Mg]$ 10 \times higher than $[P]$ and $[N]$: $[Mg] = 10 \times [P] = 10 \times [N]$
3. $[P]$ 10 \times higher than $[Mg]$ and $[N]$: $[P] = 10 \times [Mg] = 10 \times [N]$
4. $[N]$ 10 \times higher than $[Mg]$ and $[P]$: $[N] = 10 \times [Mg] = 10 \times [P]$
5. $[Mg]$ 10 \times lower than $[P]$ and $[N]$: $[Mg] = 0.1 \times [P] = 0.1 \times [N]$
6. $[P]$ 10 \times lower than $[Mg]$ and $[N]$: $[P] = 0.1 \times [Mg] = 0.1 \times [N]$
7. $[N]$ 10 \times lower than $[Mg]$ and $[P]$: $[N] = 0.1 \times [Mg] = 0.1 \times [P]$

This method allowed each constituent to serve as the stoichiometrically limiting or oversupplied molecule in the reaction, maintained order to the data, and evaluated $StrPI$ across a large range of typical wastewater compositions.

The jars were initially mixed at pH 6.5 with a root-mean-square velocity gradient of 100 s^{-1} (100 rpm), 44 s^{-1} (50 rpm), or 18 s^{-1} (25 rpm) using the Phipps and Bird PB-900 Series shear-rated paddles. Experimentation was limited to the regions between pH 6.5 and 8.5 because these are standard operating ranges for treatment processes that exhibit struvite. Notably, this is the envelope over which struvite constituents remain soluble at the concentrations used but are still concentrated enough to accurately measure precipitation by means of turbidity and the associated pH drop

Individual experiments were run using either 0.01, or 0.5 M background ionic strength—added as NaCl—to evaluate the StrPI over a range representative of wastewater.

3.6.1.1 Temperature Simplifications

Solution temperature has the potential to significantly affect the solubility of struvite, as discussed in [Aage et al. \(1997\)](#), [Hanhoun et al. \(2011\)](#), and [Bhuiyan et al. \(2007\)](#). While published values of struvite solubility product at different temperatures would ideally serve to inform an empirical model such as the StrPI, the uncertainty in equilibrium constants renders analysis difficult. For example, using the dataset for the pK_{sp} of struvite compiled in [Barnes & Bowers \(2017\)](#) and comprised of data from [IUPAC \(2011\)](#), [Hanhoun et al. \(2011\)](#), and [Ohlinger et al. \(1998\)](#), the temperature variability of the pK_{sp} over the range of 15 to 40°C is on the same order of magnitude as the uncertainty derived from inconsistencies in published equilibrium constants at 25°C. This is best represented in Fig. 3.2, where literature values for the struvite pK_{sp} evaluated at zero ionic strength are plotted against their associated temperatures.

As is apparent in Fig. 3.2, beyond a possible linear correlation between temperature and the pK_{sp} , conclusions cannot be drawn without more agreement between published solubility constants. Consequently, thermal effects were not included in this study. However, it is assumed that temperature will be appropriately modeled with the *StrPI_c*.

Research performed by [Hanhoun et al. \(2011\)](#) using a smaller dataset of published pK_{sp} values found that over the temperature range of 15 to 35°C, pK_{sp} values ranged from 13.29 (± 0.02) to 13.08 (± 0.06). In a similar study, [Bhuiyan et al. \(2007\)](#) found pK_{sp} values ranged from 14.04 (± 0.03) to 13.20 (± 0.03) over the same temperature range. These values are highly dissimilar, but both studies generally agree that an increase in temperature over this range results in increased struvite solubility.

Actual wastewater streams can exhibit seasonal, diurnal, and spatial temperature variations; further model calibration may be required when stream temperatures deviate significantly from 25°C. This is especially true for colder solutions when the aim is to prevent precipitation, as thermal functionality will slightly lower solubility. However, as waste streams generally do not undergo significant temperature changes over short periods of time, consistent model calibration will likely mitigate these effects.

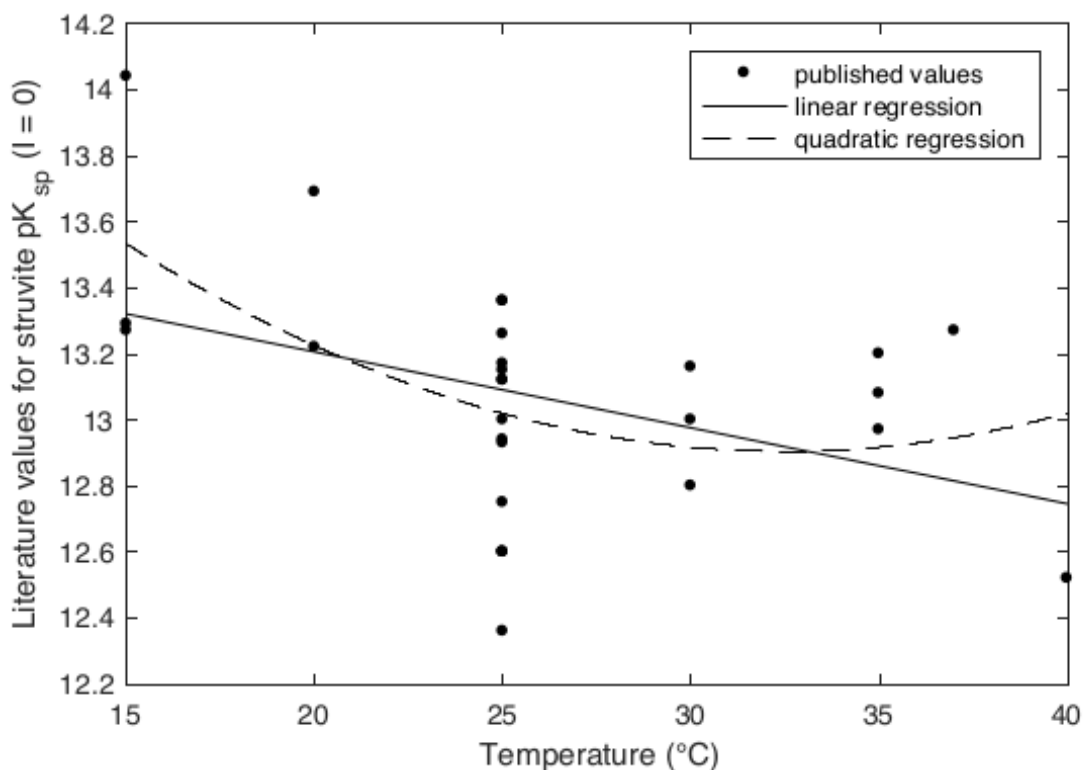


Figure 3.2: Literature values for for the pK_{sp} of struvite from IUPAC (2011), Hanhoun et al. (2011), and Ohlinger et al. (1998) are plotted against their associated temperatures. The plotted data points were taken only from published constants measured in solutions of zero ionic strength, as such solutions are the most widely reported by a substantial margin (allowing for a larger dataset). Linear (solid line) and quadratic (dashed line) least-squares regressions had adjusted R-squared values of 0.131 and 0.257, respectively. Higher order polynomial regressions fit with similarly poor results. This degree of uncertainty in published pK_{sp} values precludes deeper insight into temperature functionality.

3.6.1.2 Impact of Kinetics

The kinetics of struvite precipitation are difficult to predict and model, especially in solutions near the point of saturation. In identical supersaturated solutions, time to precipitation may differ by minutes, possibly as a result of small errors in measurements or non-homogeneity due to experimental imperfections. Further, the colloidal chemistry of struvite particle formation can be broken into three distinct phases—nucleation, coagulation, and flocculation—each controlled by different wastewater properties and exhibiting highly dissimilar rates of foulant agglomeration (Elimelech et al., 1998; Weber & DiGiano, 1996). The diagram in Fig. 3.3 depicts the relative

rates of struvite formation/accumulation as well as the pertinent wastewater properties influencing each phase. It is possible that the short-term efficacy of the StrPI equilibrium model will be more affected by the slower nucleation phase (associated with constituent concentrations and pH) than the coagulation phase (influenced by critical coagulation concentration and ionic strength), since the slower colloid formation processes inherently take longer to reach equilibrium.

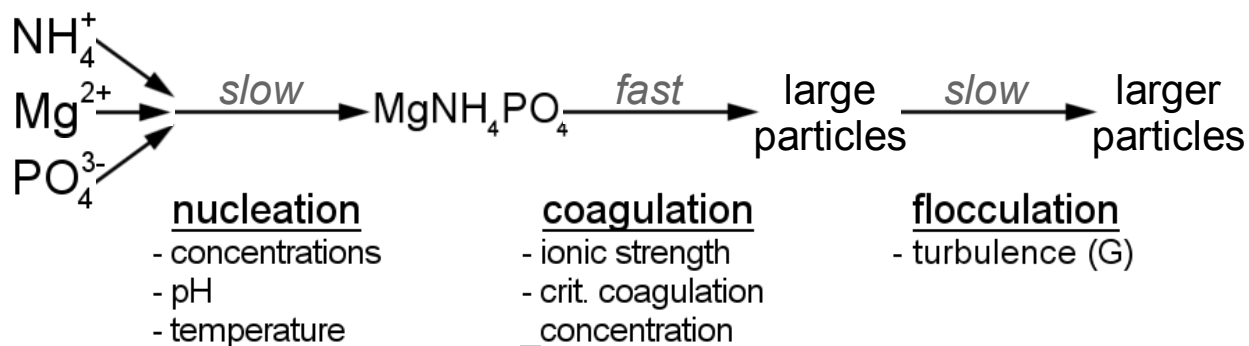


Figure 3.3: A schematic outlining the three phases of struvite formation (and accumulation) and their relative kinetic rates (Elimelech et al., 1998; Weber & DiGiano, 1996). The impactful wastewater properties are labeled for each phase.

For the sake of specificity, this research did not focus on kinetics, but relied instead on long mixing times and the simplicity of binary precipitation data to reduce its effects on the data. However, in variable wastewater systems kinetics may cause a cycle of precipitation and dissolution. This may go unnoticed or be impossible to record within a Boolean framework.

Laboratory and field scale experimentation performed in this study and in Barnes & Bowers (2017) found that the Ω model presented in Bouropoulos & Koutsoukos (2000) was highly conservative, often predicting precipitation almost a full pH point before it was observed. Solution kinetics are likely only one of many factors that affect these predictions; nevertheless, the ability to calibrate the StrPI to incorporate kinetic effects is imperative to model flexibility.

3.6.2 Methods for Field Experiments

Considering the variety of conditions present in a wastewater treatment plant (Barnes & Bowers, 2017), laboratory-scale experimentation does not necessarily translate to the field. Before it can

be used, the StrPI must be shown to be applicable to field cases. A field test was performed in the centrate nitrification basins ($\text{NH}_4^+ \rightarrow \text{NO}_3^-$) of a struvite-burdened metropolitan wastewater treatment facility. Aluminum coupons were placed at eight critical locations around a conventional plug-flow aeration basin and water samples were taken several times a day at each point. The 415-meter-long (1,360 ft) basins contained treated centrate from anaerobically digested wastewater sludge and had an average residence time of approximately two days. Concentrations of the main constituents of struvite (generally: $\text{NH}_4^+ > \text{PO}_4^{3-} > \text{Mg}^{2+}$) varied greatly over time due to inconsistency in the centrate source. Struvite formed throughout the basins, but predominantly in locations of localized pH spikes caused by CO_2 stripping or caustic addition. The wastewater pH was initially raised to around 7.0 prior to nitrification to ensure biological activity. The influent also included flow from the main aeration basins (bacterial seed) and a recycle stream from the tail end of the centrate basins (about 1 million gallons per day each).

When struvite crystals precipitated onto the metal coupons over a set period, they were dissolved in acid and the constituents were analyzed using ICAP-MS (inductively coupled argon plasma mass spectrometry). An example of a fouled coupon (precipitation present) can be seen in Fig. 3.4. In all cases, the magnesium-to-calcium ratio exceeded 100:1 and chloride was found to be negligible. More importantly, the Mg:P ratio indicated struvite as the major precipitate. To confirm, XRD measurements were performed; the sample was found to be predominantly struvite.

The field experiment was performed for two weeks, with eight samples taken daily from the nitrification basin at points near submerged coupons. Measurements of ammonia and phosphate were performed on site using a LaMotte 1200 colorimeter with a sensitivity of 0.05 ppm $\text{NH}_3\text{-N}$ and 0.05 ppm $\text{PO}_4^{3-}\text{-P}$. Magnesium was measured using an ICAP Q ICP-MS in accordance with [Rice et al. \(2012\)](#). A Fisher Scientific accumet AP85 portable pH meter was used to measure the pH. The temperature was measured as approximately 25 °C with only minor variability, and the average ionic strength was estimated using Eq. (3.34) and grab-sample measurements of solution electrical conductivity (EC, in $\mu\text{S/m}$).

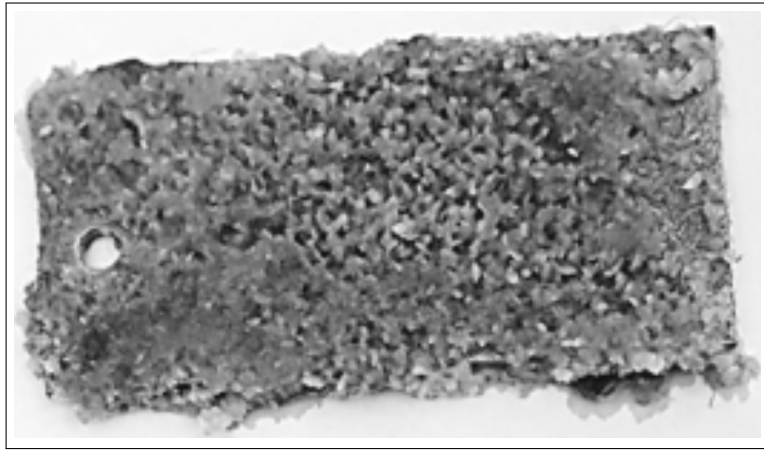


Figure 3.4: Coupon fouled with struvite from field experiments. This specific coupon was submerged at a point 325 feet (99 meters) along a nitrification basin and removed after two weeks' contact time.

$$\log I = 1.159 + 1.009 \log EC \quad (3.34)$$

valid for $I \leq 0.3$ M (Sposito, 2008; Ancheyta, 2017).

Conductivity was measured five times over two weeks, with variability of less than 20 percent between samples. Ionic strength was estimated as approximately 0.1 M ($\pm 10\%$). The conditions for supersaturation over the two weeks were evaluated by the StrPI model using the coupon precipitation data in conjunction with the pH and constituent concentration measurements. The rate of struvite crystal redissolution has not been evaluated, but it is likely slower than the rate of precipitation due to layering effects and localized areas of elevated constituent concentrations around solid particles. Consequently, it is likely that the maximum value (or a high percentile, such as the 90th) of measured pH and constituent concentrations are more useful in long-term fouling predictions than average values.

3.7 Laboratory Results

3.7.1 Approximating Measurement Error

Struvite precipitation in synthetic solutions near saturation is affected by localized kinetics, concentration inhomogeneities, and general measurement errors—all of which contribute inescapable uncertainty in any predictive model. However, such a model may also exhibit uncertainty and inaccuracy through the effects of various simplifications and assumptions. Should the model simplification errors fall within the acceptable predictive range, then the effects of the simplification or assumption can be deemed negligible for the purposes of practical application.

Each jar-test evaluation of the StrPI framework resulted in a measured pH of precipitation. Eq. (3.30) and experiment-specific concentration values were then used to calculate $StrPI$ at the point of precipitation (which was not 0, as predicted theoretically), denoted as $StrPI^*$. For a calibrated StrPI model, precipitation should occur at $StrPI_c = 0$ for all experimental conditions; however, $StrPI^*$ includes the conservatism of the Ω model, so the uncalibrated values are much higher—generally nearer to 1.0. The $StrPI^*$ inaccuracies are partitioned into two statistically independent components: measurement errors and model simplification errors. For a set of $StrPI^*$ precipitation data, S^* , the variance of the set can be written as the sum of the variances of the two components (Ang & Tang, 2007), or:

$$Var(S^*) = Var(ME) + Var(\varepsilon) \quad (3.35)$$

where ME represents the measurement errors, ε represents the model errors, and the Var function denotes the variance of its argument. $Var(ME)$ was estimated by evaluating the difference between the measured $StrPI^*$ of duplicate experiments, each sharing identical concentrations of $[Mg]$, $[P]$, and $[N]$ as well as identical background ionic strengths and mixing speeds.

These $StrPI^*$ residuals were calculated from a series of 27 duplicate pairs containing a wide range of constituent triplicates and ionic strengths, all at a G of 100 s^{-1} . As duplicate experiments contain the same model error, ε , the variance of the residuals is entirely due to the variance of

measurement error. Following [Ang & Tang \(2007\)](#), this relationship can be used to estimate $Var(ME)$:

$$Var(ME) \approx \frac{Var(R)}{2} \quad (3.36)$$

where R is an array of $StrPI^*$ residuals between duplicate experiments.

For the synthetic experiments, ME was found to have a variance of 0.017, which results in a standard deviation of approximately 0.131 pH units. This is within the range of acceptable model uncertainty, especially as temporal and localized wastewater variability would generally negate the value of a more accurate model. A one-sample Student's t-test ($p = 0.05$) was performed on R and the residuals were found to be approximately normally distributed. The estimated measurement error was subtracted from the right side of Eq. (3.35) to calculate ε . This facilitates investigations into the effects of ionic strength and root-mean-square velocity gradient simplifications of the StrPI.

3.7.2 Ionic Strength Analysis

Ions added as a byproduct of increasing pH (by adding NaOH) or added as ammonium chloride, potassium phosphate, or magnesium chloride, were rendered negligible by the addition of 0.01 M or 0.50 M NaCl as swamping ionic strength, I . The maximum value of I (0.50 M) was not set to a higher value because of concerns about magnesium chloride interference at more concentrated doses. Nonetheless, both the addition of constituents and the pH modification during experimentation cause an inherent increase in the ionic strength of the solution. In cases involving precipitation at a relatively low pH (i.e. well below 7.0) and 0.01 M background NaCl, the necessary elevated constituent levels may overcome the background ionic strength's swamping effect and reach non-background ion concentrations comparable to that supplied by the NaCl.

While ionic strength is an important modeling consideration, in wastewater it can be highly dissimilar between individual plants (magnitude and composition) and between periodic grab samples. Moreover, ionic strength is generally estimated using conductivity measurements—a method understood to introduce some uncertainty. This research is meant to simplify the prediction of

struvite precipitation so that the StrPI can be approximated promptly, and the exhaustive experimentation required to include an ionic strength factor can be eliminated. Nonetheless, the effect of ionic strength variability between experimental runs was assessed.

Preliminary experiments suggested that solution ionic strength has a small to negligible effect on measured $StrPI^*$ over the range of experimental constituent concentrations. This result suggests that ionic strength effects can be assessed by evaluating the model at its boundary conditions. Time-intensive experiments that use a grid of ionic strengths to span the model's expected practical range, as was done with constituent concentrations, can thus be eliminated. This analysis at boundary conditions again collects pairs of "duplicate" solutions ($[Mg]$, $[P]$, and $[N]$ ranging from 1×10^{-3} to 1×10^{-1} M); however, in this case, the background ionic strength of one duplicate is added at 0.01 M, while the other is added at 0.50 M.

This method does not model the functional effects of ionic strength on $StrPI^*$. Instead, it quantifies the impact of the effect across a range of probable wastewater conditions. As published solubility products suggest that the relationship between $K_{sp_{cond}}$ and ionic strength contains no inflection points over the model range, the use of maximum and minimum values for I should encapsulate the range's full breadth of ionic strength interference on $StrPI^*$ (IUPAC, 2011).

An analysis of variance on the $StrPI^*$ data using a linear fixed effects model was performed to evaluate the effects of ionic strength, as is discussed later. As the ionic strength was evaluated at only one of two values, the condition of background ionic strength was converted to a binary value I_x , set at 1 for $I = 0.01$ M and 0 for $I = 0.50$ M.

3.7.3 Root-Mean-Square Velocity Gradient Analysis

Past field studies have evaluated the range of wastewater turbulence within municipal treatment facilities. These studies reported values in the form of the root-mean-square velocity gradient, G , a common measure of mixing intensity generally used to define flocculation. Specifically, Das et al. (1993) ran a comprehensive field study of the effects of the root-mean-square velocity gradient on a full-scale activated sludge wastewater treatment plant that evaluated and expanded upon the

conclusions of [Parker et al. \(1971\)](#). While these papers suggested that ideal flocculation occurs at a G between 20-70 s^{-1} , G values measured in the aeration basins of 14 full-scale treatment plants were much higher, resulting in a general range of 88-220 s^{-1} ([Das et al., 1993](#)). Additionally, [Das et al. \(1993\)](#) measured the G in mixed liquor transport systems and found that values ranged between 1 and 72 s^{-1} .

The *StrPI** baseline experiments performed in this study were run at 100 revolutions per minute (rpm). From the Phipps and Bird documentation, at room temperature this imparts a homogeneous root-mean-square velocity gradient, G , of 100 s^{-1} . This value was selected as it allowed for adequate mixing of the added constituents, fit within the range supplied by [Das et al. \(1993\)](#) for aeration basins, and would not create a large vortex.

To examine the specific effects of G on struvite precipitation, the 100 rpm experiments were replicated using G values of 18 s^{-1} (25 rpm) and 44 s^{-1} (50 rpm). For the $G = 18 \text{ s}^{-1}$ experiment runs, constituents were rapidly mixed at a low pH to allow for faster dissolution. However, the paddle speed was slowed before the pH was brought above 6.5.

The impact of turbulence on precipitation was determined by employing the same method that was used with ionic strength. Specifically, 34 slowly mixed (25 rpm) solutions were compared to 34 quickly mixed (100 rpm) but otherwise identical solutions. The velocity gradient was also treated as a binary value, G_x , for use in the linear fixed effects model: 100 s^{-1} was set as $G_x = 1$ and 18 s^{-1} was set as $G_x = 0$.

Unlike the ionic strengths included in I_x , the selected G values are not meant to encompass the entire range of potential turbulence within a treatment plant. They do, however, represent a significant difference in root-mean-square velocity gradient and encompass the entire “ideal aeration basin” span of 20-70 s^{-1} described in [Das et al. \(1993\)](#) and [Parker et al. \(1971\)](#). Should the difference between these two mixing rates have no significant effect on *StrPI*, it is unlikely that values outside this range would differ.

We note that turbulence simulated using synthetic precipitation does not encompass all impacts of mixing rates in the field. Specifically, in an open-air wastewater process, localized areas with

high velocity gradients may evolve and release CO₂ at faster rates than are occurring in the bulk solution. This can cause small pockets of elevated pH which inherently exhibit higher *StrPI** values than are predicted by bulk-flow pH measurements. In these cases, the StrPI may be calibrated to the local areas of elevated pH, or a safety factor may be implemented independently of the StrPI equation.

3.7.4 Analysis of StrPI Using a Linear Fixed Effects Model

There are two principal factors of interest: ionic strength and mixing speed. To quantify the impact of these two factors, a standard linear fixed effects model was fit to the data and an associated analysis of variance was carried out (Walpole et al., 2002):

$$StrPI^* = aI_x + bG_x + intercept \quad (3.37)$$

where *StrPI** is the measured *StrPI* at precipitation; *I_x* is the binary set representing ionic strengths of *I* = 0.01 and *I* = 0.50 as 1 and 0, respectively; *G_x* is the binary set representing root-mean-square velocity gradients of 100 s⁻¹ and 18 s⁻¹ as 1 and 0, respectively; and *a*, *b*, and *intercept* represent fitted constants. As the binary *I_x* and *G_x* variables span the range of expected ionic strength and turbulence values, respectively, *a* and *b* represent the magnitude of each factor's impact on the measured *StrPI** (e.g. a larger *a* value means a larger expected difference between the *StrPI** in solutions of 0.01 M vs. 0.50 M ionic strength). The *intercept* coefficient represents the magnitude of the uniform bias in the uncalibrated StrPI model that causes precipitation to not occur at StrPI* = 0 (not a function of ionic strength and mixing speed).

A regression algorithm was used to minimize the sum of the squares of the errors for all *StrPI** data with initial conditions included within *I_x* and *G_x* (77 runs). The results of this fit can be seen in Table 3.1.

Table 3.1: Regression results for linear fixed effects model of measured $StrPI^*$ values described in Eq. (3.37). The p -value is calculated for a null hypothesis where the coefficient is equal to zero. Coefficients a and b apply to the binary I_x and G_x data, not I or G , and thus should not be used to estimate functionality. Instead, the estimates simply compare the change in $StrPI^*$ when I or G vary between their max and min values.

Coefficient	Estimate	Std error	t-Stat	p -Value
a	0.0453	0.0408	1.11	0.271
b	-0.0182	0.0384	-0.473	0.637
intercept	1.16	0.0340	34.1	5.14×10^{-47}

Num. Obs.	MSE	RMSE
77	0.0162	0.127

3.7.4.1 Estimation of Model Uncertainty

The root mean squared error (RMSE) was evaluated for the 77 experimental runs. This value, 0.127, serves as an approximation of the standard deviation of the regression errors and is comparable to 0.131, the approximate standard deviation of measurement error calculated using Eq. (3.36). The similarity between these two values suggests that the fixed effects model sufficiently captured the model error, ε . This absence of unexplained error also implies that using the product of [Mg], [P], and [N] to model saturation, as suggested by [Bouropoulos & Koutsoukos \(2000\)](#), is robust when evaluated at different stoichiometric ratios.

3.7.4.2 Impacts of Ionic Strength and Velocity Gradient

The least-squares estimates for the I_x and G_x coefficients, a and b , were both small. Moreover, the estimates had a standard error of similar magnitude. The associated p -values also failed to reject the null-hypotheses of both $a = 0$ and $b = 0$ (using a level of significance, α , of 0.05), meaning the coefficients are statistically indistinguishable from zero. This suggests the difference in saturation points between solutions with 0.01 and 0.50 M background ionic strength is insignificant (accounting for an estimated 0.045 unit shift of pH^*). The same conclusion can be drawn about saturation between solutions where $G = 100 \text{ s}^{-1}$ and $G = 18 \text{ s}^{-1}$. It must be noted that “statistically

insignificant" is not equivalent to "has no effect". It is possible that ionic strength and mixing speed have slight effects on struvite precipitation over their expected ranges, but these impacts are swamped by measurement errors during statistical analysis. Nonetheless, I and G are unlikely to affect practical applications.

A second set of mixing speed duplicate residuals (44 vs. 100 s^{-1}) was used in the fixed effects model to confirm the viability of root-mean-square velocity gradient assumptions across the 18 s^{-1} to 100 s^{-1} envelope. This second set compared 21 moderately turbulent solutions (44 s^{-1} , $G_x = 0$) to 21 highly turbulent ones (100 s^{-1} , $G_x = 1$). This analysis also failed to reject the null hypothesis, which supports the conclusions of the first G_x set. In conclusion, the effect of ionic strength and mixing speed over the model's applicable range is statistically indistinguishable from zero, and I and G terms can be justifiably excluded from the StrPI model.

3.7.4.3 Estimating Bias in the Uncalibrated Model

In addition to a and b , the fixed effects analysis outlined in Table 3.1 estimated the y-intercept of the linearized $StrPI^*$ model. Calculated as 1.16, *intercept* represents the magnitude of the uniform overprediction of an uncalibrated model. This bias can be observed in Fig. 3.5, where the dataset of $StrPI^*$ values included in the fixed effects model is plotted against solution pH at precipitation, pH^* . The mean $StrPI^*$ is approximately 1.16, whereas an ideal calibrated prediction, $StrPI_c^*$, should have a mean near zero.

The bias in Fig. 3.5 highlights the need for model calibration. It also suggests an estimate of the StrPI calibration value, C , described in Eq. (3.33). The value of *intercept* from Table 3.1 serves as a good initial guess for C ; however, it does not take into account the site-specific requirements of the model, i.e., setting the calibration to eliminate either false negatives or false positives. Specifically, in efforts to prevent struvite scaling, an ideal calibration would see precipitation occur at or above the point where $StrPI_c = 0$. Likewise, in efforts to facilitate struvite precipitation, the selected C should be higher than 1.16 to allow precipitation to occur before $StrPI_c = 0$. The exact value should be set in consideration of the necessary level of certainty.

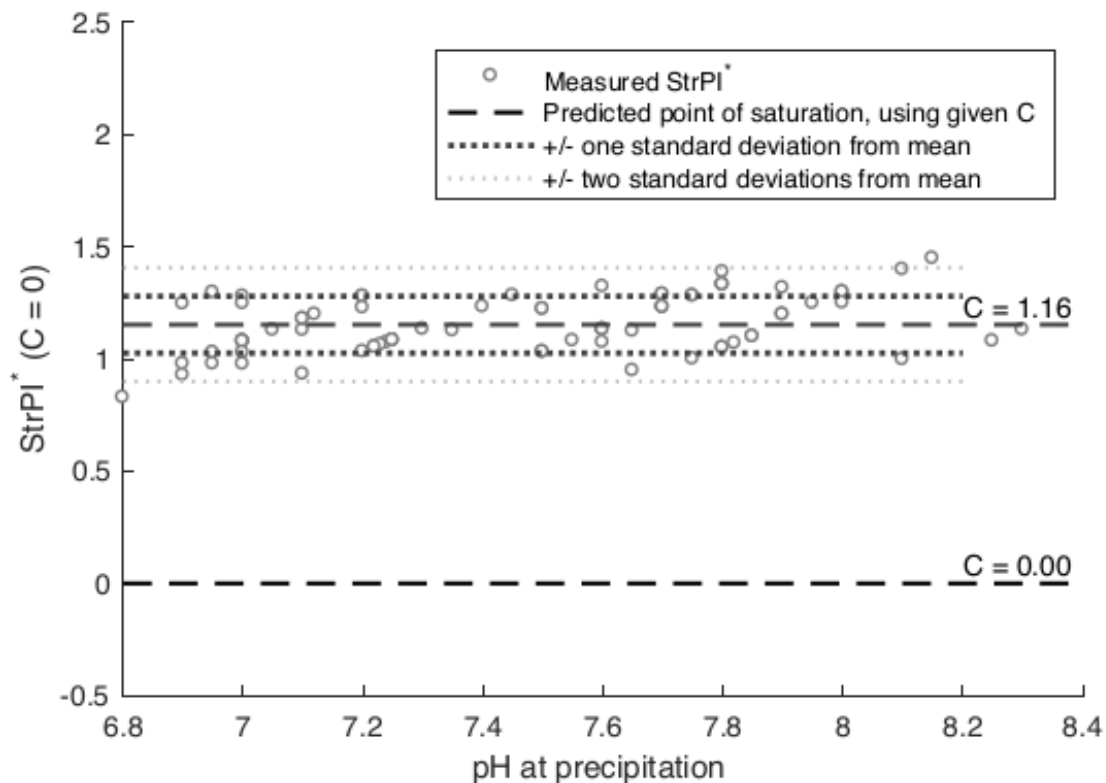


Figure 3.5: The calculated $StrPI^*$ vs. actual measured pH of precipitation for all synthetic struvite precipitation experiments included in the fixed effects model (77 points). The estimated bias, $intercept = 1.16$, and associated error bars were drawn from the synthetic experiments. Many of the data points are coincident or stratified as a result of identical duplicate pairs and the 0.10 unit resolution of pH measurements.

Fig. 3.6 contains the normal probability plot of all measured $StrPI^*$ values generated from the synthetic precipitation experiments. It indicates that StrPI prediction uncertainty at known initial conditions is approximately normally distributed.

Using the linear effects model outlined in Table 3.1, the uncertainty of the StrPI model was estimated to have a standard deviation of 0.127 pH units. Paired with the assumption of normality, this value was used to represent model uncertainty associated with StrPI predictions. These can be seen in Fig. 3.5, where dashed lines are drawn at ± 1.0 and ± 2.0 standard deviations from the mean.

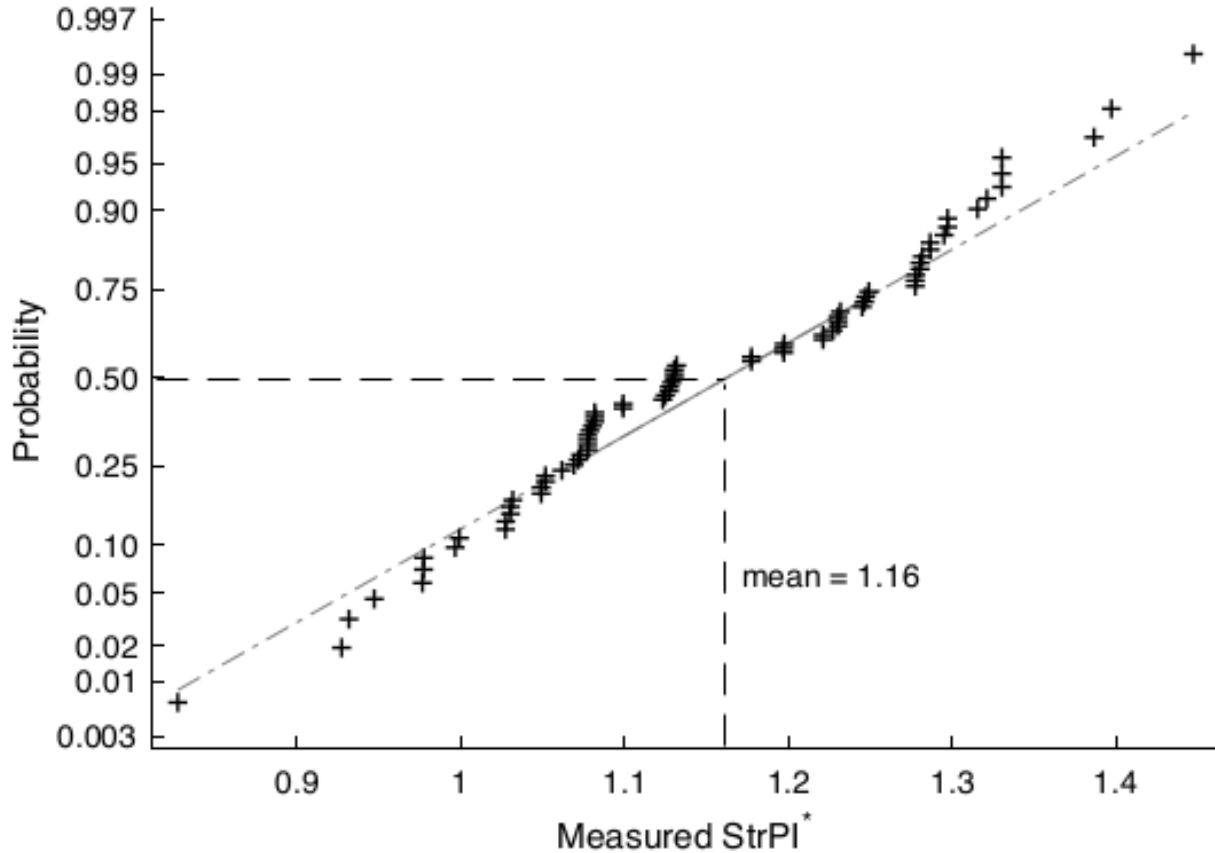


Figure 3.6: The normal probability plot of all measured $StrPI^*$ values generated from the synthetic precipitation experiments. The assumption of normality was supported by a one-sample Student's t-test ($\alpha = 0.05$).

3.7.5 Calibration Using Synthetic Results

The $StrPI$ model was developed specifically to permit field calibration of the generalized $StrPI$ equation. As these calibrations are performed by operators, they can accommodate for plant- or process-specific irregularity and nuance that is not captured by universal models. This calibration factor can be added to Eqs. (3.30) or (3.31) to establish a calibrated $StrPI$, $StrPI_c$:

$$StrPI_c = pH - C - 10.52 + 2.363 \sqrt{7.928 + 0.8464 \log_{10}(Mg_T \cdot N_T \cdot P_T)} \quad (3.38)$$

where pH is the measured pH of the waste stream and C , the $StrPI$ calibration factor, corrects for the uniform bias in an uncalibrated model. C is a single number, likely positive, that can be adjusted

to allow for less (or more) conservative predictions. While a least-squares fit of the synthetic experiments estimated that $C = 1.16$, this distributes uncertainty equally about the mean—which is not necessarily ideal for use in operations. The model should be recalibrated (i.e., C should be adjusted) to incorporate the specific predictive needs of individual treatment plants. Concentrations are in mol/L as [Mg], [N], and [P].

Conversely, using concentrations in mg/L:

$$StrPI_c = pH - C - 10.52 + 2.363 \sqrt{-3.095 + 0.8464 \log_{10}(M_{mg/L} N_{mg/L} P_{mg/L})} \quad (3.39)$$

The two subplots in Fig. 3.7 contain the calibrated $StrPI_c^*$ vs. measured pH at precipitation for all synthetic precipitation experiments included in the fixed effects model. Calculations of $StrPI_c$ were calculated using a C value of 0.90 in the top subplot and 1.42 in the bottom subplot. These values represent two standard deviations below and above the mean ($C = 1.16$), respectively. The data in Fig. 3.7 are well represented within ± 2 standard deviations, where about 95% of normally distributed data should fall.

3.7.6 Calibration-Updated Solubility Product

A uniform shift in the expected pH of precipitation to accommodate empirical results is a viable engineering solution to an uncertain situation. The bias corrected by C may be a result of several factors. Those factors can include kinetics, inhomogeneities, or—at least in part—because of an incorrect assumption of K_{sp} . A comparison of the quadratic fit of $pK_{sp_{cond}}$ to a quadratic fit corrected by subtracting C can be used to examine the solubility product implications of the model calibration. The magnitude of the effects of calibration can be seen in Fig. 3.8, where the $pK_{sp_{cond}}$ and $K_{sp_{cond}}$ of an uncalibrated model ($C = 0$) are compared to a calibrated model where $C = 1.16$.

The highly uncertain equilibrium constants described in Chapter 2 may contribute to the bias; however, the published pK_{sp} values at 25 °C and $I = 0$ have a range of about one order of magnitude and a mean of 12.96. As such, it is unlikely the large $pK_{sp_{cond}}$ ratios displayed in Fig. 3.8 are a result of equilibrium constant uncertainty alone, if at all. The overprediction of precipitation is

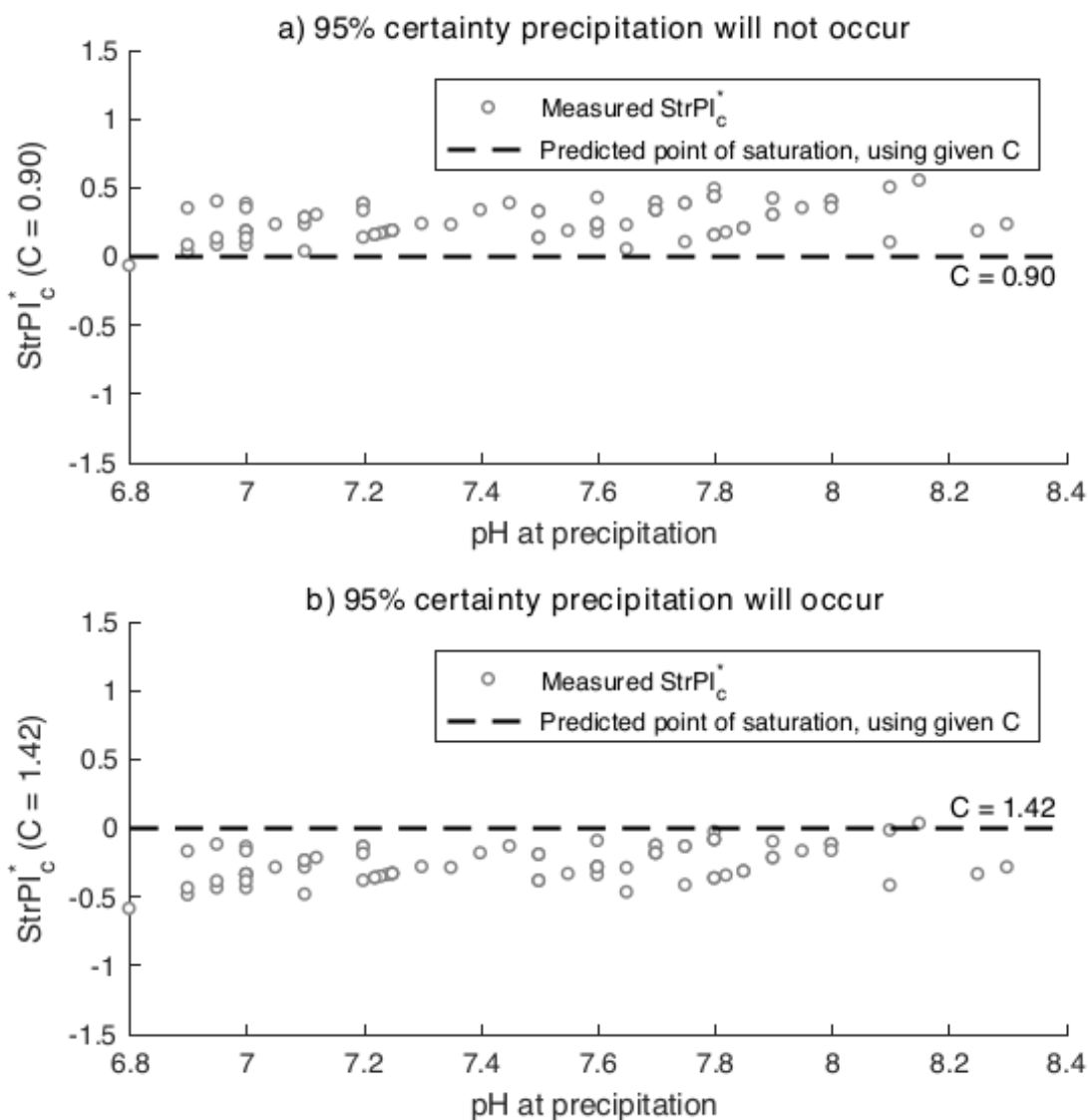


Figure 3.7: The calculated $StrPI_c$ vs. measured pH of precipitation and associated error for all synthetic struvite precipitation experiments included in the fixed effects model (77 points). For (a), the calibration factor, C , is set to 0.90—two standard deviations below the least-squares estimate of C . This calibration was selected so there is 95% certainty that precipitation will occur when $StrPI_c > 0$ (reasonable for preventing precipitation). For (b), C is set to 1.42—two standard deviations above the least-squares estimate of C (reasonable for facilitating precipitation). Note, many of the data points are coincident or stratified as a result of the identical duplicate pairs and the 0.10 unit resolution of pH measurements.

likely in part due to kinetics, and the conditional solubility products presented in Fig. 3.8 may be markedly different from those derived through comprehensive chemical analysis.

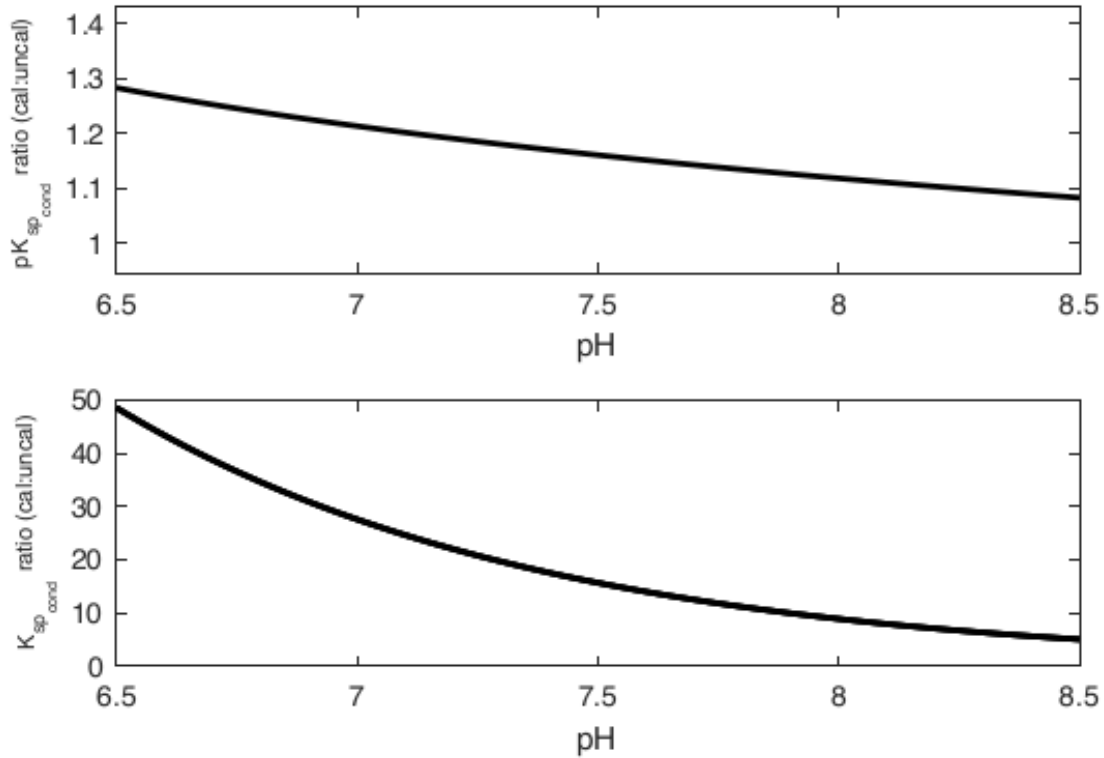


Figure 3.8: The ratio of a calibrated StrPI model ($C = 1.16$) to an uncalibrated model ($C = 0$). On the upper subplot, the two $pK_{sp_{cond}}$ values were evaluated using the simplified $pK_{sp_{cond}}$ model outlined in Eq. (3.26) over the pH range of 6.5 to 8.5. This value is converted to the $K_{sp_{cond}}$ on the lower subplot.

Following the calibration of the StrPI to synthetic solutions and the conclusion that it is functionally independent of G and I for practical purposes, the model was verified using real wastewater samples at an operating treatment plant.

3.8 Precipitation in Field

3.8.1 Field Results

Coupons were placed in reactors where struvite scaling could realistically occur. The $StrPI_c$ model ($C = 0.90$) accurately predicted long-term scaling in the field when using measured values (90th percentile of pH, [Mg], [P], and [N]) at each coupon location as inputs. This can be seen in Fig. 3.9, where the 90th percentile is represented by the top of the error bars. The specific choice of

90 percent is unsubstantiated outside of the field data's quality of fit; however, it is reasonable to use the worst-case scenario for $StrPI_c$ inputs (e.g. 90th percentiles of measurements) if preventing precipitation is critical. It should be noted, it is unlikely that 90th percentile values of pH, [Mg], [P], and [N] will occur concurrently in a wastewater stream, and the error bars likely enclose well over 99.9% of potential $StrPI_c$ values. The predictions fit without false negatives or positives when using values one standard deviation above the mean (approx. 66th percentile), but this will vary between treatment facilities. When the $StrPI_c$ is applied to a new treatment process, the distributions of waste stream concentrations should be evaluated to ensure they are not heavily skewed in a way that would undermine predictions. Also, the model should be recalibrated if precipitation does not occur near a $StrPI_c$ of zero.

As shown in Fig. 3.9, solutions evaluated using the 90th percentile of measurements never resulted in precipitation when the $StrPI_c$ was less than zero. Further, the same predictions also correctly anticipated struvite buildup on three of five coupons where the calculated $StrPI_c$ was greater than, or within, one standard deviation of zero.

3.8.2 Suggested Initial Calibration Values

The StrPI calibration value, C , was found to be 1.16 when fit using least-squares regression on the lab data. This calibration, which appears to fit well using the 90th percentile of field measurements, does not take into account the predictive needs of all situations. If a system is designed to precipitate struvite—the OstaraTM or AirPrex[®] processes, for example—then ideal calibration would ensure precipitation rather than its absence. Specifically, it might use a C greater than 1.16 to err on the side of underprediction and reduce the prevalence of false positives. Conversely, if a waste stream is highly variable, localized areas are particularly problematic, or minimal struvite precipitation is especially detrimental, a conservative C may be ideal. For example, C could be set so low that an $StrPI_c$ of zero falls several standard deviations above the lab-derived estimation of the saturation point.

The $StrPI_c$ model requires that C be set based on localized conditions. Its validity, therefore,

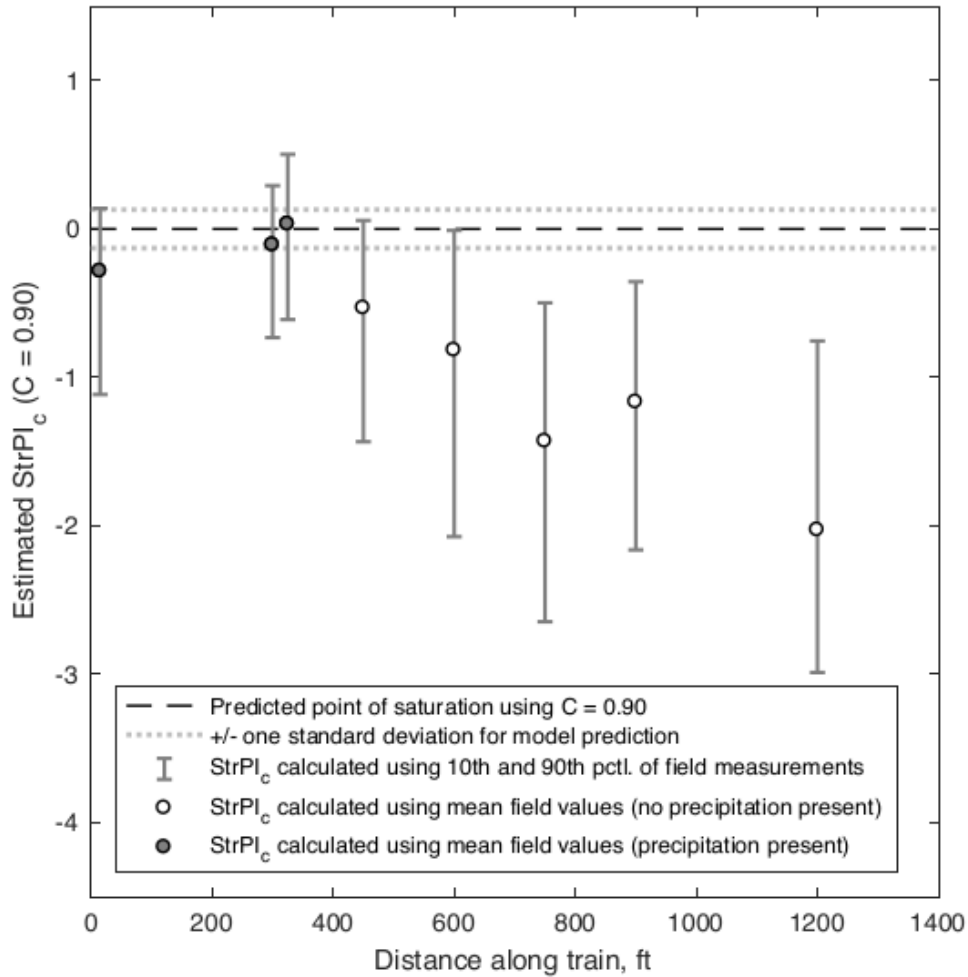


Figure 3.9: Field results for eight coupons submerged along a 415-meter (1,360-ft) centrate nitrification basin, each evaluated for the existence of struvite precipitation. Temperature was 25°C ($\pm 2^{\circ}\text{C}$). The dashed line denotes the expected point of precipitation for the calibrated model ($StrPI_c = 0$) using a C of 0.90 (empirical fit from lab experiments). Dotted lines denote a model confidence interval of \pm one standard deviation. The error bars depict the estimated range of the $StrPI_c$ over the two-week experiment, calculated using 10th and 90th percentile of measured pH, [Mg], [P], and [N] values. Both circular markers represent the $StrPI_c$ evaluated at the mean values of each set of pH, [Mg], [P], and [N].

should be periodically assessed and updated to reflect changing field conditions. Lab-scale experimentation similar to that laid out in this study can be used to quickly analyze new waste conditions and adjust calibration accordingly. However, situational inhomogeneity and the potential for CO_2 evolution require that the primary metric for calibration be the observation of precipitation within actual processes. Precipitation can be evaluated through use of coupons (as discussed in this study),

through chemical analysis of grab samples, or through the continued telltale accumulation of crystals on mixers, pipes, and other problem areas.

Initially, the C value should be set at a point that reflects the safety factor (or other predictive needs) of the individual process, and the model should be recalibrated when new data sets become available or aqueous conditions change substantially. Increasing the value of C will make the $StrPI_c$ predictions less conservative (precipitation occurs at a lower $StrPI_c$), and vice versa. The initial implementation of $StrPI_c$ can be simplified through use of these calibration guidelines, drawn from this study's field and laboratory experiments. Using measured pH, [Mg], [P], and [N] data:

$$\begin{aligned} C = & \dots \\ 0 \Rightarrow & \text{uncalibrated and highly conservative} \\ 0.90 \Rightarrow & \text{struvite prevention (95\% certainty of no precipitation when } StrPI_c < 0) \\ 1.04 \Rightarrow & \text{calibrated to 90th pctl. of field data (lowest } C \text{ with no false positives)} \\ 1.16 \Rightarrow & \text{calculated using least squares regression of lab data (centered on error)} \\ 1.42 \Rightarrow & \text{struvite recovery (95\% certainty of precipitation when } StrPI_c > 0) \end{aligned} \tag{3.40}$$

Statements of certainty apply to equilibrium model fit, not to the variability of the waste stream. The underlying distributions of measured model inputs and the selection of which percentile to use for said inputs (e.g. 90th percentile) may significantly impact model effectiveness. Future research may look to evaluate the $StrPI_c$ in variable waste conditions using a Monte-Carlo framework, similar to that discussed in [Barnes & Bowers \(2017\)](#).

The $StrPI_c$ model is designed to be used as a predictive tool that can be useful for general operational decisions, not as an analytical refinement of existing theory. Model flexibility, therefore, is more important than finding a single, unifying equation. The use of a single additive calibration constant to modulate predictions over a wide pH range streamlines $StrPI_c$ framework implementation, shortens the learning curve for plant operators, and simplifies in-the-moment calculations.

3.9 Conclusions

The struvite precipitation index is useful for wastewater operations as an accessible metric for evaluating the potential of an aqueous system to precipitate struvite (either to prevent or promote struvite precipitation). While this effort was restricted to a pH range of 6.0 to 8.5, it was shown synthetically to be effective in its predictions. This conclusion was verified through a complex field case.

A calibration constant, C , was included in the $StrPI_c$ equation to accommodate plant-specific kinetics, uncertainty, inhomogeneity, and a desired factor of safety. Jar-test results suggest an initial calibration of $C = 1.42$ to promote struvite precipitation and $C = 0.90$ to prevent it. The $StrPI_c$ is modeled as a function of $[Mg]$, $[N]$, and $[P]$ (each as mol/L in Eq. (3.38) or mg/L in Eq. (3.39)) and solution pH. The approach was verified in a field case, and $StrPI_c$ predictions were found to fit best when using the 90th percentile values of concentrations derived from distributions of waste stream measurements.

It is possible to adapt the StrPI equation to processes that are highly dissimilar to those tested in this study. Refinements could accommodate abnormal pH levels, ionic strengths, and turbulence. Other equation adaptations could accommodate significant localized pH spikes due to carbonate evolution or extreme differences between $[Mg]$, $[N]$, and $[P]$. As presented, however, the StrPI equation can serve as a valuable tool for municipal wastewater treatment plants where struvite scaling is a problem or where nutrient reclamation is being performed. Process-specific calibration allows a user to account for stream uncertainty and variability in a flexible and robust manner. Lastly, the StrPI can be a useful tool to predict the potential effects of process-specific factors, including constituent spikes, upstream pH modulation, and other significant changes in plant operations. Currently, these conditions can only be assessed after precipitation has occurred or through the use of highly conservative computer models.

Chapter 4

Empirical Model for the Dissolution of Magnesium Hydroxide Slurries in Water and Wastewater Treatment

4.1 Introduction

A variety of chemical additives are used in water and wastewater treatment for pH and alkalinity control. Typical additives to raise (or maintain) pH and alkalinity include caustic (NaOH), lime (CaO or Ca(OH)₂), sodium bicarbonate (NaHCO₃), and sodium carbonate (Na₂CO₃). Most commonly, NaOH or Ca(OH)₂ are used (Tchobanoglous et al., 2013). However, many of these common additives hinder the performance or increase operating costs of downstream processes in the treatment plant. For example, the use of lime is often curtailed because it can cause temporary hardness that precipitates as calcium carbonate, which leads to nuisance boiler scale in drinking water. This calcium carbonate also forms additional inorganic solids for disposal in wastewater processes, especially as biodegradation occurs, or (Tchobanoglous et al., 2013; Hendricks, 2010):



and:



where CaCO₃ ↓ indicates precipitation.

Recently, magnesium hydroxide has gained more attention for use in water and wastewater due to cost, increased availability, non-hazardous properties, and several process advantages it has over the most common additives, namely:

1. Mg(OH)₂ adds permanent hardness, i.e., MgCO₃ is much more soluble than CaCO₃, so there is no nuisance boiler scale or solids production in water or wastewater treatment (Lide, 1991).

2. Compared to sodium, Na^+ , Mg^{2+} is a beneficial mineral with far fewer side effects, and is generally considered by health professionals as being an undersupplied nutrient for the majority of Americans (Rude et al., 2010a,b; Mason, 2011). In addition, Mg is a beneficial nutrient for bio-P uptake and anaerobic digestion of solids (Speece, 1996).
3. $\text{Mg}(\text{OH})_2$ is much less soluble than NaOH or $\text{Ca}(\text{OH})_2$ so it can be added in excess (intentionally or accidentally) without unnecessary pH spikes. This gradual pH addition also allows for a more robust system, as interruptions in additives have a less immediate effect on system pH (Shand, 2006).
4. Slow dissolution allows excess magnesia to be carried over into other processes, such as nitrification, to supply consistent alkalinity with the fewest number of chemical addition points. Gradual alkalinity addition from $\text{Mg}(\text{OH})_2$ can also maintain a more consistent elevated pH over several hours in collection systems. Elevating the pH shifts the equilibrium of the dissolved sulfides away from the corrosive and malodorous hydrogen sulfide, H_2S , and toward the nonvolatile bisulfide (HS^-), as can be seen in Figure 4.1. Further, if the pH rises above about 8.5, the dissolved H_2S concentrations are reduced to a negligible fraction of total sulfides. Use of $\text{Mg}(\text{OH})_2$ can lead to more effective odor and corrosion control in wastewater collection systems, accompanied by the added benefit of nutritional supplementation of magnesium (Firer et al., 2008; Talaiekhosani et al., 2016; Jensen, 1990; Gutierrez et al., 2009). Any alkalinity supplied in collection systems can also be carried over into treatment processes, which can help maintain a more consistent influent pH and lower total system costs.

This work examines $\text{MgO}/\text{Mg}(\text{OH})_2$ for use in water and wastewater treatment and evaluates the factors that affect the dissolution of magnesia slurries. A nonlinear rate equation is developed, empirically fit to laboratory experiments, and verified by several case studies. Because $\text{MgO}/\text{Mg}(\text{OH})_2$ has only recently gained acceptance for pH/alkalinity control, little research has been conducted on magnesia slurries, and there is a paucity of data and case studies documenting its performance. No previous kinetic dissolution models have been published for mangesia slurry use in water and

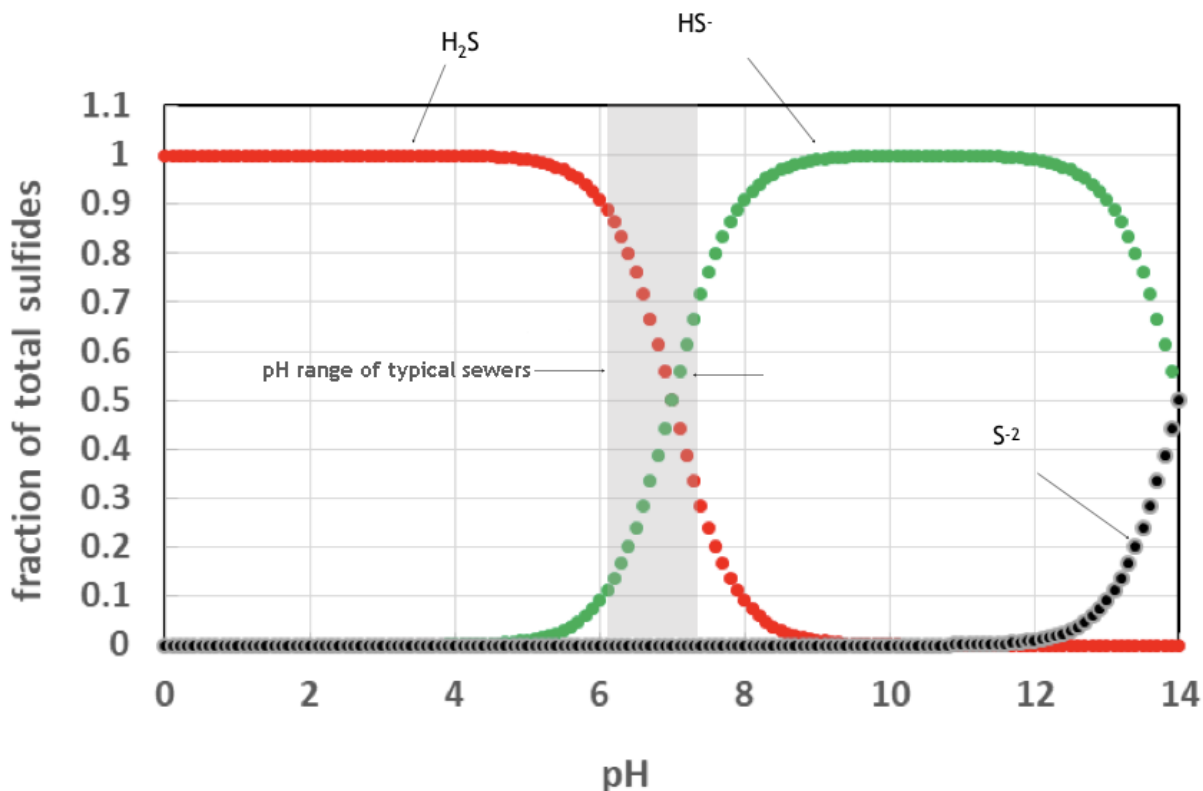


Figure 4.1: Fraction of individual sulfide species versus solution pH. The gray area represents the pH range in typical sewers before magnesia is added.

wastewater treatment. Consequently, published studies in related fields (MgO hydration kinetics, natural weathering of brucite, MgO/Mg(OH)₂ powder dissolution kinetics at low pHs, etc.) were used for insight into the mechanisms of magnesia dissolution. A collection of these related studies are summarized in Table 4.1.

4.1.1 General Magnesia Chemistry

Magnesium hydroxide, Mg(OH)₂, precipitates via a salt metathesis reaction when magnesium ions and hydroxide ions are both present in a solution. In nature, this will commonly occur when ammonium, potassium, or sodium hydroxides combine with magnesium salts through a serpentinization reaction and form the solid mineral brucite. However, industrial grade Mg(OH)₂ is more commonly precipitated by mixing lime with brine or sea water or by hydrating MgO seed

Table 4.1: Published studies relevant to the dissolution kinetics, hydration kinetics, or surface chemistry of $\text{Mg}(\text{OH})_2$ and MgO (in different forms). To date, no kinetic models have been published for commercial-grade $\text{Mg}(\text{OH})_2$ slurry dissolution, and existing kinetic studies for other magnesium products are rarely performed in conditions relevant to water and wastewater treatment.

Article	Material(s)	Application	pH Range	Methods	Rate Limiting Reaction	General Rate Expression	Reaction Order	Relevant Findings
Vermilyea (1969)	MgO , $\text{Mg}(\text{OH})_2$, and natural Brucite powders (10 to 30 μm dia.)	Metal corrosion	3.0 to 10.0 (alloys with initial pH of 3.0)	H, P, M, C, U	Surface reaction between protons and OH^-	Below pH 5.0, the Rate = $k \cdot [\text{H}^+]^{0.47}$. From pH 6.0 to 8.0 the rate is somewhat constant. Above pH 8.0 there is a "decreasing rate".	0.47 (below pH 5.0), 1.0 (above pH 5.0)	Describes the formation of an $\text{Mg}(\text{OH})_2$ shell during dissolution. At pH < 5.0, the dissolution rate is a function of proton concentration. Between pH 5.0 and 9.0, surface activity likely controls. At pH > 9.0, solution magnesium saturation should control the dissolution rate. Magnesia age, temperature, and several inhibitors may greatly influence rates.
Bharadwaja et al. (2013)	$\text{Mg}(\text{OH})_2$ powder (6 μm mean dia.)	CO_2 separation in coal fired power plants	7.6 to 9.6 (held constant)	H, T, P, O, U	Surface chemical reaction	Multiple models developed, but principal rate given as: Rate = $1.30^{(pH-9.52/7)}$ [$\text{Mg}(\text{OH})_2$] $^{0.24}$	0.2 to 0.31	
Birchal et al. (2001)	MgO (45 to 52 μm dia.)	MgO hydration	Unspecified	H, T, P, X, U	Surface chemical reaction dependent on surface area and porosity	N/A	N/A	Developed a kinetic model of MgO hydration (evaluated vs temperature and time, but not pH). Developed a model for porosity vs time. Assumes no diffusive effect.
Rocha et al. (2004)	MgO (1 to 200 μm dia.)	MgO hydration	Unspecified	H, T, P, C, U	Reaction at reprecipitated $\text{Mg}(\text{OH})_2$ surface	N/A	N/A	Explored temperature, density, reaction time, and particle size/surface area dependence of MgO hydration. Suggests that an $\text{Mg}(\text{OH})_2$ shell forms at the particle surface.
Stolzenburg et al. (2015)	Hydrated MgO powder	Promoting struvite precipitation	5.3 to 11.5 (initial pH 5.3)	H, O, B, G	Surface chemical reaction	N/A	N/A	Examining the use of MgO to promote struvite precipitation. No kinetic expressions.
Wieland et al. (1988)	Various oxide and silicate minerals	Weathering of minerals	5.0	None	Detachment of metal ligand complex from the surface lattice.	Generalized the rate using linear free energy relations. Refers to a common rate equation for oxide minerals in low pH solutions of Rate = $k[\text{H}^+]^n$, where n is between 0.2 and 0.5.	0.2 to 0.5 (oxide minerals in general)	Analyzes existing literature for minerals with far lower point of zero charge (pzc) than $\text{Mg}(\text{OH})_2$ (approx. pH 12.5). A generalized mechanistic model is developed for weathering of oxide and silicate minerals. Surface protonation isotherms are derived.
Pokrovsky & Schott (2004)	Precipitated crystalline brucite	Weathering of minerals and pollutant migration	2.5 to 12.2	H, P, S, M, C, U	The proton-promoted dissolution rate should be proportional to the concentration of a protonated surface species	Rate = $k \cdot (\text{Mg}(\text{OH})_2)^2 \cdot (1 - \Omega)^2$, where Ω is a function of the solution magnesium saturation and $>$ denotes a surface species.	2.0 (\pm 0.1)	Dissolution evaluated in solutions close to equilibrium. Suggest there is little dependence on ionic strength within natural systems. Suggests different kinetic rates for systems below pH 5.0 and systems above 5.0, as well as a diminishing rate with magnesium saturation above pH 9.0.
Jordan & Rammensee (1996)	Freshly cleaved, natural, pale green, and optically clear brucite crystals	Weathering of minerals	2.7 and above	H, P, S, X, U	Dissolution reaction is definitively not transport controlled, and likely limited by a surface reaction.	See source material (involves arguments pertaining to imaging setup)		Determined reactions occur at surface and are not transport controlled. At low pHs (2.7) and high dosages, the dissolution hits a maximum rate dependent on temperature.
Fedorockova & Rasmann (2008)	Three periclase samples (63 to 71, 100 to 125, and 315 to 355 μm dia.)	Unspecified	2 to 4	H, T, P, S, C, U, G	Measured values of the reaction order for H^+ ions indicate that the rate is limited by the slow reaction of surface hydroxide with a second proton.	$R = k \cdot a^n$, where a is the activity of H^+ ions on the particle surface	0.24 (\pm 0.36) to 0.41 (\pm 0.10)	It is suggested that when MgO particles are dissolved in dilute acid, the total surface area of the solid does not change significantly during the early stages of dissolution.

LEGEND — **H**: Uses higher magnesia concentrations than are common in water and wastewater treatment; **P**: System evaluated at higher temperatures (or over a broader range of temperatures) than is common in relevant treatment processes; **S**: The particle size distribution or surface morphology of the magnesia used in the associated study is likely highly dissimilar to the commercial-grade magnesia slurries examined in this research; **M**: Saturation constants for the selected magnesia product(s) are highly dissimilar to the $\text{Mg}(\text{OH})_2$ slurries used in this research; **M**: Dissolution was evaluated in the presence of background magnesium in order to simulate natural systems; **O**: The system was open to the air, and CO_2 exchange was likely; **X**: The system's openness was unspecified; **C**: The system was closed, and CO_2 exchange was likely negligible; **U**: The system was unbuffered; **B**: Buffers were not explicitly added, but an open system may have absorbed CO_2 over time; **G**: The system was buffered; **G**: The system contained baffled mixing or a homogeneous mixing gradient.

particles in a pressurized vessel (Kramer, 2007; Shand, 2006). In its simplest form, the precipitation and dissolution of $\text{Mg}(\text{OH})_2$ occurs as follows:



In general, magnesium hydroxide is a sparingly soluble product: 1.0 mM of $\text{Mg}(\text{OH})_2$ usually saturates pure water around a pH of 10.2 (Pourbaix, 1966). Its dehydrated form, $\text{MgO}(\text{s})$, is far more soluble; however, upon introduction to water it quickly hydrates with heat evolution, or (Shand, 2006):



This reaction is highly exothermic; its enthalpy of reaction is approximated as:

$$\Delta H_{298} \approx -9.77 \text{ kcal/mol} \quad (4.5)$$

to produce a crystalline form at stoichiometric water addition at standard state, as reported by Smithson & Bakhshi (1969).

While the low solubility of magnesium hydroxide allows for gradual pH elevation, it also precludes one's use of fast titration curves and simple stoichiometric relationships to model pH, as would be the case for labile NaOH and $\text{Ca}(\text{OH})_2$. For the most common pH states of municipal water and wastewater treatment processes (pH 5.0-8.5), the rate of $\text{Mg}(\text{OH})_2$ particle dissolution is the controlling factor in increasing the pH and alkalinity. A kinetic model, particularly one that can be calibrated to adapt to the variability between treatment plants and processes, is a valuable tool in the development and operation of mangesia-based processes. The low solubility and suspended nature of the slurry both appear to influence dissolution in water with near-neutral or neutral pH. Consequently, a general kinetic model must consider the slurry characteristics (particle size distribution, shape, density, concentration, slurry age, etc.) as well as its thermodynamic relationships (Mg^{2+} saturation, solution buffer capacity, ionic strength). (Amaral et al., 2011;

Thomas et al., 2014; Stoltzenburg et al., 2015; Birchal et al., 2001; Rocha et al., 2004).

4.1.2 Modeling Alkalinity and pH

During the dissolution of $\text{Mg}(\text{OH})_2$ in water, the pH will change based upon the solution alkalinity (typically phosphate and carbonate) and can be modeled using conservation of alkalinity:

$$\text{Alk}_{total} = [\text{HCO}_3^-] + 2[\text{CO}_3^{2-}] + [\text{HPO}_4^{2-}] + 2[\text{PO}_4^{3-}] + [\text{OH}^-] - [\text{H}^+] \quad (4.6)$$

where Alk_{total} is the total solution alkalinity in meq/L and all species are in mM and are a function of pH based on their acidity constants, or:

$$\text{Alk}_{total} = \alpha_1 C_T + 2\alpha_2 C_T + \gamma_2 P_T + 2\gamma_3 P_T + 10^{(14-pH)} - 10^{-pH} \quad (4.7)$$

where α_s and γ_s are the ionization fractions for the carbonate and phosphate systems, respectively. For the carbonate system, the ionization fractions are given by:

$$\alpha_1 = \frac{K_{a1}[\text{H}^+]}{[\text{H}^+]^2 + K_{a1}[\text{H}^+] + K_{a1}K_{a2}} \quad (4.8)$$

and,

$$\alpha_2 = \frac{K_{a2}}{[\text{H}^+]} \alpha_1 \quad (4.9)$$

where $pK_{a1} \approx 6.35$ and $pK_{a2} \approx 10.33$ at an ionic strength of 0.01 mM (Averill & Eldredge, 2012; Smith & Martell, 1996).

For the phosphate system:

$$\gamma_1 = \frac{K_{a1}[\text{H}^+]^2}{[\text{H}^+]^3 + K_{a1}[\text{H}^+]^2 + K_{a1}K_{a2}[\text{H}^+] + K_{a1}K_{a2}K_{a3}} \quad (4.10)$$

$$\gamma_2 = \frac{K_{a2}}{[\text{H}^+]} \gamma_1 \quad (4.11)$$

$$\gamma_3 = \frac{K_{a3}}{[\text{H}^+]} \gamma_2 \quad (4.12)$$

where $pK_{a1} \approx 2.16$, $pK_{a2} \approx 7.21$, and $pK_{a3} \approx 12.32$ at a background ionic strength of 0.01 mM (Smith & Martell, 1996; Averill & Eldredge, 2012). The acid dissociation constants for both systems are reported as approximates because of the large range of published values—a concept described previously in Chapter 2. Future models may be improved by evaluating the impacts of these uncertainties; however, a full-scale Monte Carlo uncertainty model would be overdesigned for use by practicing professionals, so process-specific calibration will be employed in this model instead.

Following Equations 4.6-4.12, the resulting pH after a change in alkalinity can be determined for any solution with a known C_T , P_T , and Alk_{total} using a nonlinear equation solver for $[\text{H}^+] = 10^{-pH}$. In a closed system—i.e. where Alk_{total} , C_T , and P_T are conserved and $\text{Mg}(\text{OH})_2$ dissolution is the only source of additional alkalinity or negative acidity—the alkalinity will change over time as a function of the hydroxide ions introduced to the solution by the slurry.

$$\text{Alk}_{total} = f(\text{time}) = \text{Alk}_{initial} + \text{OH}^-_{added} \quad (4.13)$$

where OH^-_{added} is the total concentration of hydroxide ions added by the dissolving slurry. While there are other potential contributors to alkalinity such as borates or bisulfide, they are usually at low enough concentrations in municipal waste streams to be negligible. Therefore, only carbonates and phosphates are considered in water and wastewater models.

For each magnesium ion that dissolves, two hydroxide ions are produced. Thus, for $\text{Mg}(\text{OH})_2$ dissolution in a closed solution of known initial alkalinity, the OH^- term in Equation 4.13 is equal to twice the magnesium supplied by the dissolved slurry, or

$$\Delta\text{Alk}_{total} = 2\Delta[\text{Mg}^{2+}] \quad (4.14)$$

wherein ΔAlk_{total} is the change in total alkalinity, and $\Delta[\text{Mg}^{2+}]$ is the change in total dissolved magnesium. In cases where biological or other processes are adding or removing alkalinity at the same time as the slurry, Equation 4.14 may not fully represent the alkalinity of the end solution. In such cases, the model will need to be calibrated *in situ* or updated. Note: The expected pH change from a dose of OH^-_{added} will depend on the buffers in solution. The resultant change in solution alkalinity, however, is consistent across buffer states, and will accordingly serve as a central component of this model. In other words, alkalinity is a conservative parameter.

4.1.3 Overview of Magnesia Dissolution Kinetics

For a particle in near-neutral, deionized water, an outer layer of $\text{Mg}(\text{OH})_2$ should dissolve rapidly as long as the solution remains well below magnesium hydroxide saturation. Past studies into MgO hydration/dissolution as well as preliminary $\text{Mg}(\text{OH})_2$ investigations suggest that dissolution kinetics during this “regime” are controlled by particle morphology—specifically, the effective surface area of particles in suspension (Amaral et al., 2011; Thomas et al., 2014; Stoltzenburg et al., 2015; Birchal et al., 2001; Rocha et al., 2004; Seager et al., 2018). $\text{Mg}(\text{OH})_2$, however, is sparingly soluble, so as pH rises it is increasingly limited by solution magnesium saturation. The generalized form of this two-regime concept is illustrated in Figure 4.2 for the dissolution rate of slurries.

For the second regime, where morphology is less influential and magnesium solubility governs (usually above pH 7.5 or 8.0), the dissolved magnesium concentration can be potentially modeled using the general rate equations described in Morel & Hering (1993) and used by Bowers & Higgs (1987) to model iron oxides, or for $\text{Mg}(\text{OH})_2$:

$$\frac{[\text{dMg}]}{\text{dt}} = kA(\text{Mg}^* - \text{Mg})^n \quad (4.15)$$

where Mg^* is the concentration at which the solution is fully saturated by magnesium at the given pH,

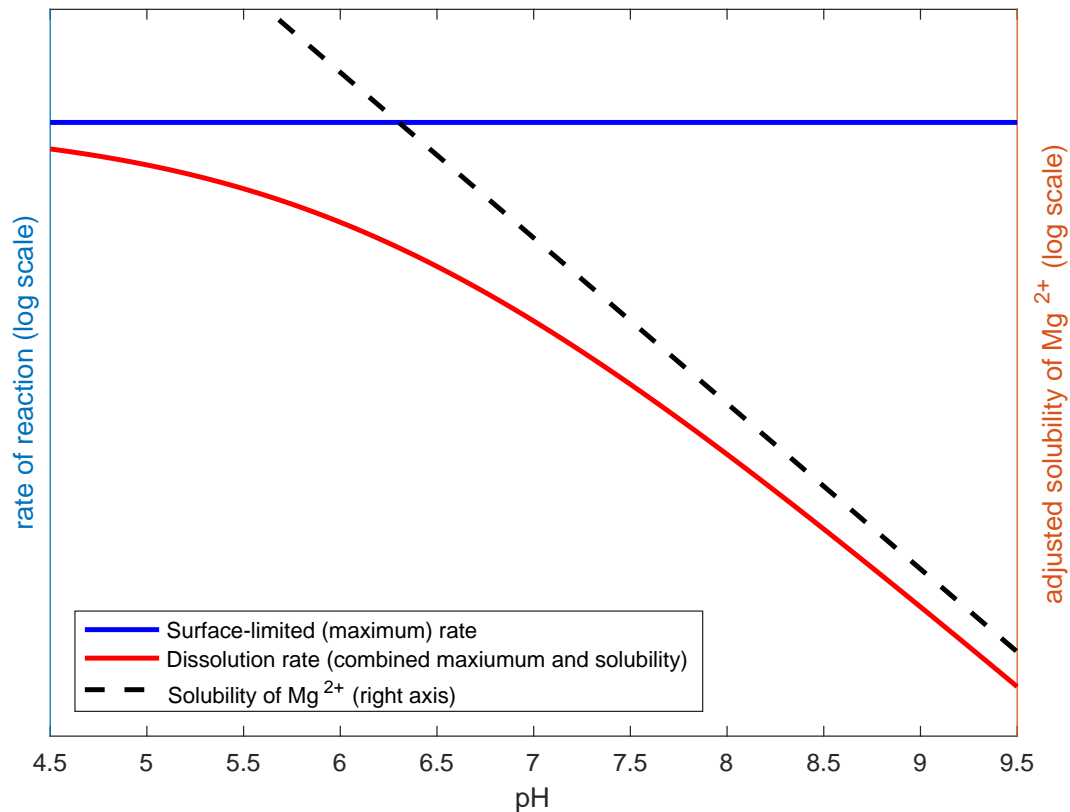


Figure 4.2: A generalized form of the two-regime concept for the dissolution rate of a slurry dose (identical dose across all pHs). The morphology governed rate (Regime I) is not a function of pH, and is thus constant in this context. As this slurry dissolves and the surface area changes, this rate will not remain constant. Magnesium solubility, adjusted by an empirically fit exponential term (generally between 0 and 1), as represented by the dashed line, exerts more control over the initial slurry dissolution rate as the pH increases. In the transition region, usually between a solution pH of about 5.5 and 7.5, both regimes will contribute to the initial dissolution rate.

ionic strength, and temperature (estimated from equilibrium); Mg is the instantaneous magnesium concentration in solution; A is the effective particle surface area; n is a fitted constant representing the order of the reaction (usually assumed to be between 0 and 1); and k is an empirically fitted rate constant used to encapsulate particle size, shape, and surface area effects into a single value. This surface area functionality of solid dissolution kinetics, identified as early as 1931 in [Hixson & Crowell \(1931\)](#), is well studied. General rate expressions have since been developed for non-slurries. These include the Nernst-Brunner equation recently outlined in [Seager et al. \(2018\)](#), or the model

explored by [Bouropoulos & Koutsoukos \(2000\)](#), where

$$\frac{dMg}{dt} \propto \sigma^{\frac{1}{n}} \quad (4.16)$$

and,

$$\sigma = 1 - \Omega \quad (4.17)$$

where Ω represents the saturation ratio, or:

$$\Omega = \frac{[Mg^{2+}][OH^{-}]^2}{*K_{s0}} \quad (4.18)$$

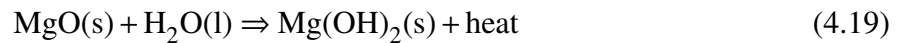
where $*K_{s0}$ is the solubility product for $Mg(OH)_2$ (in terms of $[H^+]$) and n equals 3, the stoichiometric sum for $Mg(OH)_2$.

Due to the wide variety of $Mg(OH)_2$ manufacturing processes, the kinetics of magnesium hydroxide dissolution in pH-controlled environments cannot be simplified beyond Equation 4.15 without particle-specific, empirically fitted coefficients like n and k . Estimations of particle surface area can be performed on tumbled MgO seed particles using nitrogen (or other gas) adsorption methods in accordance with Brunauer–Emmett–Teller (BET) theory. Methods for estimating the surface area of suspended solids—such as the measurement of the negative adsorption of cations ([Van Den Hul & Lyklema, 1967](#))—do exist, but they are still uncommon and have not been demonstrated as reliable. Particle simulation can involve using size distribution data measured by a microsieving system capable of handling liquid samples ([Rocha et al., 2004](#)) or through the use of aqueous polarization intensity differential scattering. While simulated particles are a valuable modeling tool and are employed in this research, surface area data will be drawn from dry particle nitrogen adsorption, as it remains the prevailing and preferred method in the field. Research on periclase samples in [Fedorockova & Raschman \(2008\)](#) suggests that the total surface area of a particle should not change significantly during the early stages of hydration. Moreover, slurry manufacturers usually use BET theory on dry MgO seeds to characterize the surface area of their

suspensions, so following this practice should simplify model calibration across different magnesia products.

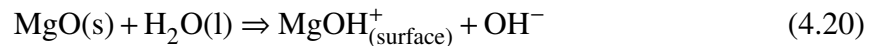
4.1.3.1 MgO Hydration

In the case of a dry MgO powder added to water, particle dissolution should follow the hydration/dissolution process developed by [Stoltzenburg et al. \(2015\)](#); [Shand \(2006\)](#); [Thomas et al. \(2014\)](#); [Rocha et al. \(2004\)](#), and described most simply by

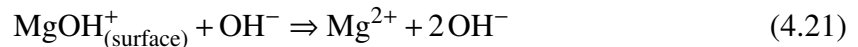


Equation 4.19 can be further broken down into five steps of MgO hydration ([Amaral et al., 2011](#); [Thomas et al., 2014](#); [Stoltzenburg et al., 2015](#); [Birchal et al., 2001](#); [Rocha et al., 2004](#)):

1. Water diffuses into the porous MgO particles, forming intermediate MgOH^+ ions on the particle surface.



2. Solution pH rises rapidly as Mg^{2+} and OH^- ions are released into solution.



3. The aqueous environment directly around the particle becomes supersaturated with Mg(OH)_2 . Magnesium hydroxide subsequently precipitates onto the MgO surface and inside the pores. The pH and concentration of Mg^{2+} ions in solution decrease rapidly during hydroxide formation, following Equation 4.3.
4. A hydroxide shell forms around the free MgO surface, effectively sealing it from further hydroxylation. Conversion of MgO to Mg(OH)_2 slows, and pH becomes steadier.
5. Due to low solubility, the magnesium hydroxide shell dissolves slowly. Any MgO surface revealed is rapidly hydroxylated, leaving Equation 4.15 in terms of Mg(OH)_2 as the presump-

tive controlling kinetic expression until solution saturation is reached or the particles dissolve fully.

See Figure 4.3 for a graphical representation of the dissolution mechanism.

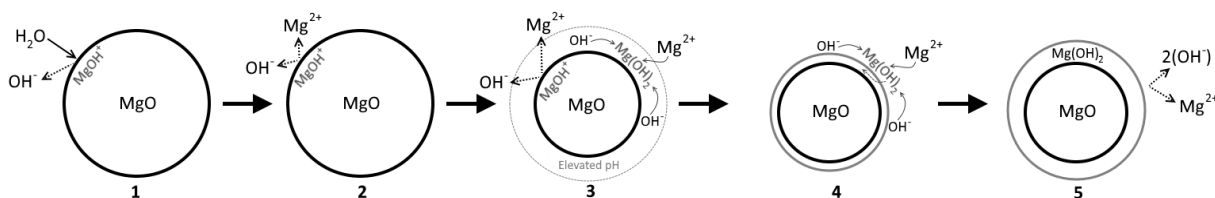


Figure 4.3: Mechanism for MgO hydration described in [Amaral et al. \(2011\)](#); [Thomas et al. \(2014\)](#); [Stoltzenburg et al. \(2015\)](#); [Birchal et al. \(2001\)](#); [Rocha et al. \(2004\)](#).

It seems apparent that $\text{Mg}(\text{OH})_2$ dissolution begins with the third step described in Figure 4.3 and continues the same pattern going forward. However, unlike with MgO hydration, a slurry will have partially (or fully) equilibrated to its suspension in the magnesium saturated supernate. Further, slurries often contain proprietary dispersants/polymers/additives to keep particles in solution. $\text{Mg}(\text{OH})_2$ suspensions often exhibit dissimilar dissolution/hydration rates and pathways, which may result from both of these factors. Nonetheless, MgO hydration provides the most relevant insights available into the underlying dissolution mechanics of magnesia suspensions.

4.2 Experimental Methods

$\text{Mg}(\text{OH})_2$ slurry dissolution must be observed in a controlled environment to model the kinetics of the reaction. More specifically, for both model formulation and slurry-specific calibration, particle dissolution will be measured at 1 atmosphere in a closed (to avoid CO_2 exchange), temperature-controlled environment with a known or measurable pH, alkalinity, mixing speed (or velocity gradient), and magnesium concentration.

Synthetic wastewater solutions were prepared in a Phipps and Bird PB-900 Series programmable jar tester with square, polycarbonate, 2-liter beakers. To limit carbon loss through bicarbonate evolution (and thus inaccurate pH assumptions), the tops of the beakers were cut shorter so to only

hold 2 liters of water and were then retrofitted with plastic covers to close the experiments to the air. A diagram of this experimental setup is included in Figure 4.4.

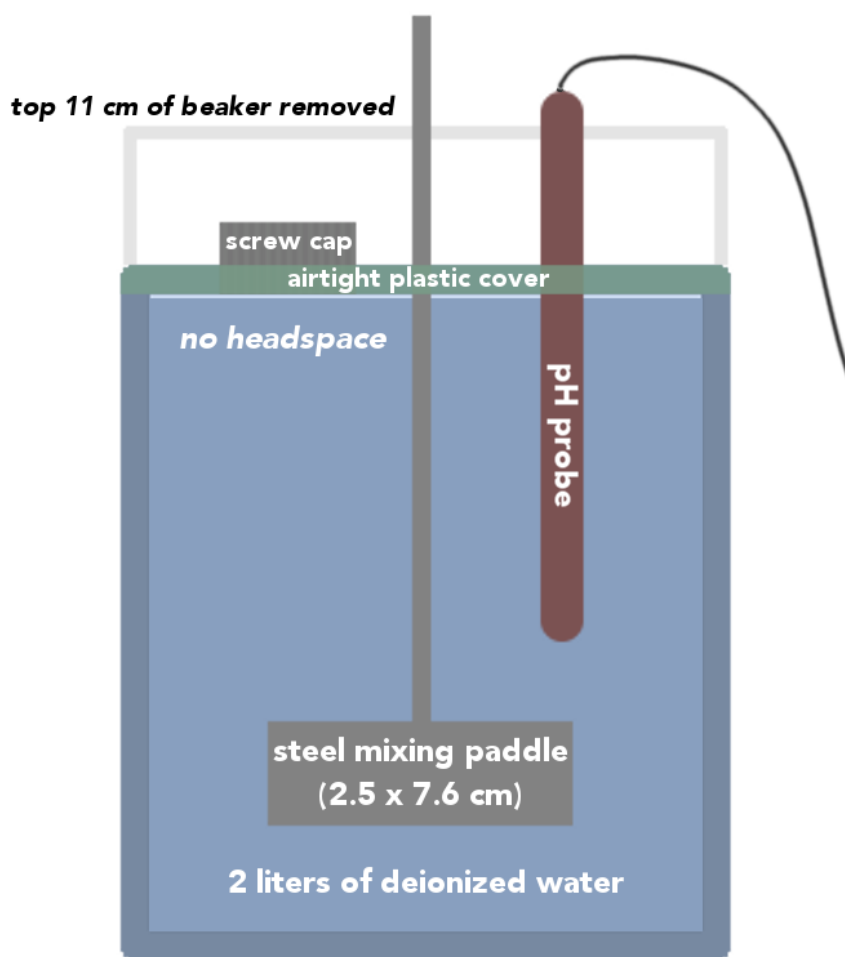


Figure 4.4: Diagram of the modified Phipps and Bird jar test beaker used in the magnesium hydroxide dissolution experiments. The screw cap was opened to add reagents and take samples.

Jar testers are industry standard across American water and wastewater facilities, allowing these experiments to be repeated by utilities using site-specific wastewater compositions—though they too must cover the jars or risk overestimating the pH impact of magnesium slurries. The stirrers in the jar testers are designed to create a fully mixed environment with a consistent, known velocity gradient curve (Lai et al., 1975; Cornwell & Bishop, 1975). In square beakers, this ensures that mixing occurs at known root-mean-squared velocity gradients, G , s^{-1} , as provided by the jar tester

documentation.

Synthetic water/wastewater solutions were prepared in room temperature (approximately 25 °C) deionized water. Before the slurry was introduced, all solutions were prepared by adding 0.1 M sodium chloride to swamp any slurry-supplied ionic strength. Additionally, sodium bicarbonate was added in two different concentrations—0.70 or 1.40 g/L (8.3 or 16.7 mM, respectively). From this, the alkalinity can be calculated at any point using the current solution pH and Equations 4.6-4.12 as long as the total carbon, C_T , is known and there is no phosphate present. While disregarding phosphate alkalinity is a common simplification in water and wastewater treatment due to the prominence of the carbonate system, the model uses a well-supported model of alkalinity (Equation 4.6), and should be readily applicable to solutions with both carbonate and orthophosphate present in significant concentrations.

After the sodium chloride and sodium bicarbonate dissolved, the solution was raised or lowered to a starting pH, pH_0 , using 1 N solutions of NaOH and HCl, respectively. The experiments with synthetic solutions were run at five realistic wastewater pH_0 states (5.5, 6.0, 6.5, 7.0, 7.5) and one relatively extreme state (8.5) to evaluate the upper limits of the model.

As suggested by [Lai et al. \(1975\)](#), the jar tester mixing speed was run at 100 revolutions per minute ($G = 100 \text{ s}^{-1}$) to guarantee turbulence throughout (although the square beakers should ensure it as well). This value was slowed to 50 rpm (44 s^{-1}) for several preliminary experiments, which did not appear to make a significant impact. At even slower speeds, as particles fall out of suspension, the dissolution rate will likely diminish; however, this effect was not studied.

As highlighted by the relationships in Equation 4.15, the chemical potential caused by the difference between a fully saturated solution and the current solution saturation (Mg and Mg^* , respectively) is the driving force behind particle dissolution. To further explore this relationship, some of the calibration experiments were preemptively swamped with dissolved magnesium by adding $MgCl_2$ to the synthetic water before the slurry was introduced. Added at 5.0 mM (approximately 1-3 times the ultimate magnesium dose from the slurry), this information was used to evaluate model performance closer to the solubility limit.

Because manufacturers and preliminary experimentation suggest that the pH response of magnesium hydroxide often changes depending on its age, the slurry samples used in this research were well-mixed before use, frequently replaced, and never used if they were more than one month old. This also means that inconsistencies between slurry batches caused by the manufacturing process were revealed by this experimentation and included in the model. Thus, the results are a good representation of the average $\text{Mg}(\text{OH})_2$ suspension conditions for each sample. Since slurry tanks in treatment facilities are regularly resupplied and perpetually mixed, magnesia used in full-scale processes is usually less affected by the small-scale inconsistencies this lab methodology aims to prevent.

Once the synthetic solutions were prepared, the slurries were added via micropipette in two different concentrations—1.6 or 3.2 mM as Mg—by adding 50 or 100 $\mu\text{L}/\text{L}$ of slurry into each 2-liter beaker. These values were selected as they are representative doses common in wastewater treatment plants. Additionally, since diluting a slurry may invalidate the results by changing initial particle morphology, these were the smallest concentrations that could be added in sufficiently consistent dosages.

For each experiment, the slurry was allowed to dissolve in the closed beaker for 40 minutes. This length was selected because after approximately 45 minutes, low pH blanks (pH < 6.0, no $\text{Mg}(\text{OH})_2$ added) were found to exhibit a measurable rise in pH. This is likely due to CO_2 evolution into the atmosphere due to imperfect seals between the beaker, lid, and pH probe.

Solution pH was measured every minute using a Orion Star A111 benchtop pH meter. The pH probe was inserted through a hole in the beaker cover and sealed to keep the vessel airtight. Filtered and unfiltered samples (1.20 followed by 0.45 μm syringe filters in succession) were taken through an uncapped orifice at the end of the experiment, acidified using 1 N HCl, and evaluated for dissolved magnesium by inductively coupled argon plasma mass spectrometry (ICAP-MS) using a Thermo Scientific iCAP Q ICP-MS in accordance with [Rice et al. \(2012\)](#). These magnesium measurements verified both the concentration of slurry that had dissolved and the concentration that remained in particle form (via the unfiltered samples).

Further magnesium measurements were performed on unfiltered samples of the synthetic water and heavily acidified with HCl (pH < 3.0). This process dissolved all of the particles in solution and gave an accurate measurement of the magnesium added per μL of slurry added. For example, the representative slurry used in this study was found to supply a mean of 0.78 mg Mg per μL of slurry added over five samples. Standard error for these samples was estimated as ± 0.015 mg per μL of slurry (about $\pm 2\%$ error), suggesting slurry can be added in relatively consistent doses.

While magnesium measurements over time could be used to confirm the relationship between dissolved Mg and alkalinity/pH (see Equation 4.14), samples are difficult to filter quickly and the undissolved particles continue to dissolve during the sampling and filtration process. These circumstances led to some uncertainty in measurements of Mg over time. Instead frequent pH measurements were used in conjunction with filtered and unfiltered measurements of the final Mg (when dissolution had slowed sufficiently) to serve as the principal metrics by which the dissolution model was validated.

4.3 Field Experiments

4.3.1 North Carolina Lake Water

In addition to experiments on synthetic wastewater, samples of raw water taken from the influent of a 120 MGD municipal water treatment plant were used to evaluate the efficacy of the model. The water was sourced from Mountain Island Lake, a man-made lake along the Catawba River in North Carolina. The methods previously outlined for synthetic experiments were repeated on 2 liters of this water, except that no reagents were added outside of the magnesium dose and the initial pH was left unchanged. Water alkalinity for all field experiments was measured to a sensitivity of ± 2 ppm using LaMotte colorimetric alkalinity test kits.

The slurry dose is usually added in significantly smaller doses when water has particularly low alkalinity. When slurry was added at dosages less than 50 $\mu\text{L}/\text{L}$ (the lower limit of the micropipette), it was diluted in a liter of deionized water before use to ensure accurate measurements. Specifically, 1.0 mL of the magnesia was added to 1.0 L of deionized water, mixed rapidly while covered to

disperse the slurry, and promptly added to the jar tester at the required concentration.

4.3.2 Chesapeake Collection System

This model was also evaluated in the collection system of a 55 MGD wastewater treatment plant in a metropolitan area on the Chesapeake Bay. As part of a larger experiment to evaluate the effectiveness of $\text{Mg}(\text{OH})_2$ for odor reduction, magnesia slurry was added to the waste stream at a pumping station about 3 miles (pipe distance) from the treatment plant itself. From this point, the waste traveled toward the plant for approximately 4 hours and 40 minutes through a closed pipe with no adjoining tributaries. Samples could be taken at the outflow of the pipe, so it effectively worked as a sealed, plug flow reactor. The measured influent was relatively consistent and devoid of magnesium, and contained an average alkalinity of about 156 mg/L (as CaCO_3) almost exclusively from carbonate. LaMotte colorimetric hardness test kits were also used to measure hardness; samples were diluted 10x or 100x when necessary to meet the concentration limitations of the testing methodology. Despite the inability to sample along the pipe and the inherent limitations of experiments in operating treatment systems, this situation was ideal for evaluating the validity of the dissolution model.

The slurry was pumped into the collection system at a constant, known rate, and the alkalinity and magnesium concentrations were measured at the outflow of the pipe at the treatment plant. When used solely to mitigate odors (by raising pH to suppress H_2S volatilization), the ideal dose of slurry would slowly dissolve over the entire 4 hours and 40 minutes while in the collection system, only to be exhausted moments before it arrived at the plant. As such, the model could be used to select a dose that should keep the pH high and show full dissolution at the end of the pipe.

4.4 Selecting and Characterizing a Representative Slurry

Little research has been conducted on modeling the dissolution of magnesium hydroxide slurries, and comparatively low solubility and slurry-specific considerations prevent the reappropriation of models designed for other common treatment additives. As there are no available models for magnesia dissolution in water and wastewater, this proposed model relies on empirical results to

support several of the constitutive decisions made in its construction. Magnesium hydroxide slurries, however, are highly variable between production methods, manufacturers, slurry brands, and even between ostensibly identical batches. Further, these slurry formulations (particle size distributions, concentrations, additives) are typically proprietary, and manufacturers are generally not forthcoming with this information. Consequently, experiments primarily focused on one slurry—referred to in this research as Slurry A—for which data and samples were provided. This data is not publicly available. Nonetheless, the characterization methods included in this study in combination with the study results should be applicable in modeling new slurries. Four additional suspensions were characterized to provide comparison, but they were not used in any dissolution experiments (Slurries B, C, D, and E).

Slurries A, B, C, and D were all manufactured by hydrating MgO in a pressurized tank. Conversely, Slurry E was manufactured by precipitating functionally homogeneous Mg(OH)₂ from brine. In addition to the five characterized suspensions, size distributions and surface area data for several other magnesia slurries—all derived from hydrated MgO—were used to evaluate the state of the industry. All slurry formulations studied in this research are currently used as additives in U.S. water or wastewater treatment facilities.

Because most scanning electron microscopes (SEMs) available in environmental laboratories are designed for either solid-phase or liquid-phase samples, slurries are often difficult to characterize. The liquid water prevents the use of epoxy to stabilize the slurry for imaging, as is common practice for powders. Moreover, attempts to dry the slurry resulted in substantial morphological changes in the particles. Liquid-phase SEMs have produced slurry images in the past; however, samples may be altered through the use of partial water vapor pressure in the specimen chamber. Further, liquid-phase SEMs generally only image a thin layer at the top surface of a liquid, and frequently achieve poor contrast and resolution (Bogner et al., 2005). However, liquid-phase SEM technology is rapidly improving (De Jonge & Ross, 2011); in recent years, better images of magnesia have begun to appear in journals and manufacturer documentation. In Pradita et al. (2017), the shape of dry MgO particles is shown to be significantly different across manufacturers. They suggest

that this may be a result of both the uncertain effects of calcination during synthesis and particle shrinkage while cooling, among other reasons. Nonetheless, the particles characterized by [Pradita et al. \(2017\)](#) were approximately round, and the seed for Slurry A is tumbled to achieve an even more spherical shape prior to hydration. Some SEM images taken by manufacturers of both their tumbled MgO powder and Mg(OH)₂ slurry support these assessments; however, these images are proprietary and cannot be included in this study.

Because of these constraints, imaging was only used in this research to gain basic insights into particle morphology—namely, that the dry particles were markedly spherical, and there is reason to expect hydrated slurry particles retain this approximate shape during dissolution (as supported by [Fedorockova & Raschman \(2008\)](#)). Instead, slurry was characterized by measuring four non-graphical metrics: surface area of particles per unit mass of slurry, magnesium concentration per unit volume, average slurry density, and average differential volume of particles (i.e., particle diameter vs. percent of the total volume of solids).

4.4.1 Simulation of Slurry Characteristics

Instead of modeling the dissolution of the slurry as a single entity, the proposed model simulates representative particles grouped by particle-size distribution estimates.

When large numbers of unique entities—in this case, particles—are modeled, it is common to represent the attributes of each individual entity as random variables drawn from the distribution of that attribute within the slurry as a whole. For example, if particle radii in a suspension could be described by a normal distribution with mean μ and variance σ^2 , then the initial diameter, $Diam(0)$, of a simulated particle, w , would be taken as

$$Diam_w(0) \sim N(\mu, \sigma^2) \quad (4.22)$$

and if Z is a standard normal random variable,

$$Diam_w(0) = \sigma Z + \mu \quad (4.23)$$

Although Slurry D could be modeled as a truncated normal distribution, the distribution of particle diameters in Slurries A, B, and C did not follow any standard probability distribution. To properly encapsulate these “abnormally” distributed sizes, the simulated particle diameters were instead derived from particle size characterization experiments in the form of empirical distributions, similar to the process described in Chapter 2. As with most particle size characterizations, suspension solids were partitioned into bins with other particles of similar diameter, and the percent volume of each bin was measured. The diameter of every particle within a bin was then modeled as the average diameter within that bin. In the case of Slurry A, there were 59 different bins with diameters ranging from approximately 0.4 to 120 μm . Other slurries exhibited particles as small as 0.05 μm , but none were larger than 120 μm . Since this type of characterization is commonplace in the magnesia industry, the particle size model can be easily updated for any new slurry.

4.4.2 Morphology

Particles were assumed to be spherical as an inspection of several tumbled and hydrated magnesia slurries verifies that is predominantly the case. Proprietary imaging and documentation by magnesia manufacturers further supports the spherical assumption. Though past MgO dissolution studies have taken micrographs showing irregular but stout particles (Rocha et al., 2004; Liu et al., 2012; Amaral et al., 2011), other studies have shown images of longer and more angular particles, which are less ideal for spherical modeling (Thomas et al., 2014). While MgO will likely exhibit morphology dissimilar to particles in precipitated and hydrated slurries, existing literature for dry MgO particles is far more extensive. In a rare example, Wang et al. (2011) showed that $\text{Mg}(\text{OH})_2$ nanoparticle growth morphology is highly dependent on the method of synthesis. Consequently, morphological consistency between slurries used in this research and others should not be assumed.

Additionally, as the reprecipitation of $\text{Mg}(\text{OH})_2$ into the pores and onto the surface of dissolving MgO particles has been found to smooth incongruencies in the solid-liquid interface (Stoltzenburg et al., 2015; Rocha et al., 2004), it is reasonable to expect both layered or pure $\text{Mg}(\text{OH})_2$ particles to exhibit similarly rounded morphologies. Visual inspection of hydrated particles via scanning

electron microscope (SEM) was unsuccessful. Further experimentation involved ingrain the slurry in an epoxy, which supported the assumption of generally round particles; however, the epoxy mixing and hardening process likely caused changes in particle geometry or surface structure, and evolution/devolution of the hydration states outlined in Figure 4.3.

4.4.2.1 Particle Homogeneity

The state of magnesium hydration and dehydration within slurries is relatively complex, as Figure 4.3 highlights. The mass fraction of MgO vs. Mg(OH)₂ is difficult to evaluate by microscopy due to the variety of particle sizes, the similar appearance of the different magnesium states, and preparation difficulties involving slurry/instrument incompatibility. Inherently, ICAP-MS cannot differentiate between hydration states. For particles precipitated from brine as Mg(OH)₂, it is reasonable to assume that the magnesium content is almost exclusively hydrated. For slurries produced by the pressurized hydration of dry MgO, however, it is possible that a core of dry MgO exists within larger particles. As mentioned earlier, the hydration process quickly forms a smooth layer of reprecipitated Mg(OH)₂ on the surface, potentially sealing off the hydration interface behind a less soluble shell (Stoltzenburg et al., 2015; Rocha et al., 2004). This may seem inconsequential, as any MgO revealed in dissolution will rapidly dissolve and reprecipitate; however, the absence of the hydroxyl group on MgO means that its magnesium per unit mass is higher than Mg(OH)₂. Consequently, a fully dissolved non-homogeneous slurry would add more alkalinity per unit mass than a homogeneous one—an important factor in process design, slurry formulation, and plant operations. Accordingly, the Mg(OH)₂/MgO content of hydrated slurries as well as precipitated slurries (though presumed homogeneous) were evaluated using thermogravimetric analysis (TGA).

4.4.2.2 Thermogravimetric Analysis

Thermogravimetric analysis (TGA) was identified as the ideal means to differentiate between the Mg(OH)₂/MgO content. During TGA, a sample is placed on a hyper-sensitive scale within a sealed container and gradually heated at a constant rate to 1000°C. As sample constituents vaporize, sublime, or are removed by some other chemical or physical phenomena, the reduction in mass is

measured as the fraction of total mass lost.

In the case of $\text{Mg}(\text{OH})_2$ particles, the TGA was expected to pinpoint at least two notable reactions. The first occurs around 100°C , when the free water in the slurry is evaporated away (Wang, 2011; Kramer, 2007). This accounts for a large portion of the mass, but reveals little about the nature of the particles.

The second reaction — the dehydration of $\text{Mg}(\text{OH})_2$ into MgO — occurs around 350°C and is expressly more pertinent Kramer (2007). The water lost in this step is entirely bound by the $\text{Mg}(\text{OH})_2$. Using the known 1:1 ratio of water to magnesium oxide in the dissolution of $\text{Mg}(\text{OH})_2$, one can solve for the initial $\text{Mg}(\text{OH})_2$ fraction. More simply, thermogravimetric analysis allows the total mass of the slurry to be broken down into three masses—that of the free water, that of the $\text{Mg}(\text{OH})_2$, and that of the MgO nuclei within each particle.

It is important to note that mass fractions of the slurry are not necessarily equivalent to that of an individual particle, especially if particles in the slurry have a wide particle size distribution or highly variable morphology. It is expected, however, that due to the method of hydration of the MgO seeds in manufacturing, the thickness of the outer $\text{Mg}(\text{OH})_2$ layer should be relatively consistent across particles large enough to maintain an MgO nucleus. In cases where MgO seeds are hydrated in batches under different conditions and then combined into a single slurry, this assumption may need to be reevaluated.

Two separate methods of thermogravimetric analyses were performed on Slurry E (precipitated from brine) and Slurry A (hydrated from MgO seeds). The first such method uses a large volume of slurry, 100 mL, and heats it in an oven at a set of predetermined temperatures. The entire sample is weighed between each heating step to calculate water lost in evaporation and subsequent dehydration, as depicted in Figure 4.5.

The use of a larger sample in this oven method simplifies replication and streamlines microscopy. More importantly, the use of such a large volume should limit incongruencies between the sample and the rest of the slurry that may be present in smaller samples.

In addition to the large-scale TGA, a far more precise measure of lost water-weight was

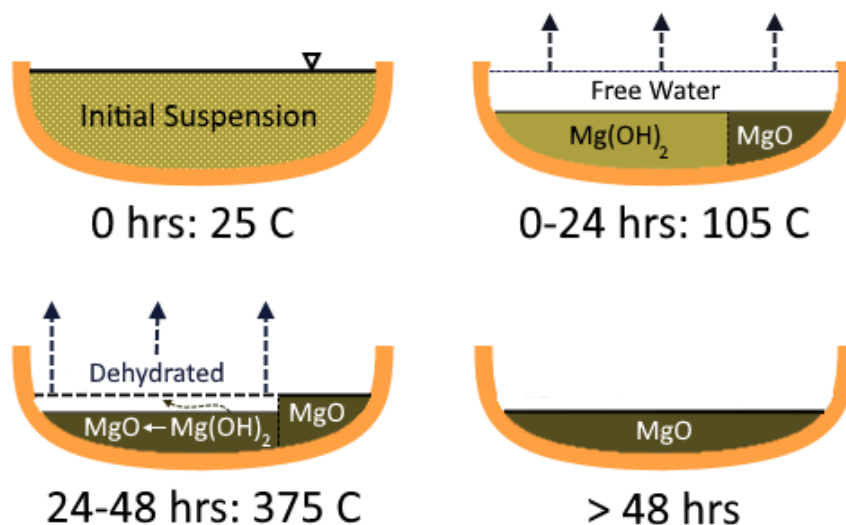


Figure 4.5: Oven analysis of bulk slurry. Temperatures of 105°C and 375°C were selected as they are slightly above the evaporation and dehydration temperatures of 100°C and 350°C , respectively.

performed on a laboratory TGA instrument (TA Instruments SDT Q600). This allowed for far more accurate, real-time measurements of water loss at more refined temperature steps.

The results of the preliminary small-scale TGA analyses on well-aged precipitated (homogeneous) and hydrated (layered) particles are depicted in Figures 4.6 and 4.7. The fraction of dehydrated Mg(OH)_2 was calculated using a 1:1 ratio between moles of water released and resulting moles of MgO , or 1:2.237 by weight. Or, beginning with the water lost to Mg(OH)_2 dehydration:

$$16.5\% (\text{H}_2\text{O from dehydration}) \times 2.237 = 36.9\% (\text{Mg(OH)}_2) \quad (4.24)$$

$$41.7\% (\text{MgO remaining}) - 36.9\% = 4.7\% (\text{MgO core}) \quad (4.25)$$

The remaining weight was considered part of the MgO nucleus. Measurements of soluble metals in the aqueous phase of the slurry (ICAP-MS) have confirmed non-magnesium metals are an inconsequential fraction of the solids.

The end result of the dissolution of one mole of MgO and one mole of Mg(OH)_2 are the same—

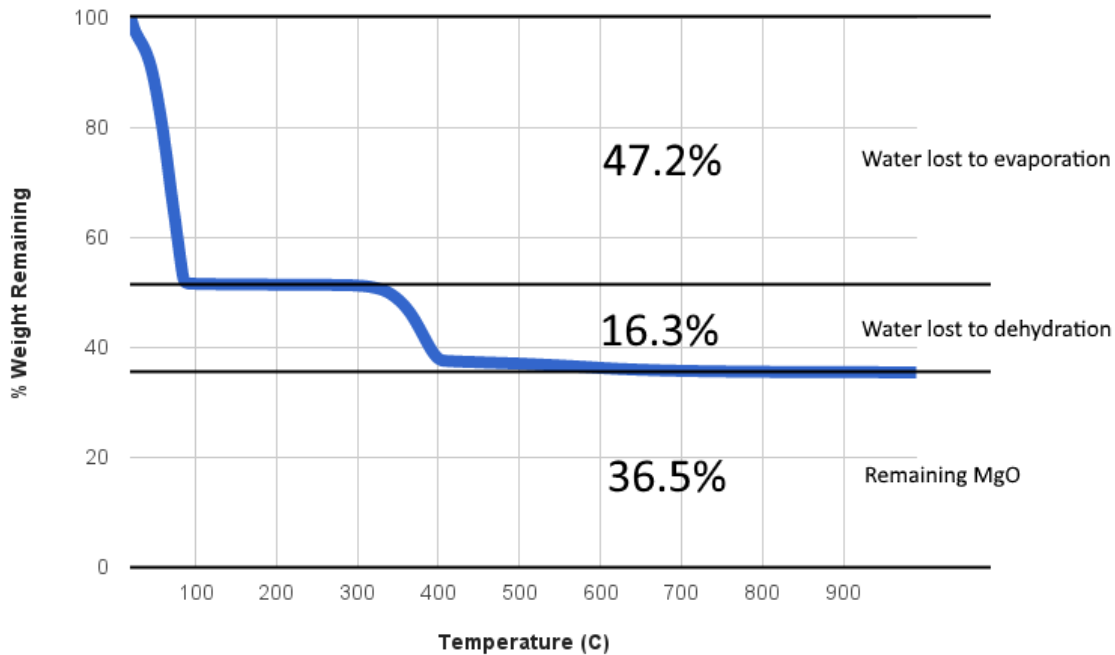


Figure 4.6: Preliminary TGA for precipitated (homogeneous) particles (Slurry E). Note: As expected, the MgO core was found to be negligible when estimated using the method described in Equations 4.24 and 4.25 (in-house data).

the release of two moles OH^- . However, the differences in the molecular weight of the MgO nuclei (40.3 g/mol) compared to $\text{Mg}(\text{OH})_2$ (58.3 g/mol) means that the MgO nuclei are 1.45 times more effective at supplying alkalinity per unit mass.

This “effective density” difference between the two substances is made significantly more important by the manufacturing limitations of the slurry. Manufacturers report that for both precipitated and hydrated particles, more concentrated slurries have difficulties with viscosity and maintaining particle suspension. However, these industry studies—and the manufacturers themselves—consider layered particles as being composed completely of $\text{Mg}(\text{OH})_2$, a fact that TGA experiments contradict.

According to the small-sample TGA, the measured MgO nucleus in Slurry A is around 5 percent of total slurry weight (8 percent of dry particle weight). While physically small, this nucleus should still have a sizable impact on the overall alkalinity added by the dissolution of the slurry.

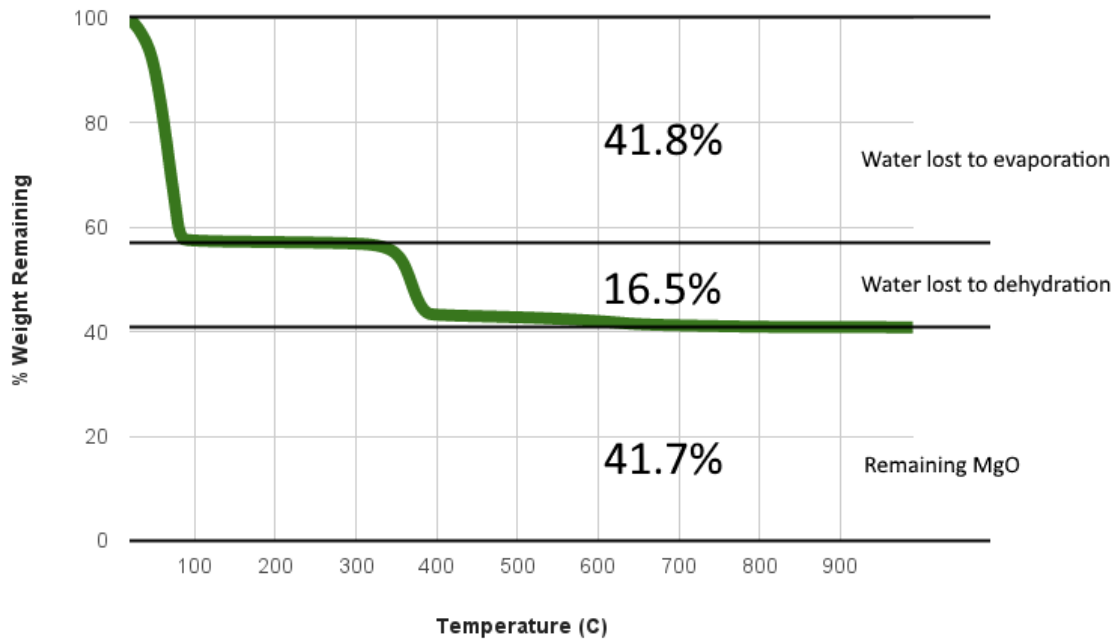


Figure 4.7: Preliminary TGA for hydrated (layered) particles (Slurry A). Note: The fraction of dehydrated $\text{Mg}(\text{OH})_2$ was calculated using a 1:2.237 ratio by weight between water released and resulting MgO , as described in Equations 4.24 and 4.25. The tested solids were hydrated for one year (in-house data).

The simplified large-sample TGA tests confirmed this assessment (around 4 percent of total slurry weight). TGA experiments on Slurry E confirmed that there was no unhydrated MgO present in the precipitated particles, as expected.

When the effective density disparity is considered, an MgO nuclei consisting of 5 percent of total slurry weight gives layered particles (marketed as 58 percent $\text{Mg}(\text{OH})_2$) the per-mass equivalent of approximately 60.3 percent homogeneous $\text{Mg}(\text{OH})_2$ slurry for pH and alkalinity addition. This could potentially highlight a way to push the concentration limits set by viscosity and particle suspension limitations. Lastly, “older” $\text{Mg}(\text{OH})_2$ particles that have been stored in suspension for a long time may exhibit smaller MgO cores as the hydration interface slowly encroaches, thus lowering pH and alkalinity per unit mass.

This research focused primarily on hydrated slurries (Slurry A) and not precipitated slurries

(Slurry E). The particles were modeled as made entirely of $\text{Mg}(\text{OH})_2$ since any exposed (more soluble) MgO would immediately dissolve and reprecipitate as part of the $\text{Mg}(\text{OH})_2$ shell. This simplification could be argued to lead to an underprediction of the magnesium density of a given particle; however, bulk slurry magnesium dosages were calibrated to ICAP-MS measurements and were unaffected by this source of error.

4.4.3 Slurry Aging

One of the primary difficulties in designing a predictive model of magnesia slurries is the variability between slurry samples. Slurry concentrations, additives, particle size distributions, manufacturing methods, and other characteristics vary significantly between manufacturers. This variability gave rise to the decision to design and calibrate this model based solely on Slurry A. Slurry aging, however, is a secondary source of uncertainty that is not mitigated by modeling slurry from only one source.

Magnesia slurries are generally used promptly after they are delivered to a municipal treatment plant—partially because of limited storage space and partially because they must be mixed intermittently to prevent settling (and mixing larger volumes is more expensive). In addition, large quantities of slurry are mixed together, which gives an averaging effect. Slurry aging, therefore, is generally a non-issue in full-scale plants. Unfortunately, the consistency in slurry necessitated by the μL doses used in this research could not necessarily be guaranteed. Different grab samples of the "same" slurry may have aged differently or contain other localized inhomogeneities, or manufacturing conditions/components may have changed slightly. Further, the pH response of aged slurries is different than that of fresh slurry. Although test cases on aged slurries were inconsistent, the release of alkalinity generally appeared to take place more quickly in aged slurries than in fresh ones, and solution magnesium saturation was usually reached more rapidly. This could be attributed to an increase in surface area resulting from fissure development in degrading particle surfaces or other morphological changes. It could also be caused by the formation of magnesium carbonate (at pH 10.5 in the raw product) on the particle surface from exposure to air during storage, however this

was mitigated by limiting air intrusion and headspace in containers (and TGA analysis found no evidence of the presence of magnesium carbonate). To avoid problems with aging, all calibration experiments were performed promptly using the same batch of slurry. Further research is warranted to test this model in full-scale conditions over the range of concentrations, ages, and mixing regimes of magnesia used in actual treatment processes.

In this research, the slurry used in calibration experiments was well mixed before every experiment and always less than one month old. This cutoff was selected since cursory assessments of the aging rate suggested that significant changes in slurry pH response (and final Mg^{2+} concentrations) began to occur after approximately 3 months of storage and intermittent mixing. Nonetheless, this is another potential source of experimental uncertainty if slurries are stored and used over a longer time period.

4.4.4 Particle Shape Evaluation for Example Slurry

For this model, the initial surface area per mole of slurry is derived using N_2 adsorption measurements from the MgO seeds. The rate at which this surface area dissipates, conversely, is predicted using an idealized spherical model. When considering a single particle of MgO undergoing hydration, it may be insufficient to consider surface morphology of a shrinking particle (and thus dissolution rate per unit surface area) as consistent (Stoltzenburg et al., 2015; Smithson & Bakhshi, 1969; Birchal et al., 2001; Rocha et al., 2004). Also, as reported in Rocha et al. (2004), the depth and surface structure of the the initial $\text{Mg}(\text{OH})_2$ shell surrounding fresh particles, created during hydration in pressurized environments, may be significantly different than the reprecipitated $\text{Mg}(\text{OH})_2$ shells that occur at the ambient temperatures and pressures of wastewater treatment processes. Specifically, the formation of fissures are found to be more likely at lower temperatures. These considerations indicate that the surface area and depth of hydration may be influenced by cracks and incongruencies, for which the perfect sphere does not account. In typical wastewater conditions, however, after the initial “fresh” particle surface dissolves and partially reprecipitates as a shell (due to local pH elevation around the particle surface), this sparingly soluble $\text{Mg}(\text{OH})_2$ shell

should remain as the dissolution interface until the particle has completely dissipated (Stoltzenburg et al., 2015; Smithson & Bakhshi, 1969; Birchal et al., 2001; Rocha et al., 2004). Provided the particles don't undergo large pressure or temperature changes during dissolution, this shell should maintain a relatively consistent surface morphology and, subsequently, a consistent dissolution rate per unit surface area over the "lifetime" of the dissolving particle. Specifically, this means that a shrinking spherical model should be viable to model slurry dissolution as long as the $\text{Mg}(\text{OH})_2$ shell serves as a consistent and effective barrier.

The effective surface area per liter, A , is modeled as a function of the idealized surface area, A_{sphere} , and an empirical coefficient, λ , to account for superficial incongruencies, non-spherical aberrations, and the difference between the measured surface area of dry MgO seeds and the surface area of the reprecipitated $\text{Mg}(\text{OH})_2$ shell under current conditions. Or, for a single, spherical particle,

$$A = A_{sphere} \cdot \lambda \quad (4.26)$$

where

$$A_{sphere} = 4\pi r^2 \quad (4.27)$$

and r is the particle radius. The units of A and A_{sphere} are cm^2/L ; however, the entire model is evaluated on a per-liter basis (measurements and outputs in M, meq/L, etc.), so A and A_{sphere} is represented as simple areas (cm^2) to compress derivations.

The spherical model allows geometry can be simplified to:

$$v = \frac{4}{3}\pi r^3 \quad (4.28)$$

where v is the particle volume. Given the assumption of consistent density (ρ), this volume is proportional to the initial concentration of magnesium in each particle.

The remaining particle volume during dissolution can be written as:

$$v(t) = v(0) - \Delta v(t) = \frac{4}{3}\pi(r(0))^3 - \Delta v(t) = \frac{4}{3}\pi r(t)^3 \quad (4.29)$$

where $v(t)$ is the particle volume at time t , $v(0)$ is the initial particle volume, $\Delta v(t)$ is the total volume of the particle that has dissolved by time t , $r(0)$ is the initial particle radius, and $r(t)$ is the particle radius at time t .

These basic geometric assumptions for the preliminary model are outlined in Figure 4.8.

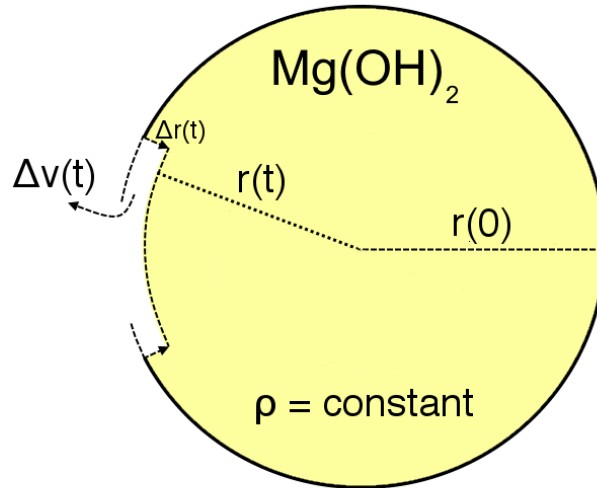


Figure 4.8: Preliminary diagram of particle dissolution. $r(0)$ is the initial radius of the full particle and $r(t)$ is the radius of the particle at time t . The density of each particle is represented by ρ , and is assumed homogeneous between particles and consistent as the particle dissolves. The total volume of the particle that has dissolved by time t is represented by $\Delta v(t)$. The total length of radius lost to dissolution over an elapsed period of time t is represented by $\Delta r(t)$.

Given the assumptions of spherical particles and material homogeneity, the $\text{Mg}(\text{OH})_2$ shells on each particle will dissolve proportionally to the amount of surface area exposed. That is to say, while larger particles will dissolve a larger volume/mass over a period of time, the radius lost over that time period is consistent between particles of all size. Or, for two dissolving particles of differing radii, $r_1(t)$ and $r_2(t)$, at any point in time t :

$$\frac{dr_1}{dt} = \frac{dr_2}{dt} \quad (4.30)$$

This relationship can be derived by starting with the assumption that the rate of dissolution by volume is proportional to the particle surface area, as is suggested by magnesia properties during hydration. This can be written generally as:

$$\frac{dv}{dt} = f(A) = f(A_{sphere} \cdot \lambda) = \Lambda_v(t) \cdot 4\pi r(t)^2 \quad (4.31)$$

where $\Lambda_v(t)$ is a placeholder function representing the volume of particle dissolved per unit surface area, per unit time. More generally, $\Lambda_v(t)$ is a time-dependent representation of λ (to capture evolving surface properties that may change during dissolution). Continuing, Equation 4.28 can be differentiated with respect to t :

$$\frac{dv}{dt} = \frac{d}{dt} \left(\frac{4}{3} \pi r(t)^3 \right) = 4\pi r(t)^2 \frac{dr}{dt} \quad (4.32)$$

This result can be set equal to Equation 4.31, since both are equivalent to $\frac{dv}{dt}$:

$$\Lambda_v(t) \cdot 4\pi r(t)^2 = \frac{dv}{dt} = 4\pi r(t)^2 \frac{dr}{dt} \quad (4.33)$$

Solving for $\frac{dr}{dt}$:

$$\frac{dr}{dt} = \Lambda_v(t) \quad (4.34)$$

This means the rate of radius change across all particles is simply a function of $\Lambda_v(t)$. Because the MgO seeds are all tumbled into spheres before hydration and the reprecipitated $\text{Mg}(\text{OH})_2$ shell described in [Rocha et al. \(2004\)](#), [Thomas et al. \(2014\)](#), and [Amaral et al. \(2011\)](#) should keep the particle surface texture relatively consistent during dissolution, then $\Lambda_v(t)$ should be a function of the material and manufacturing style—both of which are independent of the properties of individual particles. That is to say, the surface area-dependent dissolution rate is simply a function of the

surface properties of this type of dissolving magnesia (which are shared by all particles of the same slurry). If, as expected, this “volumetric flux” is consistent across both time and individual particles, then $\Lambda_v(t)$ can be treated as an empirically fit constant, Λ , that persists for the entirety of dissolution. Equation 4.34 can then be rewritten as:

$$\frac{dr}{dt} = \Lambda \quad (4.35)$$

The morphology-dominated dissolution regime will be modeled as a function of a particle’s simulated surface area divided by the empirically fit Λ constant. In the future, if more accurate measurements of the surface area of dissolving slurries are available, the $\Lambda_v(t)$ function may be characterized and used instead.

If all $\frac{dr}{dt}$ are equal to a constant (Λ), the relationship described in Equation 4.34 simplifies the model significantly. It means that the radii of all well-mixed dissolving particles will shrink at the same rate (though this rate likely changes over time due to solubility) until a particle is fully dissolved. This relationship will allow for a much faster model and a simplified characterization of slurries.

4.4.5 Modeling Surface Area

The particle size distribution of Slurry A was measured using polarization intensity differential scattering (Beckman Coulter LS 13 320 Particle Sizing Analyzer). These results are depicted in Figure 4.9 (as is standard in the industry, the diameters were binned with a logarithmic x-axis so smaller diameter groupings had a finer resolution). Particles within each bin are assumed to be identical, and all share the diameter that falls at the midpoint of the bin.

The specific surface area of tumbled MgO seeds were measured twice by the aqueous nitrogen adsorption method. Using a Tri Star II surface area and porosity instrument, the surface area was estimated to be about $12.6 \text{ m}^2/\text{g}$ and $13.5 \text{ m}^2/\text{g}$. This level of uncertainty is expected, and the values were averaged to find an initial effective surface area of about $13.1 \text{ m}^2/\text{g}$. This is similar to the surface area estimated by the spherical model, $10.3 \text{ m}^2/\text{g}$ (though the model estimate of

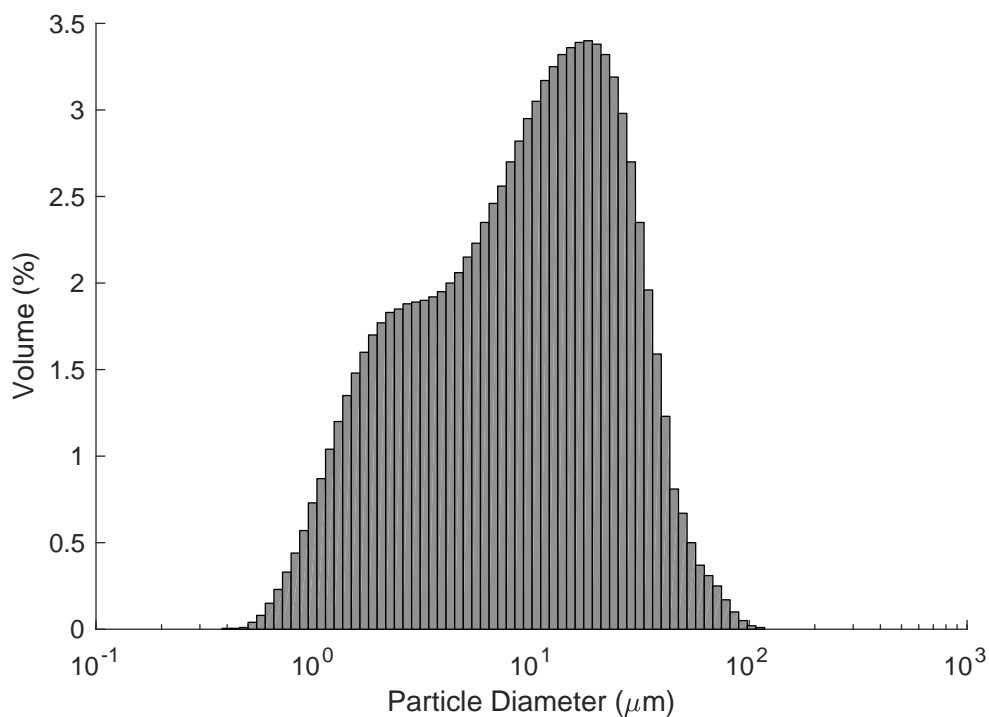


Figure 4.9: Measured percent volume by particle size for Slurry A. Values are binned lognormally.

surface area is not used). Similar to the particle size distributions, this value is expected to be highly slurry-specific, and shouldn't be applied to magnesia slurries other than Slurry A. This value is used to derive the initial surface area for the model.

These surface area estimations are imperfect, as these particles are now in suspension and at least partially hydrated; however, the slurry supernate quickly saturates during manufacturing and the particles should keep their sizes relative to each other. More specifically, at a normal slurry pH of ~10.5 and 25°C, Mg(OH)₂ has a solubility of about 0.0009 g/100 mL while 100 mL of a typical slurry contains between 100-300 g of Mg(OH)₂ (Shand, 2006).

The particles simulated using the particle size distribution are used solely to estimate how the initial surface area will change as the particles dissolve and shrink. Nonetheless, for some of the dissolving solids studied in Seager et al. (2018) (non-slurry pharmaceuticals), particle breakage during dissolution had an influence on the effective surface area. If this is also the case for magnesia slurries, it may cause a disparity between empirical models fit at drastically different dosages and

alkalinities. This might necessitate model recalibration if water properties evolve significantly beyond the scope of calibration.

The surface area at any point in time is derived as a function of undissolved or remaining magnesium, Mg_{rem} , and the initial (measured) surface area. The total magnesium can then be converted to volume of $Mg(OH)_2$ using a molar mass of 58.3 g/mol and a uniform density of 2.34 (as provided by the manufacturer). As each bin is modeled to contain identical particles, only one particle needs to be evaluated per bin—a total of 59 particles for Slurry A. This methodology, and the relationship described in Equation 4.30, allows dissolving particle radii to be modeled by comparing the total volume of remaining particles to the total initial volume of particles (derived from molar dose of magnesium). For example: if, after the first time step, the total volume of particles (per unit volume of solution) has dissolved by a known amount, the 59 representative particles can be simulated to all lose radius at the same rate until the (weighted) sum of the particle volumes equals the modeled volume of $Mg(OH)_2$ remaining. The weight applied to a representative particle volume, which denotes the number of particles in its bin, is derived from the bin's measured volume fraction. To expound, consider a dose of slurry with a total initial volume of $Mg(OH)_2$ particles, $V(0)$. Since all particles in a bin are considered identical, $V(0)$ can be written as the sum of the volume of each representative particle multiplied by the number of particles in its corresponding bin, or:

$$V(0) = \sum_{bin=1}^{59} \left(\frac{4\pi}{3} (r_{bin}(0))^3 \cdot n_{bin} \right) \quad (4.36)$$

where bin is the bin number (1-59), $r_{bin}(0)$ is the initial radius of particles in each respective bin (given by particle size distribution data), and n_{bin} is the initial number of particles in each respective bin. The total volume initially in an individual bin, $V_{bin}(0)$, can be represented simply by:

$$V_{bin}(0) = \frac{4\pi}{3} (r_{bin}(0))^3 \cdot n_{bin} \quad (4.37)$$

By dividing both sides by the total initial volume of particles, $V(0)$, Equation 4.37 can be rewritten

as:

$$\frac{V_{bin}(0)}{V(0)} = \frac{4\pi}{3}(r_{bin}(0))^3 \cdot \frac{n_{bin}}{V(0)} \quad (4.38)$$

The term $\frac{V_{bin}(0)}{V(0)}$ is equivalent to the initial fraction of total $\text{Mg}(\text{OH})_2$ volume supplied by each bin, denoted hereafter as $FV_{bin}(0)$. Equation 4.38 can be rearranged to solve for the n_{bin} of an individual bin:

$$n_{bin} = \frac{FV_{bin}(0) \cdot V(0)}{\frac{4\pi}{3}(r_{bin}(0))^3} \quad (4.39)$$

$FV_{bin}(0)$ and $r_{bin}(0)$ are known quantities for each representative particle, as they are provided by the the particle size analysis measurements (see Figure 4.9). Additionally, $V(0)$ can be computed as the mass of dosed particles divided by the particle density. With this information, n_{bin} can be calculated for each bin. Particles that shrink to a radius of zero during dissolution are still counted in this model, so the number of particles per bin will remain constant.

After an infinitesimal progression of time, the particles will have dissolved slightly, resulting in a new, smaller total volume. After any amount of time t , the total volume of undissolved particles, $V(t)$, is given by:

$$V(t) = V(0) - \Delta V(t) \quad (4.40)$$

where $\Delta V(t)$ is the total volume of $\text{Mg}(\text{OH})_2$ that has dissolved by time t . Because all particles lose radius at the same rate, each representative particle will have the same reduction in radius at time t , denoted as $\Delta r(t)$. Following this, Equation 4.36 can be modified to represent $V(t)$ as a function of $\Delta r(t)$ instead:

$$V(t) = \sum_{bin=1}^{59} \left(\frac{4\pi}{3} (r_{bin}(0) - \Delta r(t))^3 \cdot n_{bin} \right) \quad (4.41)$$

Given a $V(t)$, this equation could already be solved for $\Delta r(t)$. First, however, all sides of Equation

4.41 can be divided by $V(0)$:

$$\frac{V(t)}{V(0)} = \frac{\sum_{bin=1}^{59} \left(\frac{4\pi}{3} (r_{bin}(0) - \Delta r(t))^3 \cdot n_{bin} \right)}{V(0)} \quad (4.42)$$

The term $\frac{V(t)}{V(0)}$ is equivalent to $FV(t)$, the fraction of the initial volume of $Mg(OH)_2$ still undissolved at time t .

Since we assume a uniform density, the volume of undissolved particles is proportional (via density) to the mass of the undissolved particles. This also means that the volume fraction remaining, $FV(t)$, can be considered equal to the mass fraction remaining, denoted as $FM(t)$.

Following Equation 4.39, n_{bin} can be rewritten in terms of measured values $FV_{bin}(0)$, $V(0)$, and $r_{bin}(0)$. Combining this with Equation 4.42, dosed $Mg(OH)_2$ particles that have dissolved to a fraction, $FM(t)$, of their original mass can be represented by:

$$FM(t) = FV(t) = \sum_{bin=1}^{59} \left((r_{bin}(0) - \Delta r(t))^3 \cdot \frac{FV_{bin}(0)}{r_{bin}(0)^3} \right) \quad (4.43)$$

The value of $\Delta r(t)$ can then be solved numerically using any $FM(t)$ and employed to calculate the associated $r(t)$ value ($r(t) = r(0) - \Delta r(t)$). Plugging the calculated $r(t)$ and the measured r_0 into the equation for the surface area of spheres (Equation 4.27), the ratio of the total current to the total initial surface area ($\sum A(t) : \sum A(0)$) can be calculated at any molar fraction $FM(t)$. This value will be referred to as $A_{frac}(t)$.

The numerical process for dissolving particles can be performed for small increments of $FM(t)$ until the slurry is completely dissolved. As the volume in a bin is exhausted, the radii of the constituent particles go to zero, and are thus ignored.

A generic dataset was generated for Slurry A consisting of the molar fraction of magnesium still undissolved, $FM(t)$, and the associated $A_{frac}(t)$ value calculated by Equation 4.43. When modeling any amount of Slurry A, the $FM(t)$ column can quickly be multiplied by the concentration of magnesium added (measured via ICAP-MS), and the $A_{frac}(t)$ column can be multiplied by the initial surface area measured via nitrogen adsorption (not as estimated by the spherical model) to

estimate the actual values of each variable. This dataset for Slurry A is summarized in Figure 4.10.

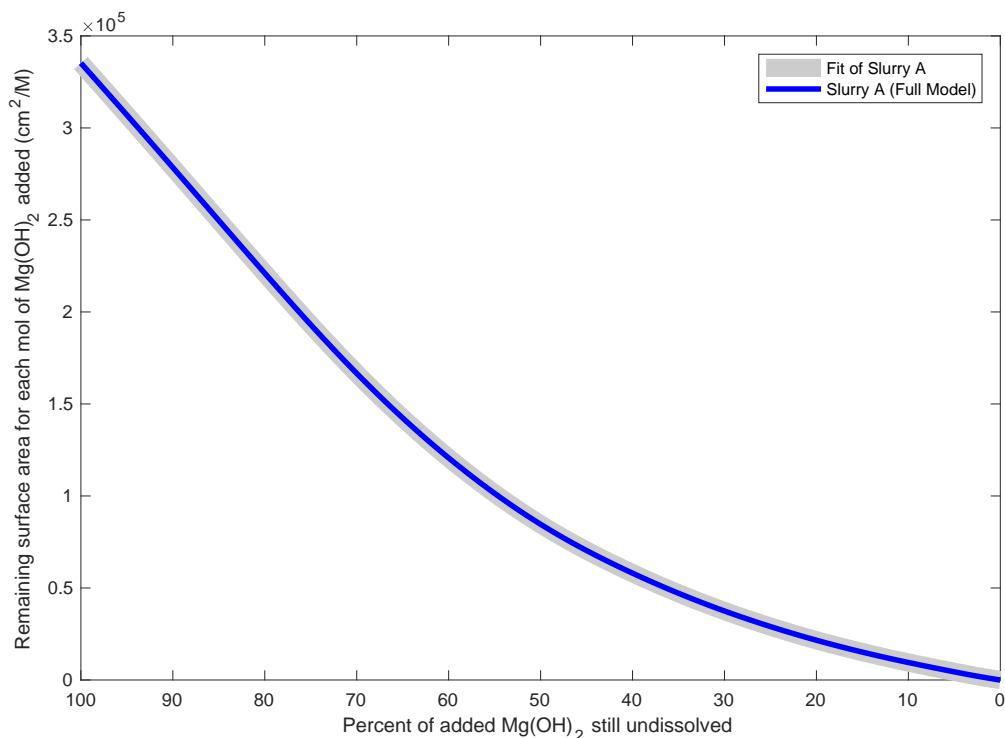


Figure 4.10: Estimated surface area vs. the fraction of Slurry A that remains undissolved (normalized to 1 mol $\text{Mg}(\text{OH})_2$ added.) A fifth-degree polynomial was fit to the data to aid computational speed in modeling, shown as the gray line. Because the plots of the fitted and model data are nearly superimposed, the fitted line has been made bolder so it is visible. Note: The polynomial fit is simply an empirical method by which this slurry-specific data may be efficiently defined for use in the model; it is not an expansion of the underlying shrinking particle theory.

This relationship between molar fraction undissolved and surface area was fit to a fifth-degree polynomial, or:

$$A_{frac}(t) = 91.8 + (-0.724FM(t)^5 + 1.34FM(t)^4 - 0.608FM(t)^3 + 0.253FM(t)^2 + 0.073FM(t)) \times 10^6 \quad (4.44)$$

where $FM(t)$ is the molar fraction of Slurry A that is still undissolved at time t . The fifth-order polynomial fit was selected because it fit the surface area model well; the fraction of variance unexplained was less than 8×10^{-6} . The success of this fit is exhibited in Figure 4.10 by the consistent superposition of the fitted and model data points.

This morphological characterization was performed on three other commercial suspension as well (Slurries B, C, and D); the results are compiled into Table 4.2 and displayed in Figure 4.11. These polynomials can be an efficient means of conveying particle diameter and surface area information for individual slurries. If the particle size distribution and surface area of an untested slurry are similar to those of one of the four representative slurries, the polynomial of the similar slurry may potentially be employed in lieu of a comprehensive analysis the new slurry.

Table 4.2: Fitted parameters for the fifth-order polynomial fit of the particle surface area analysis for four different magnesia slurries. All four equations follow the format: $A_{frac}(t) = p_1 \cdot FM(t)^5 + p_2 \cdot FM(t)^4 + p_3 \cdot FM(t)^3 + p_4 \cdot FM(t)^2 + p_5 \cdot FM(t) + p_6$. This fit was selected because it was the smallest order polynomial that sufficiently fit the data (especially at the boundary conditions). These fits are not an expansion of theory; rather, they are an efficient means of communicating slurry morphology information for use in future predictions.

Slurry Label	Fitted Parameters					
	p_1	p_2	p_3	p_4	p_5	p_6
A	-7.24E-05	0.0134	-0.608	25.3	728	91.8
B	1.57E-04	-0.0383	3.46	-91.7	3440	-1770
C	-3.41E-05	0.00472	-0.00566	9.23	840	-50.6
D	4.75E-05	-0.0136	1.12	0.262	2470	-364

The numerical model described in this study uses Equation 4.44 to estimate total surface area per liter of solution during dissolution by multiplying by the total concentration of slurry added, or:

$$A_{est}(t) = Mg_a \cdot A_{frac}(t) \quad (4.45)$$

where Mg_a is the amount of slurry added (in M) and $A_{est}(t)$ is the estimate of remaining surface area at time t . The coefficient λ from Equation 4.26 is included in this estimate, as it is derived from measured, not simulated, particle data. The Λ coefficient described in Equation 4.35, conversely, is included in the final comprehensive model as part of an empirically fit rate constant.

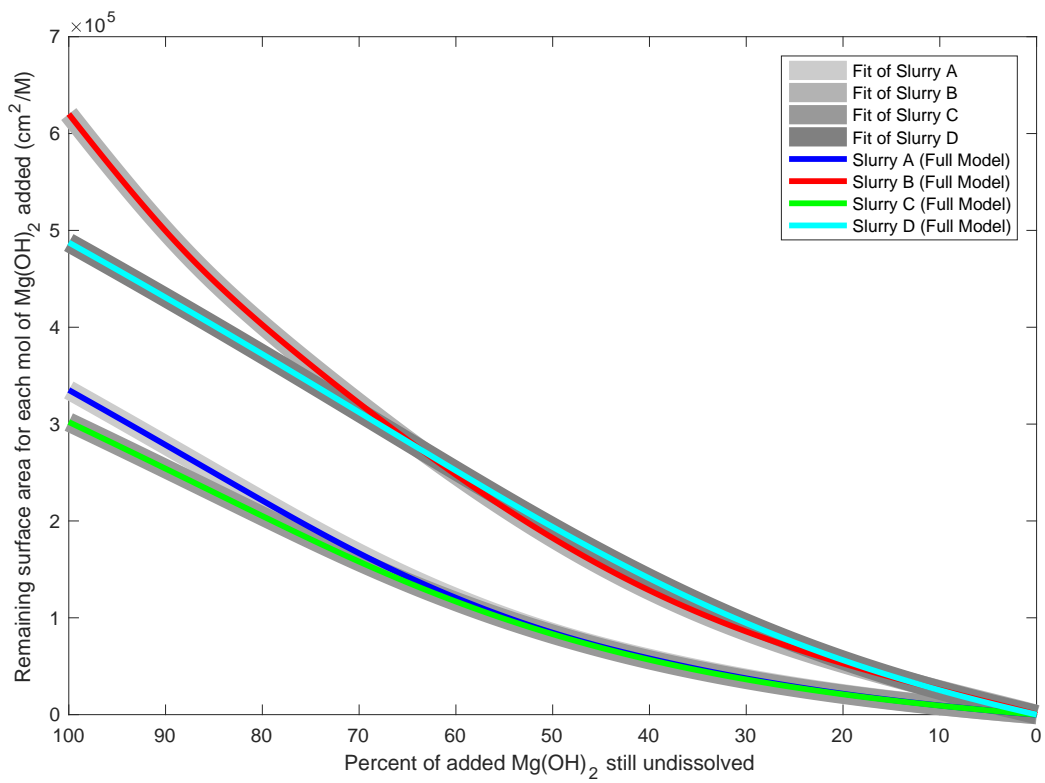


Figure 4.11: The fifth-order fitted polynomials for the characterization of the shrinking surface area of four different magnesia slurries alongside their underlying long-form model predictions. Again, less than about 0.001% of the variance of each remains unexplained, and the fits are near perfect. Because the plotted lines of the fitted and model data are nearly superimposed, the fitted lines have been made bolder so they are visible. Note: the polynomials are simply an empirical method by which to efficiently communicate this slurry-specific data; they are not an expansion of the underlying shrinking particle theory.

4.5 Formulation of Kinetic Model

4.5.1 Conceptual Form

Once surface area is modeled as a function of undissolved magnesium, $Mg_{rem}(t)$, it can be incorporated into the dissolution model. Despite the separation of dissolution kinetics into “regimes”, i.e., those that are surface area-limited and those that are thermodynamically limited, dissolution kinetics should not be thought of (or regarded) as a stepwise process. While surface area may not be the dominant factor controlling dissolution in near-saturated or high-pH solutions, [Seager et al. \(2018\)](#) and [Birchal et al. \(2001\)](#) suggest morphology and resulting particle diffusivity estimates should have an impact on the model across the pH range of standard water and wastewater treatment processes.

As a result, the two regimes must be modeled multiplicatively, and in such a way that the dissolution rate diminishes asymptotically, slowing as the solution approaches saturation. For example, if slurry is added to a solution at a high pH (> 8.5) that is already closer to saturation, the thermodynamic regime should significantly dampen the dissolution rate from the outset. Conversely, if slurry is added to an unsaturated solution at a low pH (< 7.0), the particles will often completely dissolve before magnesium saturation has any influence on the dissolution rate (unless heavily dosed).

Placeholder variables are used to represent the two modulating regimes to create a generic model format:

$$\frac{dMg}{dt} \propto \phi \cdot \psi \quad (4.46)$$

where ϕ represents the morphology-dominated fast regime, and ψ denotes the saturation-dominated slow regime.

At their most basic, the ϕ and ψ terms must accomplish two things: first, they both must accurately represent the asymptotic behavior of their respective systems—for ϕ , this means accurately predicting the extent and effect of diminishing particle surface areas; for ψ , this means accurately

modeling the effect of dissolved magnesium concentrations on solution thermodynamics as the system approaches saturation. In addition, they must permit the seamless transition between the two regimes. If a slurry has completely dissolved (and there is no remaining surface area), there can be no further dissolution of particles regardless of the solution saturation. Similarly, if a solution is fully saturated with magnesium, the particles will not dissolve, despite their surface area. Consequently, these functions must both have a minimum value of zero to allow either term to negate the dissolution rate when their limitations (slurry exhausted/fully saturated solution) are reached. Additionally, ψ and ϕ should range between a value of 1.0 and 0 so a non-consequential term can simply equal 1.0 when its respective regime does not dominate.

The dissolution model developed for iron oxides by [Bowers & Higgs \(1987\)](#) and [Morel & Hering \(1993\)](#), given by Equation 4.15, provides the basis for the model of the saturation-limited regime. Specifically, it suggests a ψ term of the form:

$$\psi \propto (Mg^*(t) - Mg(t))^m \quad (4.47)$$

where $Mg^*(t)$ is the magnesium concentration at saturation/equilibrium, evaluated at the pH at time t ; $Mg(t)$ is the instantaneous dissolved magnesium concentration; and m is an unknown dimensionless reaction order ($m = 0$ to 1.0).

The rest of the model from [Bowers & Higgs \(1987\)](#) and [Morel & Hering \(1993\)](#) includes surface area as a single variable, A , modified only by an empirical constant, k . This simple model could potentially be expanded by replacing the A term with a more complex surface area function; however, Equation 4.15 shapes the model's asymptotic behavior using a single empirical constant, and preliminary experiments showed this method to fit poorly. In solutions of lower initial pH (pH 5.0-7.0), the $Mg(OH)_2$ particles may completely disappear at a point well below the magnesium saturation limit, limiting the impact of the slow regime. Despite this, the ψ component in Equation 4.47 is at its largest magnitude in unsaturated solutions. Similarly, when slurry is added to a solution at higher pH (pH 7.0-9.0), magnesium approaches saturation before the particles fully dissolve. In this case, the area term would continue to significantly impact the rate predictions when it should

be controlled by the diminishing ϕ term. To fix this problem, ϕ and ψ were given their own fitted parameters— α and β , respectively—to individually model and calibrate each regime’s asymptotic behavior.

4.5.2 Thermodynamics

Preliminary experiments suggested that for dissolving particles in solutions nearing saturation, represented by ψ , the dissolution rate was well represented as proportional to:

$$\psi \propto \frac{(Mg^*(t) - Mg(t))^m}{1 + b(Mg^*(t) - Mg(t))^m} \quad (4.48)$$

where b is an empirical constant of units M^{-m} that is used to shape asymptotic behavior, and (t) denotes that a variable is a function of time. The value of ψ ranges from 1.0, when Mg is far from saturation and the fast regime (ϕ) still dominates, to 0 when the solution is effectively saturated. This function was developed by incorporating Equation 4.15 into the classic Langmuir-Hinshelwood (LH) kinetic functions for surface reactions occurring at liquid solid interfaces (often used to model photocatalyzed or enzymatic reaction kinetics) (Ollis, 2018). Langmuir-Hinshelwood equations were investigated for this study as they are often used when modeling surface-area functionality in slow reactions, adsorption kinetics in liquid-solid systems with unknown reaction orders, and kinetic systems limited by multiple or complex reactions. While other continuous functions involving particle surface-area functionality were evaluated, this combination of the LH framework and Equation 4.15 was the best fit to preliminary data. The model is evaluated on a per-liter basis, which allows magnesium concentrations to instead be represented as a mass of magnesium. This simplifies the units and improves readability of the model.

The total saturation concentration of magnesium at equilibrium, $Mg^*(t)$, can be evaluated as a function of pH by (Pourbaix, 1966):

$$Mg^*(t) = 10^{(*pK_{s0} - 2pH(t))} \quad (4.49)$$

where $^*pK_{s0}$ is the negative log of the solubility product for magnesium hydroxide (in terms of $[H^+]$), given as 16.95 by Pourbaix (1966) at 25°C. The value of this empirical constant varies greatly between literature sources; however, 16.95 was found to fit best with in-house data. Specifically, when the $^*pK_{s0}$ estimate was evaluated against laboratory-derived saturation curves rather than simply being assigned a value, the best-fit $^*pK_{s0}$ was found to be ~ 17.0 (at 25°C).

4.5.3 Morphology

The morphology-limited fast regime (surface reaction limited) was best modeled using an exponential asymptote, or:

$$\phi \propto 1 - e^{-A(t)/\alpha} \quad (4.50)$$

where α is an empirical constant that shapes surface area-specific functionality and is equivalent to Λ^{-1} . Since $A(t)$ is in units of area/volume (though dissolution will be assessed at a representative volume of 1.0 liters), and Λ has units of volume/area (because it models the volume lost per surface area over a time step), then the exponent in ϕ will be unitless. The value for $A(t)$ can be estimated from Equation 4.4.5 using an A_{frac} generated from the full model outlined in Equation 4.43 or from the simplified polynomial fit given for Slurry A by Equation 4.44. The differences between the two methods were found to be negligible; however, the latter does not require slurry morphology to be recharacterized continuously.

Before the full kinetic model was run, an $A_{est}(t)$ vs. $Mg_{rem}(t)$ matrix was compiled using the polynomial fit for Slurry A in Table 4.2 across 100,000 decreasing values of $Mg_{rem}(t)$ (see Equations 4.55 and 4.4.5). This matrix could then be referenced to find an approximation of the $A(t)$ term at any point in time, given the current $FM(t)$ and a surface area measurement of the initial slurry dose. As the model's system of differential equations is solved through the use of a numerical method, remaining surface area at time t can be estimated quickly without any additional information from previous dissolution states. This allows for a system that better lends itself to fast numerical solutions.

Equation 4.50 returns a value between 1.0 and 0, which decreases asymptotically as particles dissolve. The initial rate for the magnesium dissolution is assumed to be the fastest morphology-dominated rate, and this function simply dampens this max rate as surface area is depleted.

Equations 4.15 and 4.46 were combined and expanded to produce an overall rate equation for magnesium dissolution:

$$\left(\frac{dMg(t)}{dt}\right)_{\text{preliminary}} = k \cdot \left(1 - e^{-A(t)/\alpha}\right) \cdot \left(\frac{(Mg^*(t) - Mg(t))^m}{1 + b(Mg^*(t) - Mg(t))^m}\right) \quad (4.51)$$

where k is an empirical rate constant ($M^{1-m}\text{sec}^{-1}$). Because ϕ is unitless, the units of k were derived so as to balance the units of ψ . Because the units of k are a function of m , this results in a model that is inconveniently collinear. To remedy this, Equation 4.51 was reformulated by dividing the numerator and denominator of the right-hand side by b . This is achieved by introducing a pair of placeholder variables, κ and β , or:

$$\kappa = \frac{k}{b} \quad (4.52)$$

$$\beta = \frac{1}{b} \quad (4.53)$$

where β is an empirical constant with units of M^m and κ is an empirical reaction rate constant with units of $M \cdot \text{sec}^{-1}$.

Combining these placeholder variables with Equation 4.51, the final form of the kinetic model can be written as:

$$\frac{dMg(t)}{dt} = \kappa \cdot \left(1 - e^{-A(t)/\alpha}\right) \cdot \left(\frac{(Mg^*(t) - Mg(t))^m}{\beta + (Mg^*(t) - Mg(t))^m}\right) \quad (4.54)$$

Following Equation 4.14, the change in dissolved magnesium over a time step, ΔMg , is then converted into change in total alkalinity, $\Delta \text{Alk}_{\text{total}}$. This value is employed in a rearranged Equation 4.7 to solve for the new pH since, unlike alkalinity, the pH response to magnesia dissolution is

nontrivial due to buffers in solution. Then, C_T (and P_T) are constant and $Alk_{total}(t) = Alk_{total}(t - 1) \cdot \Delta Alk_{total}$, or pH is adjusted until Equation 4.7 matches the $Alk_{total}(t)$ at any time. Next, the $A(t)$ term must be updated for the shrinking particles. This requires an updated value for undissolved magnesium, $Mg_{rem}(t)$, given as:

$$Mg_{rem}(t) = \max \begin{cases} Mg_a + Mg_0 - Mg(t) \\ 0 \end{cases} \quad (4.55)$$

where Mg_a is the total magnesium initially added via slurry, Mg_0 is the background dissolved magnesium present in solution before the slurry was added, and $Mg(t)$ is the current dissolved magnesium in solution (modeled). Background magnesium is often near zero in water and wastewater treatment processes. Because of this, and the fact that solution pH will generally have a much more pronounced effect on Equation 4.48 than $Mg(t)$ (as the saturation limit diminishes faster than dissolved magnesium increases), the Mg_0 term will likely be inconsequential in most treatment processes.

Over one time step, the new pH can then be used in Equation 4.54 (via Equation 4.49), and the cycle can start over until saturation is reached or the undissolved slurry is exhausted.

The system of first-order ordinary differential equations given by Equations 4.14 and 4.54 were solved numerically using MATLAB's ode15s multistep solver (Shampine & Reichelt, 1997). The ode15s solver is a variable-step, variable-order (VSVO) solver, and thus does not use a fixed time step. The model returns a vector of first derivatives, $[dMg/dt, dAlk/dt]$, which represents the current system state at any requested point in time. A conceptual outline of this model structure is depicted in Figure 4.12.

4.5.4 Calibration of the Rate Constant

Preliminary experiments suggested the rate of change in dissolved [Mg] in the first three minutes of slurry dissolution was correlated with the initial pH of the solution, except in cases where pH < 6.0 and the available particles dissipated before thermodynamics could impact the rate. However,

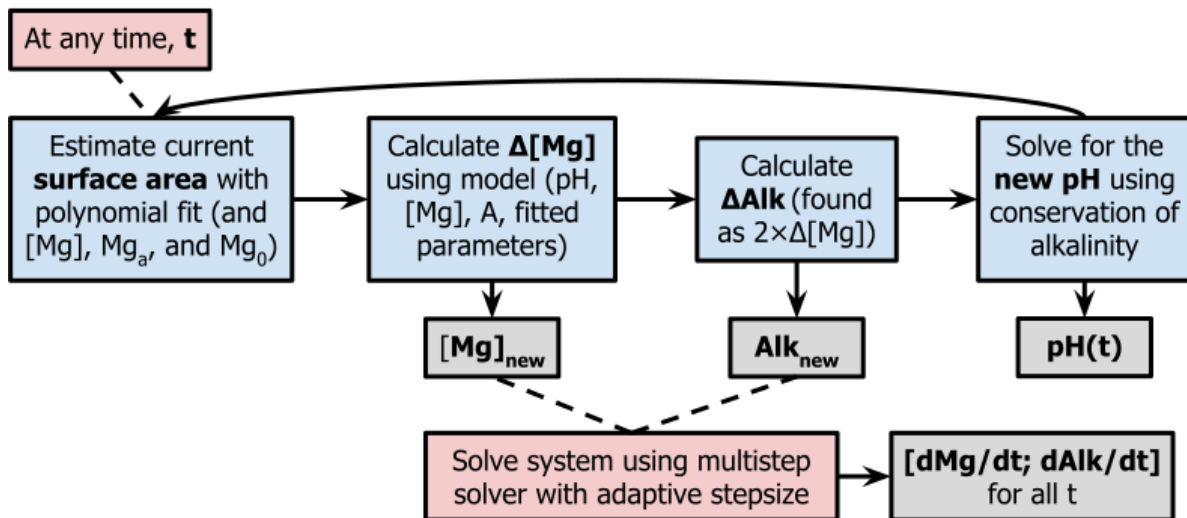


Figure 4.12: A conceptual outline of the dissolution model's computations. In summary, the MATLAB ode15s multistep (VSVO) solver is used to solve the system of first-order differential equations and calculate dissolved magnesium and total alkalinity after each variable time step.

measuring the initial rate of magnesium dissolution is difficult because the rate begins to slow within seconds of particle introduction.

As the ϕ factor already modifies the rate as a function of surface area, κ can be empirically fit over a series of calibration experiments. While κ could potentially be isolated by measuring the initial rate of magnesium dissolution, these methods proved difficult because of localized rate dynamics that take place before the slurry fully disperses as well as the response lag of the pH measurements (about 1 minute). Instead, κ was fit to the full breadth of the dissolution data. Calibration could also be useful to shape the model to process- or plant-specific requirements; however, in cases where $\text{Mg}(\text{OH})_2$ is added in abnormally high doses (>100 mg/L as Mg), the model fit may need to be reassessed.

4.5.5 Effects of Temperature

The influence of solution temperature on $\text{Mg}(\text{OH})_2$ dissolution kinetics has not been extensively studied under water and wastewater plant conditions; however, when analyzing the use of $\text{Mg}(\text{OH})_2$ for CO_2 separation from coal-fired power plants, [Bharadwaja et al. \(2013\)](#) found that the dissolution

rate was temperature dependent when dominated by the thermodynamic regime (ψ). Specifically, over the range of 22 to 32°C, the saturation-dominated dissolution rate was found to increase by a factor of about 2.0. In contrast to those performed for this study, however, these experiments were run at extremely fast mixing speeds (500-1100 rpm), in an open system, at four fixed pHs (pH 7.5-9.0). Although their final dissolution model was found effective for the conditions common within coal-fired power plant CO₂ separation processes, it focused on elevated pH systems that exhibit less variability than is expected in wastewater. This specificity allowed their model to focus primarily on the saturation-dominated (solubility limited) dissolution regime without the extensive surface area modeling (and surface area limited regime) described in this research. Further, as they made their own magnesium hydroxide solutions from dry Mg(OH)₂ powder with an assumed uniform particle radius (taken as the average measured particle radius), it does not translate to applications of the industrial-grade magnesia slurry that is used in treatment plant operations. Altogether, as their model is specific to coal-fired power plants and CO₂ separation, it does not have the flexibility, experimental validation/verification, jar-test framework, or solution specific considerations (such as temperature) necessary for water/wastewater treatment plant applications.

Temperature functionality, while potentially important in some processes, will likely have a far smaller effect when applied to effective dissolution rates in water and wastewater treatment. This is primarily because of the much smaller variability of water temperature over short time scales. For example, over the two-week field experimentation period, the full range of measured sewage temperatures at the outlet of the Chesapeake collection system was less than 2°C. Nonetheless, if seasonal temperature variability is significant, the model should be updated with a new $*pK_{s0}$ value for Mg(OH)₂ at the solution temperature, as well as updated fits for κ and β .

4.6 Lab and Computational Results

The pH over time and the final dissolved and suspended magnesium concentrations were measured for 14 different “scenarios” defined by the concentration of slurry added and the initial $C_T/pH_0/Mg_0$ of the synthetic water. For each scenario, three duplicate runs were performed to

mitigate the experimental uncertainties — most notably the 2 percent slurry dosage error and any unintended CO₂ evolution (despite the cover) that caused errors in alkalinity estimation (C_T changes) as CO₂ evolves or is absorbed. The average minute-by-minute pH response and final magnesium concentrations were calculated for each triplicate, and these datasets were used to calibrate and evaluate the dissolution model.

4.6.1 Fitting Model Parameters

The four empirical model parameters (κ , β , m , and α) were fit in MATLAB. Starting with a set of best-estimate parameters, $P_0 = [\kappa_{est}, \beta_{est}, m_{est}, \text{ and } \alpha_{est}]$, the model described in Equation 4.54 was evaluated at each time-step over the length of an experimental run (40 minutes for the synthetic experiments) using the VSVO MATLAB solver. The slurry dissolved over each time step was converted into a resulting change in alkalinity; subsequently, the new solution pH was calculated. This initial model fit (using P_0) produced a pair of arrays, Mg_P and Alk_P , that hold the model's predictions for both magnesium and alkalinity over time (and thus pH over time when C_T is known). While the model was solved using variable step sizes and orders to prevent truncation errors, for comparison and fitting purposes it returned values over the same time steps as the experimental measurements. The total sum of squared residuals (SSR) was then computed between the predicted and measured pH responses to produce an estimate of the model's goodness-of-fit for each scenario. The total root-mean-squared error (RMSE) for all scenario residuals was calculated and served as the objective function for fitting the four parameters in P_0 .

The set of best-fit parameters, P , was computed using an unconstrained, nonlinear programming solver included in MATLAB that solved the multivariate function and minimized the total RMSE. This fitting method was selected as it was the most efficient. It also was successful at avoiding local minima that can obfuscate this type of fitting process.

The best fit across all average pH responses for each of the 14 synthetic scenarios evaluated in this study was calculated as:

$$P = [\kappa, \beta, m, \alpha] = [5.001 \times 10^{-4}, 11.84, 0.2278, 297.6] \quad (4.56)$$

This fit, as well as the estimations of surface area and particle sizes, is specific to Slurry A, and should be revised if characterizing a different magnesia slurry.

Future calibration jar tests should include jars containing the maximum and minimum expected alkalinity at the maximum and minimum expected starting pH (at least four experiments). Additional calibration tests may be necessary when solutions are between pH 7.0-9.0, as the alkalinity has the lowest buffer capacity in this range, which magnifies (or tends to magnify) the effects of experimental error.

4.6.2 Modeled pH Responses

The 14 batch laboratory scenarios used for this fit are organized in Table 4.3. Each scenario was given a single-letter name and consisted of a unique combination of initial pH (pH_0), concentration of slurry added (Mg_a), initial background dissolved magnesium (Mg_0), and total inorganic carbon in the closed system (C_T). A plot of both the predicted and average measured pH responses of each of the 14 setups are split between Figures 4.13 through 4.16. The datasets were split for readability and partitioned into groups that share initial slurry, inorganic carbon, and magnesium concentrations; however, all were run using Slurry A.

The pH response to the addition of 3.2 mM (100 $\mu\text{L/L}$) of slurry to synthetic wastewater containing 8.3 mM of total carbon and no background magnesium, beginning at one of six initial pHs (5.5, 6.0, 6.5, 7, 7.5, 8.5), is shown in Figure 4.13. While this plot fits most of the data exceptionally well, it particularly highlights the region between pH 7.3 and 8.3 where dissolved carbon is predominantly in the form of bicarbonate, and the pH response over this range is subsequently more rapid due to the diminished adjusted buffer capacity and an unsaturated solution. In other words, a small change in ΔAlk_{total} results in a larger increase in pH. This rapid response magnifies slight experimental errors (such as the expected ± 2 percent slurry dosage error or slight C_T loss during preparation and experimentation. In addition, the pH probe response time may lag behind the actual results in some cases. This assessment is further supported by the fact that Scenarios C, H, and J (initial pH 6.5, 6.5, and 6.0, respectively) displayed the largest variability between duplicate runs

Table 4.3: The 14 synthetic wastewater scenarios used to calibrate and evaluate the model. These were run in triplicate in sealed beakers. The pH response of each scenario is shown in one of four succeeding figures, as indicated. The initial pH, magnesium dose, initial dissolved magnesium, and total dissolved inorganic carbon are given by pH_0 , Mg_a , Mg_0 , and C_T , respectively.

Label	pH_0	Mg_a mM	Mg_0 mM	C_T mM	Runs	Figure
A	5.5	3.2	0	8.3	3	4.13
B	6.0	3.2	0	8.3	3	4.13
C	6.5	3.2	0	8.3	3	4.13
D	7.0	3.2	0	8.3	3	4.13
E	7.5	3.2	0	8.3	3	4.13
F	8.5	3.2	0	8.3	3	4.13
G	6.0	3.2	0	16.7	3	4.14
H	6.5	3.2	0	16.7	3	4.14
I	7.0	3.2	0	16.7	3	4.14
J	6.0	1.6	0	8.3	3	4.15
K	7.0	1.6	0	8.3	3	4.15
L	8.5	1.6	0	8.3	3	4.15
M	6.0	1.6	5.0	8.3	1	4.16
N	7.5	3.2	5.0	8.3	1	4.16

over the full 40 minutes (exhibiting a common variance of errors of 0.048, 0.065, and 0.035 pH units, respectively). Nonetheless, the model represents the overall trend and final pH after the initial transition range for these scenarios. For all other scenarios, the initial kinetics appear generally well represented and the final pH equilibrium settled within 0.1 pH points of the average measured values. No other triplicate sets had a variance of errors above 0.016 pH units.

Figures 4.14-4.16 show similar results to Figure 4.13, though the model was evaluated under different conditions. Specifically, Figure 4.14 depicts scenarios with twice the initial carbon, Figure 4.15 shows scenarios with half the slurry dose, and Figure 4.16 has scenarios with 5.0 mM initial background magnesium added as $MgCl_2$ (i.e., more Mg than added with the magnesia dose). Unlike the scenarios depicted in Figure 4.13, the scenarios represented by Figures 4.14-4.16 were not performed as exhaustively across all permutations. They instead serve to evaluate the model under disparate conditions. Further, adding background magnesium (as $MgCl_2$) was not found to have a

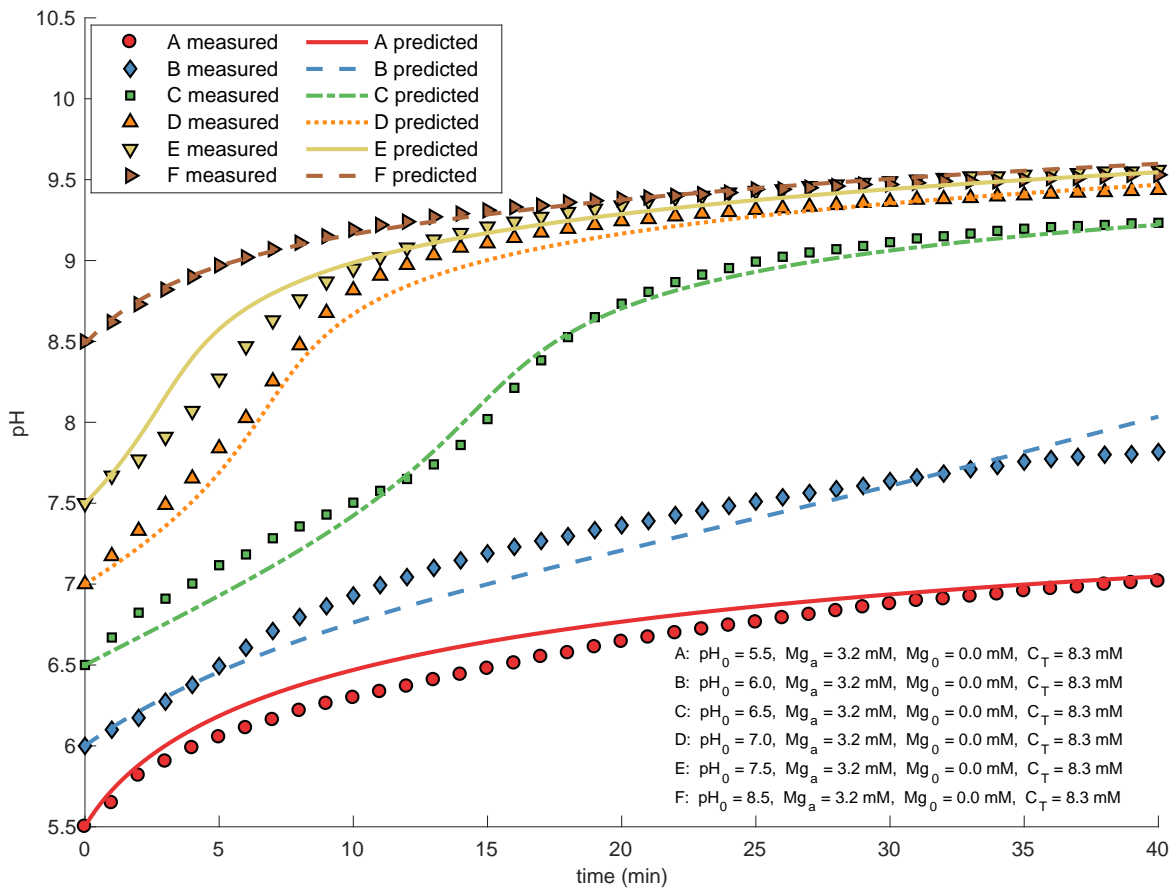


Figure 4.13: The modeled (using values shown in Equation 4.6.1) and average measured pH responses to the addition of 3.2 mM (100 $\mu\text{L/L}$) of slurry to synthetic wastewater containing 8.3 mM of total carbon (0.7 g NaHCO_3/L) and no background magnesium, starting at different initial pH states. The slurries were mixed in a covered jar test beaker at a mean velocity gradient of 100 s^{-1} and an initial ionic strength of 0.01 M as NaCl.

significant impact on the pH response. This makes sense, as a slight change in solution pH has a much larger effect on solubility than a slight change in dissolved $[\text{Mg}^{2+}]$ (see Equations 4.48 and 4.49).

Figures 4.17 and 4.18 show a more detailed picture of the measured and modeled responses to Scenarios K and E, respectively. Specifically, Figure 4.17 shows how the model of Scenario K responds in the transition region, when the added slurry approaches exhaustion while the solution becomes partially saturated with magnesium. Figure 4.18 shows how the asymptotic behavior in Scenario E occurs well before the slurry is exhausted; instead, the dissolution slows because of

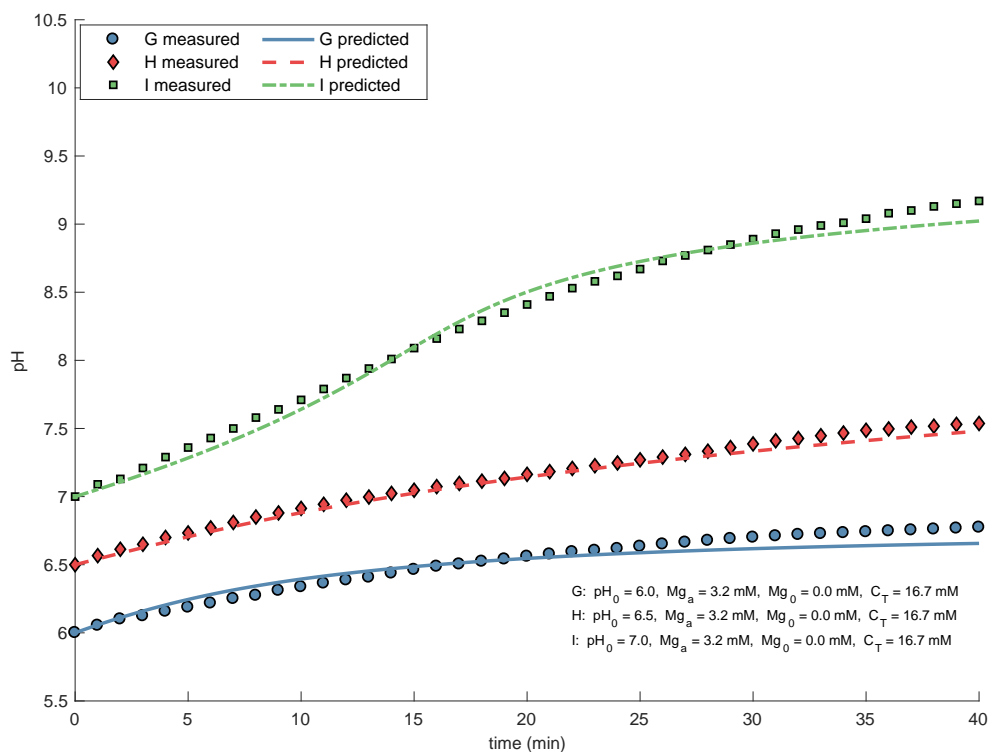


Figure 4.14: The modeled (using values shown in Equation 4.6.1) and average measured pH responses to the addition of 3.2 mM (100 $\mu\text{L/L}$) of slurry to synthetic wastewater containing 16.7 mM of total carbon (1.4 g NaHCO_3/L) and no background magnesium, starting at different initial pH states. The slurries were mixed in a covered jar test beaker at a mean velocity gradient of 100 s^{-1} and an initial ionic strength of 0.01 M (as NaCl).

magnesium saturation.

Acidified filtered and unfiltered samples were taken for selected scenarios after 40 minutes of dissolution, and ICAP-MS measurements of magnesium were logged. The two sets of triplicate samples, Scenarios K and E, were selected because they had different slurry dosages and exhibited the flattest pH slope at 40 minutes. Samples taken from scenarios with more active dissolution were found to continue to dissolve during the sampling and double filtration regimen (1.20 followed by 0.45 μm , a 1-2 minute delay), and returned inconsistent measurements. As such, datasets of filtered magnesium may be used to support the pH measurements, but should not be used alone as a calibration metric. Unfiltered sample measurements of Mg_a showed less uncertainty than their filtered counterparts (unfiltered and acidified should ideally result in 100% of added slurry

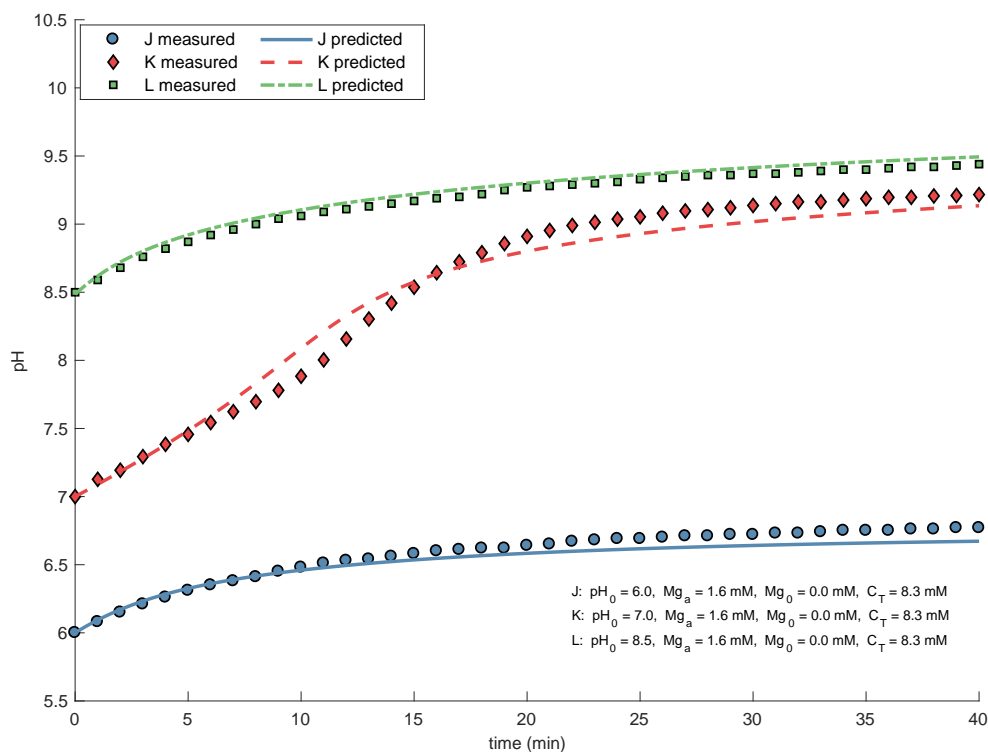


Figure 4.15: The modeled (using values shown in Equation 4.6.1) and average measured pH responses to the addition of 1.6 mM ($50 \mu\text{L/L}$) of slurry to synthetic wastewater containing 8.3 mM of total carbon ($0.7 \text{ g NaHCO}_3/\text{L}$) and no background magnesium, starting at different initial pH states. The slurries were mixed in a covered jar test beaker at a mean velocity gradient of 100 s^{-1} and an initial ionic strength of 0.01 M (as NaCl).

dissolved), suggesting that filtration may be the source of the extra uncertainty of filtered samples. These measurements are included in Figures 4.17(b) and 4.18(b) and compiled in Figure 4.19. They appear to support the model predictions for these two scenarios.

4.6.3 Statistical Analysis of Results

Using the fitted P parameters (Equation 4.6.1), the residuals of all average pH responses were found to be approximately normally distributed. Table 4.4 contains the approximate 95% confidence intervals calculated through a Monte Carlo simulation of residuals and an approximate correlation matrix for the four parameters. The confidence intervals suggest that moderate uncertainty remains in each of the parameter fits. Given the underlying uncertainties working with magnesia slurries,

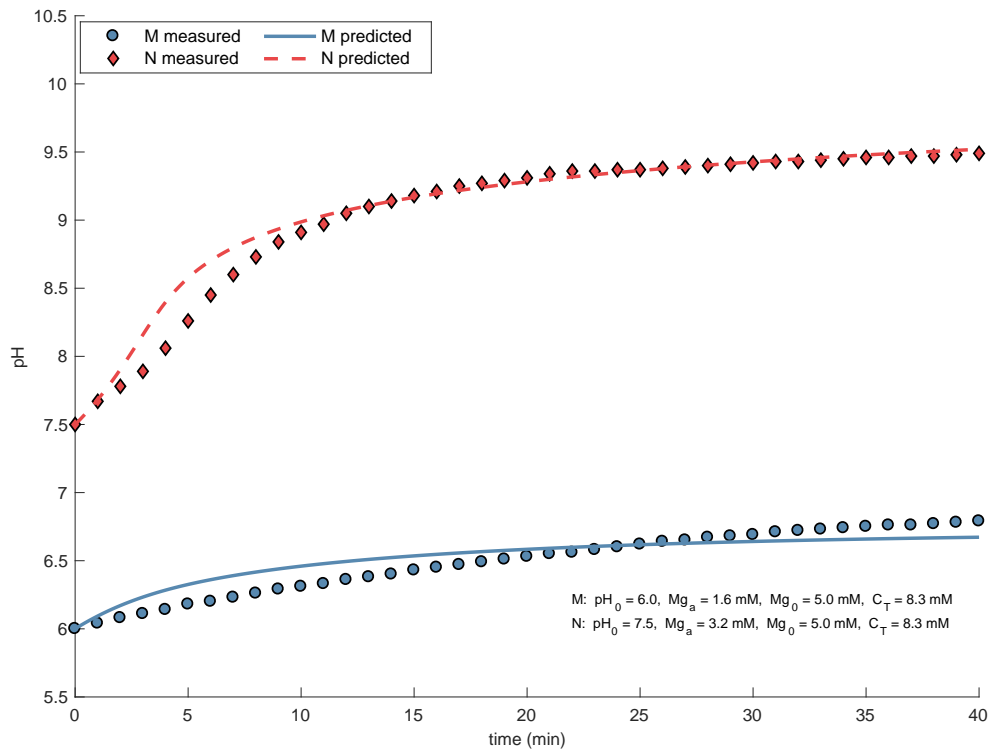


Figure 4.16: The modeled (using values shown in Equation 4.6.1) and measured pH responses to the addition of 1.6 mM and 3.2 mM (100 and 50 $\mu\text{L}/\text{L}$, respectively) of slurry to synthetic wastewater containing 8.3 mM of total carbon (0.7 g NaHCO_3/L) and 5.0 mM of dissolved background magnesium, starting two different initial pH states. Magnesium concentrations in most treatment facilities are generally orders of magnitude less concentrated than this background dose, but even in the rare case that the concentrations are high and alkalinity is relatively low, such in Scenario N, background magnesium at these doses does not appear to have a significant effect on the equilibrium pH. Note: Scenario M appears to dissolve fully in the fast regime (surface saturation dominated), whereas Scenario N crosses into the slow regime (solution saturation dominated).

this is to be expected. If this model is to be used for magnesium doses or alkalinities far outside the typical—but moderately narrow—ranges used in this study, further calibration experiments may prove necessary.

Table 4.5 contains the approximate correlation matrix for the four fitted parameters. While correlation between parameters in this model is expected to be relatively high due to the breadth of the confidence intervals (as one variable may be able to “make up” for a slightly inaccurate fit of another if collinear), the κ parameter is revealed as the most uncertain. The correlation between κ and β (and less so, κ and m) suggest that there may be some collinearity within the structure of

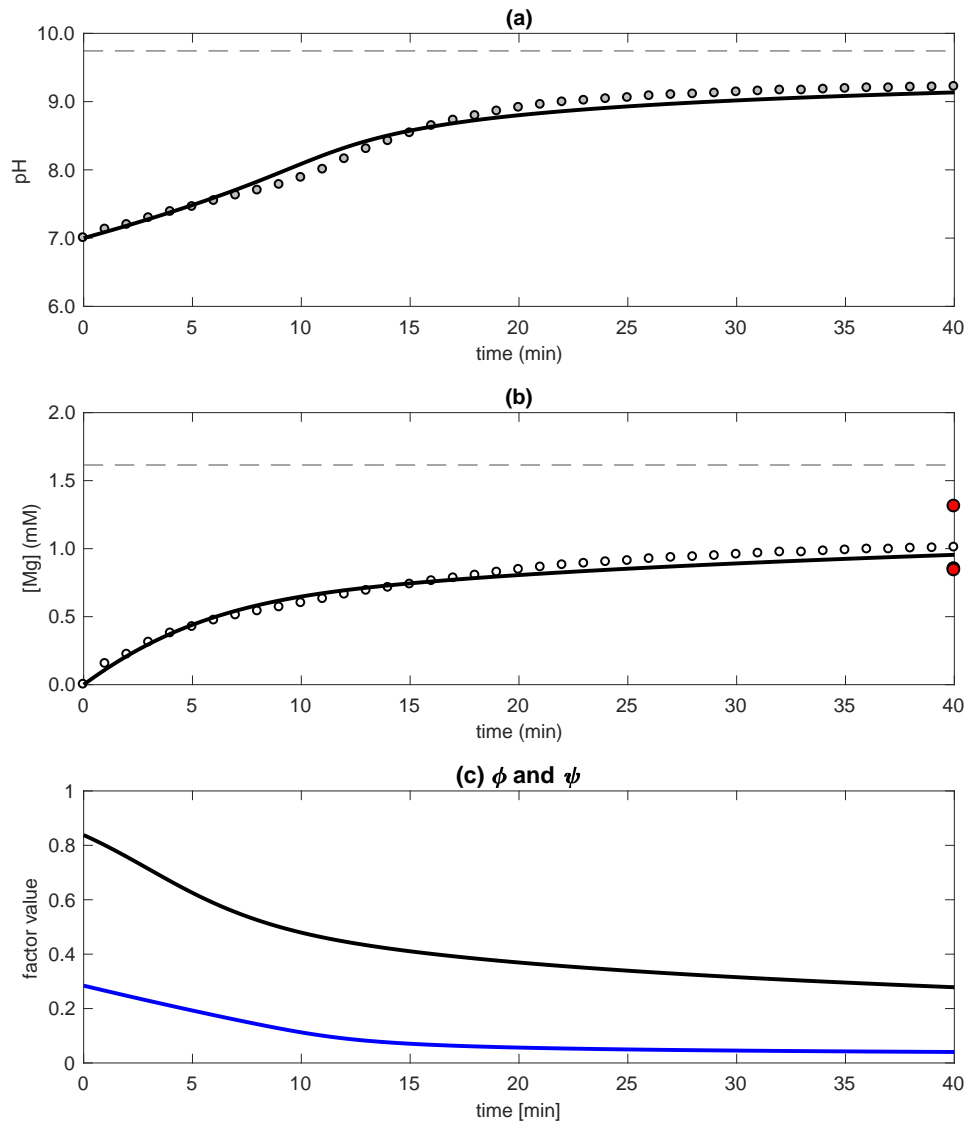


Figure 4.17: Subplot (a) shows the model (solid line) and average measured data (circles) for the pH response of Scenario K (3 total experiments, $pH_0 = 7.0$, $C_T = 8.3$ mM, $Mg_a = 1.6$ mM, and $Mg_0 = 0$ mM). The dashed line represents the expected equilibrium pH for the given slurry dose and water characteristics, i.e. at 100% dissolution. Subplot (b) shows the model (solid line) and the corresponding dissolved magnesium values as derived from the measured pH response data (white circles). The dashed line represents the total amount of magnesium added as $Mg(OH)_2$. The red markers represent the measured undissolved magnesium at 40 minutes for each of the three experiments in the triplicate (two markers are superimposed at 0.84 and 0.85 mM). Subplot (c) contains the model values for the intermediate ϕ (black line) and ψ (blue line) terms.

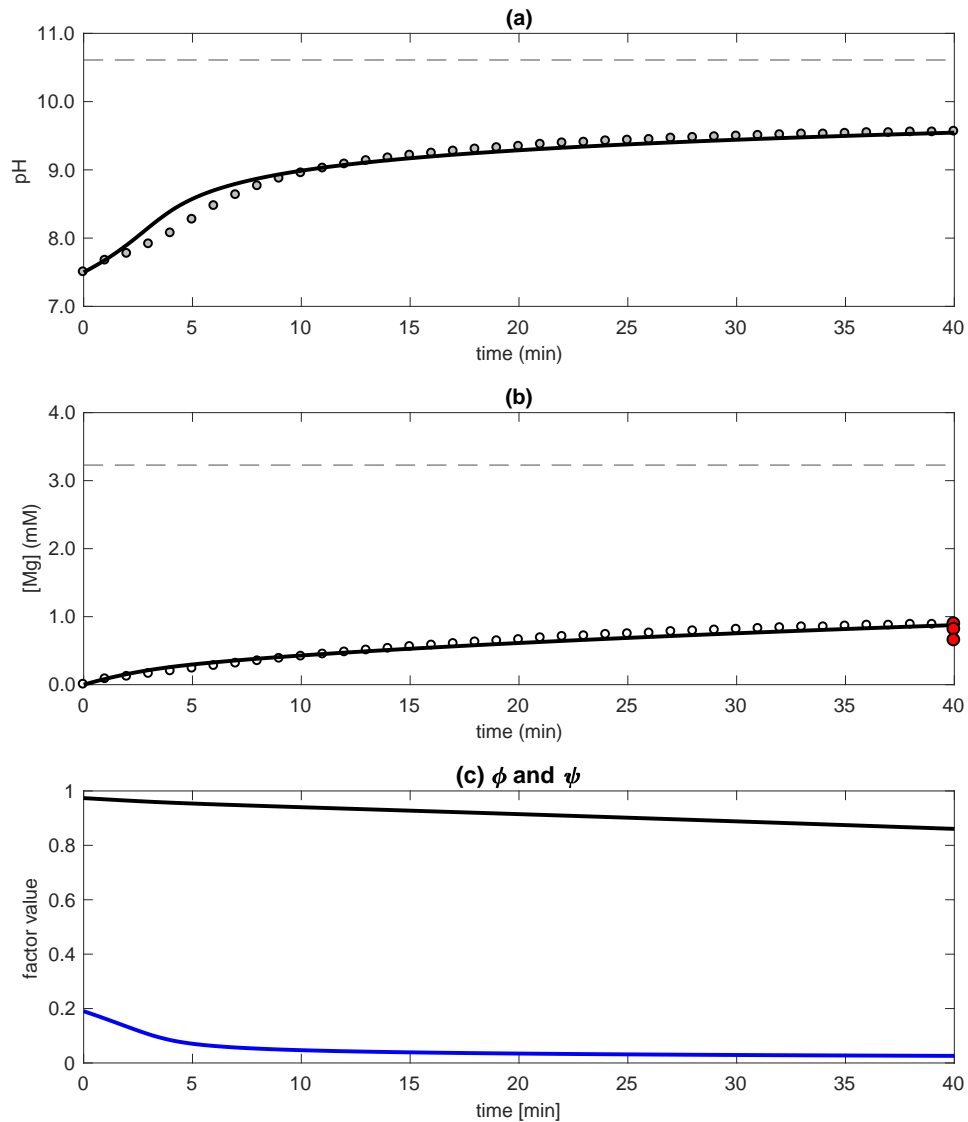


Figure 4.18: Subplot (a) shows the model (solid line) and average measured data (circles) for the pH response of Scenario E (3 total experiments, $pH_0 = 7.5$, $C_T = 8.3$ mM, $Mg_a = 3.2$ mM, and $Mg_0 = 0$ mM). The dashed line represents the expected equilibrium pH for the given slurry dose and water characteristics, i.e. at 100% dissolution. Subplot (b) shows the model (solid line) and the corresponding dissolved magnesium values as derived from the measured pH response data (white circles). The dashed line represents the total amount of magnesium added as $\text{Mg}(\text{OH})_2$. The red markers represent the measured undissolved magnesium at 40 minutes for each of the three experiments in the triplicate. Subplot (c) contains the model values for the intermediate ϕ (black line) and ψ (blue line) terms.

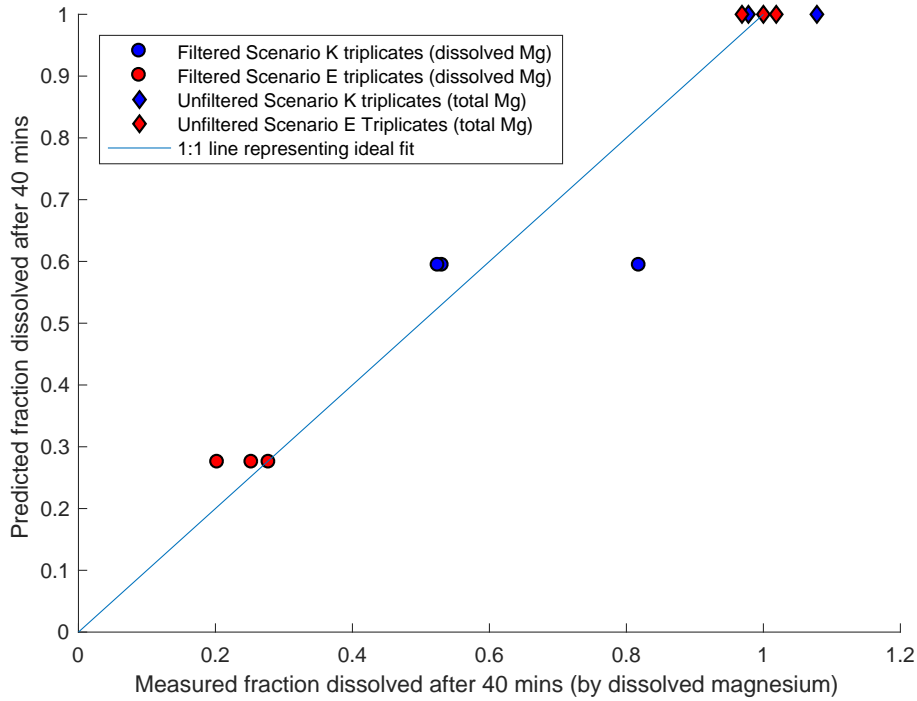


Figure 4.19: ICAP-MS measurements of magnesium for filtered and unfiltered samples for each Scenarios K and E triplicate, taken after 40 minutes of dissolution. Magnesium measured in filtered samples represents the mass of particles that have already dissolved by the 40-minute mark. Magnesium measured in unfiltered (and acidified) samples represents the accuracy of the initial slurry dosage. Data points that coincide with the blue 1:1 reference line have perfect agreement between measurements and predictions. Values from unfiltered samples that fall above 1.0 on the abscissa signify that the slurry was dosed at a higher concentration than intended. The outlier in the Scenario K filtered data may also be the result of filter failure.

Table 4.4: The fitted model parameters and approximate 95% confidence intervals calculated using a generic Monte Carlo simulation of residuals.

Parameter	Fitted Value	Approx. 95% Confidence Interval	
		Lower Bound	Upper Bound
κ	5.001×10^{-4}	4.577×10^{-4}	5.424×10^{-4}
β	11.84	10.63	13.05
m	0.2278	0.2194	0.2362
α	297.6	277.6	317.7

the model or contained within the calibration data. This suggests that as the mechanisms are better understood, a reparameterization may be appropriate. Nonetheless, this model addresses the current

demands of water and wastewater treatment plants better than the saturation-only metal-oxide kinetic model from [Bowers & Higgs \(1987\)](#) as well as the magnesia dissolution model developed in [Bharadwaja et al. \(2013\)](#) for CO₂ separation in coal-fired power plants.

Table 4.5: Approximate correlation matrix for the fitted parameters

Parameter	κ	β	m	α
κ	1			
β	0.938	1		
m	-0.863	-0.734	1	
α	-0.399	-0.619	0.328	1

4.7 Field Results and Discussion

4.7.1 Chesapeake Collection System Results

The model and empirical fit were put to the test at a 55 MGD wastewater treatment plant on Chesapeake Bay. Baselines were gathered over several days before two separate experiments were run. The first experiment (Test 1) entailed adding 0.49 to 1.11 mM (10 to 27 mg/L) of Slurry A into the collection system at a pump station over the course of a 22-hour period. Although the slurry was pumped at a constant rate, magnesium addition rate was not constant as the rate of flow in the collection system varied over the course of the day. During this period, alkalinity and magnesium (filtered/acidified and unfiltered) measurements were taken continuously at the pump station and at the influent to the plant. In addition, pairs of filtered/unfiltered measurements were taken, and Mg was measured by ICAP. Figure 4.20 contains these acidified measurements for Test 1 (taken over 22-hour period). Most of the data points indicate that Mg(OH)₂ was 100 percent dissolved by the time the flow reached the plant, i.e., the filtered Mg \approx the unfiltered Mg.

Despite the normal difficulties inherent in highly variable systems (variations in slurry pumping rates, variable wastewater flows, variable wastewater composition, etc.) it is reasonable to conclude from Figure 4.20 that the slurry was fully exhausted at dosage rates below 20 mg/L (0.82 mM). At doses between 20 and 27 mg/L (0.82 to 1.11 mM), the data was slightly less consistent, but

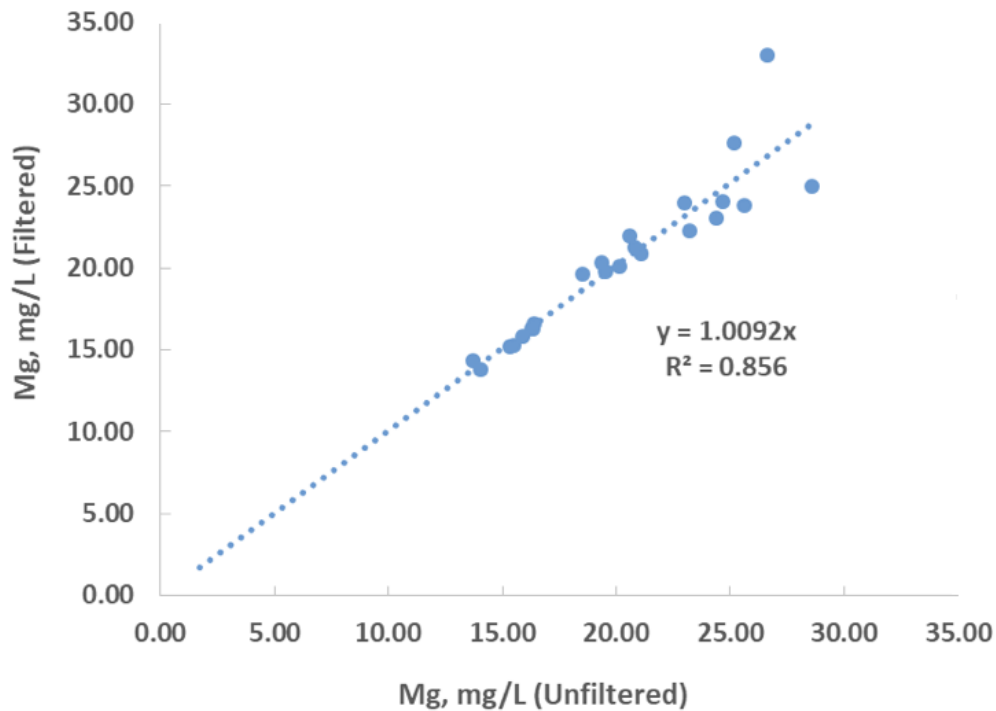


Figure 4.20: Magnesium measurements (filtered and acidified vs. unfiltered and acidified) taken at the plant influent (collection system effluent) during Test 1. The 1:1 slope implies complete dissolution of the slurry.

suggested most (but not necessarily all) of the magnesia was dissolved.

The model was used to estimate the fraction of slurry that would dissolve over the 280 minute residence time in the sewer. This estimation was made at the maximum and minimum slurry dosage rates of 0.53 to 1.11 mM (13 to 27 mg/L) and are displayed in Table 4.6.

The measurements in Figure 4.20 appear to agree with the model results included in Table 4.6. After slurry addition, the anoxic “plug-flow” distribution system took approximately 280 minutes to reach the plant, resulting in a model prediction of between 97 percent and 83 percent slurry dissolution at the end of the pipe (depending on the sewage flow rate). These results suggest that the dosage of 1.11 mM may be slightly too high if full dissolution after 280 minutes is necessary. Figure 4.21 shows model predictions of the percent of slurry still undissolved and the change in dissolved magnesium (ΔMg) as a function of time. The reported maximum and minimum values

Table 4.6: Model parameters and predictions for the maximum and minimum dosages during Test 1 at the Chesapeake Bay treatment plant. Specifically, the left portion of the table reports initial conditions and the right portion shows the amount of time predicted to achieve different percentages of slurry dissolution. After slurry addition, the anoxic “plug-flow” collection system took approximately 280 minutes to reach the plant, resulting in a model prediction of between 97 and 83% slurry dissolution at the end of the pipe (depending on the sewage flow rate). Initial water conditions at the addition point were taken at the beginning of the 22-hour period.

Test	Measured initial conditions				Time until percent dissolved (predicted)					
	pH_0	Alk_0	C_T	Mg_a	25%	50%	75%	90%	95%	99%
		meq	mM	mM	mins	mins	mins	mins	mins	mins
1_{min}	6.89	2.99	3.75	0.53	3	8	29	109	203	478
1_{max}	6.89	2.99	3.75	1.11	4	25	156	504	>900	>900

represent an envelope of dosages caused by the variable flow rate in the sewer over the 22-hour experiment.

The second experiment (Test 2) was performed over the course of a week. The slurry was pumped at effective rates between 0.19 to 0.37 mM (4.7 to 9.0 mg/L) during standard operating hours, then turned off for nine hours during the night. Samples were taken, consistent with the previous test. The travel time of the pH spike and magnesium plug at the beginning of the day was averaged to estimate the 4 hour 40 minute travel time, with minimal variation. The dissolution model, using the parameters fit empirically by the laboratory experiments (see Table 4.4), estimated the fraction of slurry still undissolved at the end of the collection system. The model expected between 100% and 94% of the slurry to be dissolved under minimum and maximum effective $Mg(OH)_2$ dosages, respectively. See Table 4.7 for an outline of both dissolution simulations.

While there was no way to directly confirm that most of its travel time had elapsed before the slurry had dissolved, the pH was still significantly elevated (compared to the baseline) when the waste stream arrived at the plant influent (about 0.50-0.70 pH points higher during Test 2). This pH difference is consistent with the expected alkalinity contribution of only a fraction of the slurry, but microbiological activity is expected to lower the pH significantly through the production of H_2S and organic acids (Gutierrez et al., 2009). Baseline (non-magnesia) experiments can provide a rough estimate of the magnitude of this biological alkalinity reduction, as is used in this research. In

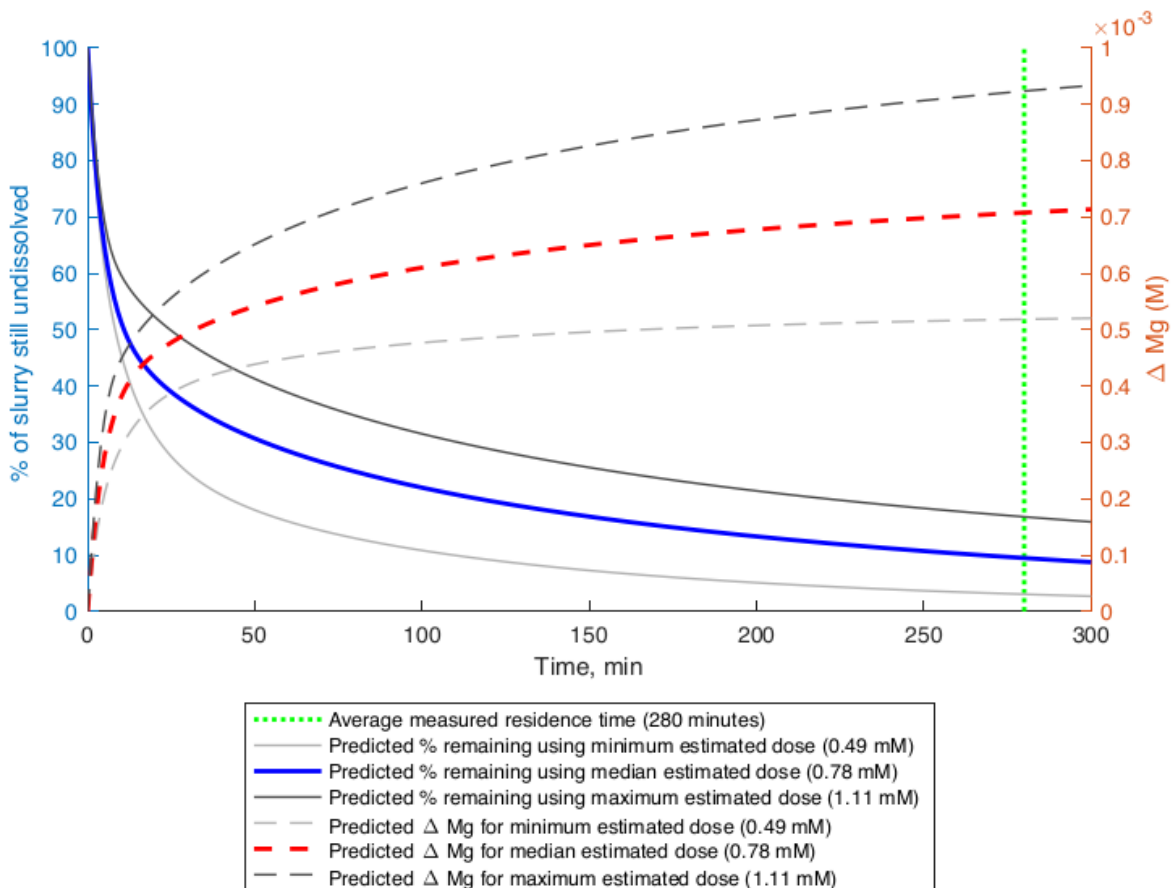


Figure 4.21: Model predictions of the wastewater state over the 280 minute travel time in the collection system of the Chesapeake Bay treatment plant. The solid lines correspond to the left axis and depict model predictions of the percent of slurry still undissolved at time t . The dashed lines correspond to the right axis, and represent the predicted change in dissolved magnesium (Δ Mg) as a function of time. The maximum and minimum values for both datasets represent an envelope of effective dosages caused by the variable flow rate in the sewer over the 22-hour experiment.

many cases, when biological activity (and, thus, H^+ addition) is minimal under baseline conditions, influent conditions alone may be sufficient to predict effluent pH. Future studies could investigate the change in biological activity when the slurry introduces magnesium and an elevated pH to the system. The change in alkalinity due to biological activity could be estimated as long as the alkalinity addition from the dissolving slurry (through accurate measurements of dissolved magnesium) is known. This “biological alkalinity” model could then be included within the dissolution model by slightly decreasing Alk_{total} each time step (either by a fixed value or using a pH-dependent

Table 4.7: Model parameters and predictions for the maximum and minimum dosages during Test 2 at the Chesapeake Bay treatment plant. Specifically, the left portion of the table reports initial conditions and the right portion shows the amount of time predicted to achieve different percentages of slurry dissolution. Note: After slurry addition, the anoxic “plug-flow” collection system took approximately 280 minutes to reach the plant, resulting in a model prediction of between 100 and 94% slurry dissolution at the end of the pipe.

Test	Measured initial conditions				Time until percent dissolved (predicted)					
	pH_0	Alk_0	C_T	Mg_a	25%	50%	75%	90%	95%	99%
		meq	mM	mM	mins	mins	mins	mins	mins	mins
2_{min}	6.89	2.99	3.75	0.19	2	6	18	39	57	105
2_{max}	7.17	3.11	3.53	0.37	3	11	57	181	300	630

submodel).

Characterization of microbiological pH effects promotes more accurate predictions of the collection system’s effluent pH (and, subsequently, better slurry dosage regimes). In all cases, measuring the change in the alkalinity response between the baseline and magnesia experiments is a critical metric in modeling dissolution (alongside pH). In addition, hardness and magnesium were measured to verify the conclusions of the alkalinity measurements; however, filtration difficulties due to high turbidity limited the frequency of magnesium measurements.

The average change in alkalinity measured at the outlet was comparable to the total alkalinity expected from the magnesia dose. For example, when comparing the baseline experiments (no slurry) to the Test 2 slurry minimum dosing regimen of 0.19 mM, the average alkalinity difference at the outlet equated to a magnesium dose of 0.21 mM. The maximum dosing regimen was even closer: the expected dose of 0.37 mM was matched by an apparent dose of 0.37 mM. These conclusions were supported by the average change in hardness, although this method afforded less precision.

The odor reduction benefits of elevating the waste stream pH past 8.5 [Gutierrez et al. \(2009\)](#); [Firer et al. \(2008\)](#); [Talaiekhosani et al. \(2016\)](#); [Jensen \(1990\)](#) suggest that the ideal regimen for this situation might include a higher slurry dose (though not significantly higher, due to diminished buffer capacity between pH 7.3 and 8.3). This excess will likely work to counteract the reduction of alkalinity caused by H_2S converting to H_2SO_4 upon introduction to aerobic conditions ($pK_a \approx 7.04$

at 18°C); however, this depends on many waste-specific properties, such as pH and temperature.

4.7.2 North Carolina Lake Water Results

A large grab sample of water was taken from the influent of a 120 MGD drinking water treatment plant in a North Carolina municipality. Six covered jar test dissolution experiments were performed on this water, following the procedures outlined in Section 4.3. Slurry A was added at four different concentrations, and the sample was used promptly to prevent excessive microbiological activity or pH changes. Table 4.8 outlines the initial water properties.

Table 4.8: Measured initial properties and magnesium dose for the jar tests of low-alkalinity North Carolina lake water (drinking water source). Note, initial pH was not altered from its original state. Slr_a represents the volume of slurry added to accomplish the dosage prescribed by Mg_a .

Label	pH_0	Alk_0	C_T	Mg_0	Mg_a	Slr_a
		meq	mM	mM	mM	$\mu\text{L/L}$
O	7.03	0.31	0.37	0.0	0.065	2.0
P	7.10	0.32	0.37	0.0	0.161	5.0
Q	7.05	0.31	0.37	0.0	0.065	2.0
R	7.15	0.32	0.37	0.0	0.161	5.0
S	7.00	0.31	0.37	0.0	0.097	3.0
T	7.00	0.31	0.37	0.0	0.129	4.0

The North Carolina grab sample had abnormally low alkalinity, which necessitated an extremely low (and diluted) magnesium dose. While data and the model agreed on the eventual pH equilibrium, the synthetically fit parameters did a poor job of predicting the dissolution kinetics. Specifically, solutions with very low alkalinity (below about 16 ± 4 mg/L as CaCO_3) and small slurry doses dissolve more slowly than predicted. Clearly, the calibration state derived using synthetic data described in Table 4.4 is not universal. This may be the result of simplified surface area or particle size characterizations, an artifact of model colinearity, errors in measurement due to low alkalinity and slurry dosage, organic acids present that compete for OH^- , or unknown factors. A universal dissolution model would be ideal but is far from necessary, especially given the complexity of the system involved.

As can be seen in Figure 4.22, the model fit exceptionally well when recalibrated using the six sets of low alkalinity data from Table 4.8. This fit is given by:

$$P_{O-T} = [\kappa, \beta, m, \alpha] = [1.58 \times 10^{-6}, 4.71, 0.345, 39.4] \quad (4.57)$$

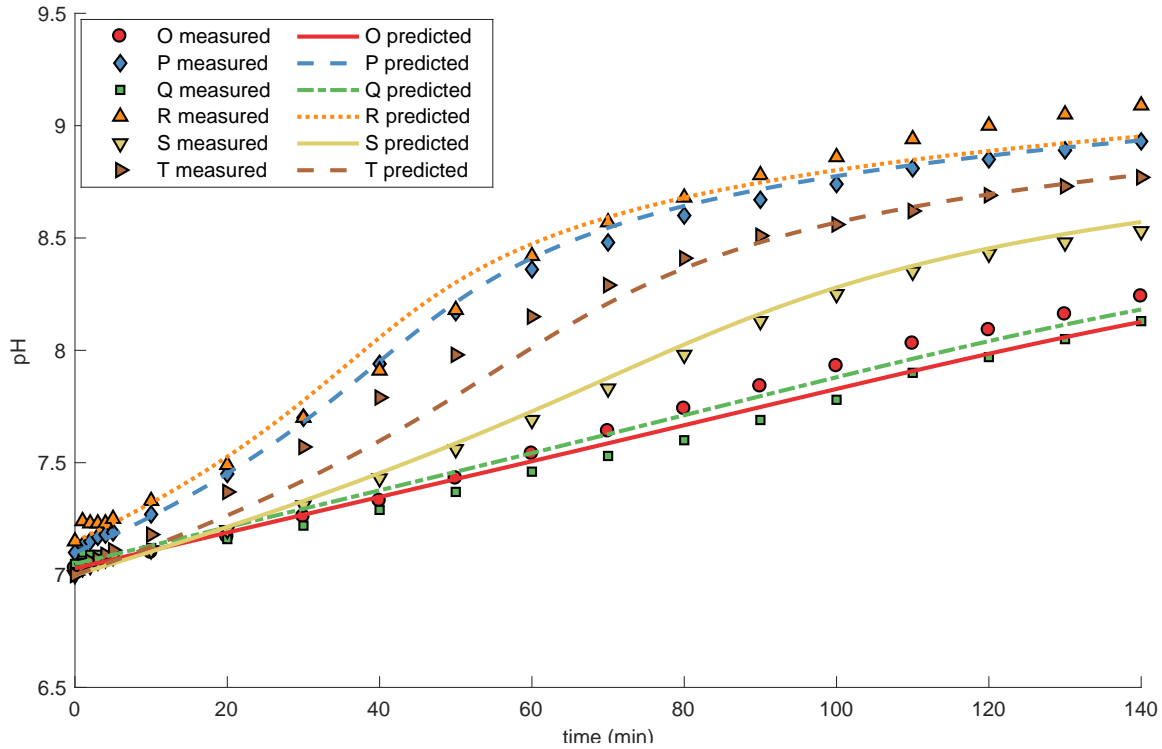


Figure 4.22: The model (solid line) and measured data (markers) for the pH response of Scenarios O-T run in sampled North Carolina lake water. In this case, the model was fit to all six data points. The pH data was not performed in triplicate and was taken every minute for the first 5 minutes (to better capture early pH functionality) and then once every 10 minutes after that.

In addition to a model calibration using the entire dataset (Table 4.4), the model was also calibrated using only the data from Scenarios O and P. These two scenarios consist of both a low and (comparatively) high alkalinity and were used to evaluate the effectiveness of the model when calibrated to a small data set. This small-set calibration, given by:

$$P_{OP} = [\kappa, \beta, m, \alpha] = [1.68 \times 10^{-6}, 5.17, 0.340, 39.0] \quad (4.58)$$

was then used to predict the pH response for Scenarios S and T, and was found to adequately predict their pH profile during dissolution. This prediction can be seen in Figure 4.23.

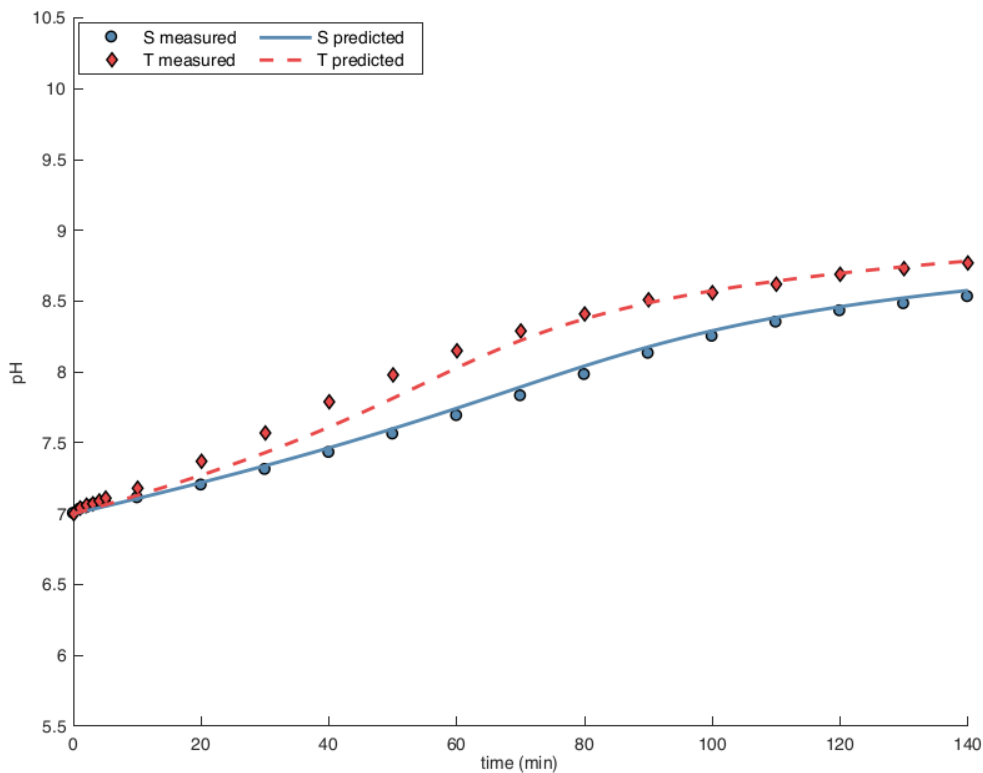


Figure 4.23: The measured data (markers) for the pH response of Scenarios S and T run in sampled North Carolina lake water. The model (solid line) predicted the pH response of Scenarios S and T using parameters derived from only the Scenario O and P datasets (which use different slurry dosages than S and T). In other words, the model was fit using two jar test experiments and this fit was used to predict the results of two other jar test experiments. The pH data was not performed in triplicate and was taken every minute for the first 5 minutes (to better capture early pH functionality) and then once every 10 minutes after that.

The fit represented in Figure 4.23 suggests that should treatment plants calibrate the model with a small number of jar tests, the fit can do an adequate job of predicting the pH response in the future. After an initial calibration, further jar testing of grab samples over the course of a magnesia trial will improve the fit of model parameters.

Altogether, these field results suggest that when calibrated across a realistic but relatively narrow range of alkalinity or slurry dosages, the parameters do not always successfully model environments outside of that range. However, the results also serve to demonstrate that the model

can be recalibrated successfully at a low initial alkalinity. As drinking water sources generally do not experience extreme short-term variability of alkalinity, this calibration requirement should not undermine the practicality of the model. On the contrary, the simplicity and jar test setting of calibration experiments affords the model the flexibility necessary for application in a wide variety of treatment processes and conditions.

4.8 Kinetic Model Conclusions

The proposed kinetic model for magnesium hydroxide dissolution was found to address the predictive needs of water and wastewater treatment operations. By modeling $\text{Mg}(\text{OH})_2$ dissolution using a surface-saturation-dominated regime in conjunction with a solution-saturation-dominated regime, the model accurately predicts the asymptotic behavior of pH responses over the wide range of conditions expected within treatment processes. The use of simulated, shrinking particles was found to successfully model surface area depletion and slurry exhaustion. While immediately useful in treatment operations, this information may also help manufacturers formulate new magnesia slurries that are tailored to produce desired pH/alkalinity responses. In addition, modifications to the thermodynamic model developed in [Bowers & Higgs \(1987\)](#) were found to accurately predict the pH response during the solution-saturation-dominated regime.

There are many direct applications for which this model will be immediately valuable, as evidenced by the field experimentation in this study and the growing implementation of magnesia in water and wastewater treatment. The fact that no other magnesium hydroxide kinetic models have been published specifically for use in municipal water and wastewater treatment only serves to enhance the value of the model. Further, the incorporation and calibration of slurry-specific properties allows the model to be implemented across a wide range of manufacturer-specific magnesia properties. In addition to its ability to replace hazardous or problematic chemicals such as NaOH and $\text{Ca}(\text{OH})_2$ in existing processes, the model's ability to predict the pH and alkalinity response of a slow-release magnesia dose allows for far more comprehensive and integrated approaches to alkalinity, pH, and odor control in collection and treatment systems.

Chapter 5

Conclusions

Magnesium hydroxide has the potential to develop into a ubiquitous and essential component of water and wastewater treatment. Its non-hazardous classification and low cost makes it a preferable source of alkalinity for existing processes. Further, the slow release of alkalinity from magnesia slurry allows new processes to be developed that cannot accommodate fast-dissolving additives like NaOH and $\text{Ca}(\text{OH})_2$. Per this study's field trials, $\text{Mg}(\text{OH})_2$ has been employed to reduce the odor in collection systems and to elevate the pH of raw water; however, it can also maintain an elevated pH throughout nitrification and supply valuable nutrients to waste biomass and in drinking water. Its low solubility prevents overdosing and it will not produce boiler scale or extra solids for disposal. Nonetheless, plant operators are often reluctant to use magnesium hydroxide slurries for two reasons: they are concerned about the precipitation of struvite and they cannot predict the gradual pH response of dissolving slurry. This research proposes a practical solution to both obstacles.

The StrPI model accurately predicted struvite precipitation in both the lab and the field. Calibration can be used to account for local pH spikes, uncertainties in waste composition, and safety factors. This flexibility also allows the model to be applied to both foulant prevention schemes and struvite recovery processes. Since the model can be quickly calculated with readily measurable values, it is ideal for practical application in municipal treatment processes.

Similarly, the kinetic model for magnesium hydroxide provides a robust solution for predicting the pH response of dissolving slurries. These predictions can provide insight into existing processes, which can dramatically improve slurry dosing regimens. The model can also serve as a framework on which to develop more complex dosing schemes that span multiple processes. Figure 5.1 contains a conceptual diagram of this integrated approach when applied to the Chesapeake Bay wastewater treatment plant.

REFERENCES

- Aage H., Andersen B., Blom A., Jensen I., 1997, *Journal of Radioanalytical and Nuclear Chemistry*, 223, 1–2, 213
- Ali I., Schneider P., 2008, *Chemical Engineering Science*, 63, 3514
- Amaral L., Oliveira I., Bonadia P., Salomao R., Pandolfelli V., 2011, *Ceramics International*, 37, 1537
- Ancheyta J., 2017, *Chemical Reaction Kinetics: Concepts, Methods and Case Studies*, John Wiley & Sons, Inc., New York
- Ang A., Tang W., 2007, *Probability Concepts in Engineering—Emphasis on Applications in Civil and Environmental Engineering*, John Wiley & Sons, Inc., New York
- Averill B., Eldredge P., 2012, *Principles of General Chemistry*, Creative Commons, Mountain View, 1st edn.
- Barnes N., Bowers A., 2017, *Chemical Engineering Science*, 161, 178
- Barnes N., Bowers A., Madolora M., 2018, *Journal of Environmental Science and Engineering*, 7, 404
- Benisch M., Clark C., Sprick R., Baur R., 2000, *WEF Operations Forum*
- Bennett D. A., Chang S. S., Cooper D. E., Dinan J., Hofmann E. L., Barry T. M., 2001, *Risk Assessment Guidance for Superfund*, vol. 3, United States Environmental Protection Agency Office of Emergency and Remedial Response
- Bharadwaja H., Leea J., Lia X., Liua Z., Keenerb T., 2013, *Journal of Hazardous Materials*, 250–251, 292
- Bhuiyan M., Mavinic D., Beckie R., 2007, *Environmental Technology*, 28, 9, 1015
- Birchal V., Rocha S., Mansur M., Ciminelli V., 2001, *Canadian Journal of Chemical Engineering*, 79, 507
- Blandamer M., Burgess J., Robertson R., Scott J., 1982, *Chemical Reviews*, 82, 3, 259
- Bogner A., Thollet G., Basset D., Jouneau P., Gauthier C., 2005, *Ultramicroscopy*, 104, 3-4, 290
- Borgerding J., 1972, *Journal Water Pollution Control Fed.*, 44, 5, 813
- Bouropoulos N., Koutsoukos P., 2000, *Journal Crystal Growth*, 213, 381
- Bowers A. R., Higgs T. A., 1987, *Water, Air, and Soil Pollution*, 32, 129
- Buchanan J., Mote C., Robinson R., 1994, *Transactions of the American Society of Agricultural Engineers*, 37, 617

Cornwell D., Bishop M., 1975, *Journal (American Water Works Association)*, 75, 9, 470

Das D., Keinath T., Parker D., Walhberg E., 1993, *Water Environment Research*, 65, 138

De Jonge N., Ross F., 2011, *Nature Nanotechnology*, 6, 11, 695

Doyle J., Parsons S., 2002, *Water Research*, 36, 3925

Durrant A., Scrimshaw M., Stratful I., Lester J., 1999, *Environmental Technology*, 20, 749

Elimelech M., Jia X., Gregory J., Williams R., 1998, *Particle Deposition and Aggregation: Measurement, Modelling and Simulation (Colloid and Surface Engineering)*, Butterworth-Heinemann, 1st edn.

Fedorockova A., Raschman P., 2008, *Chemical Engineering Journal*, 143, 265

Firer D., Friedler E., Lahav O., 2008, *Science of the Total Environment*, 392, 145

Goldberg R., Kishore N., Lennen R., 2002, *Journal Physical and Chemical Reference Data*, 31, 2, 231

Gutierrez O., Park D., Sharma K., Yuan Z., 2009, *Water Research*, 43, 9, 2549

Hanhoun M., Montastruc L., Azzaro-Pantel C., Biscans B., Fr  lche M., Pibouleau L., 2011, *Chemical Engineering Journal*, 167, 50

Hendricks D., 2010, *Fundamentals of Water Treatment Unit Processes: Physical, Chemical, and Biological*, CRC Press, Boca Raton

Hixson A., Crowell J., 1931, *Industrial and Engineering Chemistry*, 23, 8, 923

Horenstein B., Hernandez G., Rasberry G., Crosse J., 1990, *Water Science and Technology*, 22, 12, 183

IUPAC, 2011, *Stability Constants Database*, Academic Software and the Royal Society of Chemistry

Jensen A., 1990, *Public Works*, 121, 4, 57

Johnson N. L., Balakrishnan N., 1995, *Continuous Univariate Distributions, Vol. 2 (Wiley Series in Probability and Statistics)*, Wiley-Interscience, New York

Jordan G., Rammensee W., 1996, *Geochimica et Cosmochimica Acta*, 60, 24, 5055

Kramer D. A., 2007, *Kirk-Othmer Encyclopedia of Chemical Technology, Volumes 1-26*, John Wiley and Sons, New York, 5th edn.

Lai R., Hudson H., Singley J., 1975, *Journal (American Water Works Association)*, 67, 10, 553

Lide D. R., 1991, *CRC Handbook of Chemistry and Physics*, 71st ed., CRC Press, Boca Raton

Linder P., Little J., 1985, *Talanta*, 32, 1, 83

- Liu J., Wang Y., Tian Q., Zhang S., 2012, *Thermochimica Acta*, 550, 27
- Loewenthal. R., Kornmuller U., van Heerden E., 1994, *Water Science and Technology*, 30, 12, 107
- Mamais D., Pitt P., Cheng Y., Loiacono J., Jenkins D., 1994, *Water Environment Research*, 66, 7, 912
- Mason J. B., 2011, *Goldman's Cecil Medicine*, 24, 225
- Melia P., Cundy A., Sohi S., Hooda P., Busquets R., 2017, *Chemosphere*, 186, 381
- Morel F. M., Hering J. G., 1993, *Principles and Applications of Aquatic Chemistry*, John Wiley and Sons, New York
- Musvoto E., Wentzel M., Ekama G., 2000, *Water Research*, 34, 1857
- Ohlinger K., Young T., Schroeder E., 1998, *Water Research*, 32, 12, 3607
- Ohlinger K., Young T., Schroeder E., 2000, *Journal of Environmental Engineering*, 126, 361
- Ollis D., 2018, *Frontiers in Chemistry*, 6, 1
- Parker D., Kaufman W., Jenkins D., 1971, *Journal Water Pollution Control Fed.*, 43, 1817
- Pokrovsky O., Schott J., 2004, *Geochimica et Cosmochimica Acta*, 68, 1, 31
- Pourbaix M., 1966, *Atlas of electrochemical equilibria in aqueous solutions*, Pergamon Press, Oxford, 1st edn.
- Pradita T., Aji B., Shih S., Sudiby, 2017, in *AIP Conference Proceedings*, 020044
- Rice E., Baird R., Eaton A., Clesceri L., 2012, *Standard Methods for the Examination of Water and Wastewater*, American Public Health Association, Washington DC, 22nd edn.
- Rocha S., Mansur M., Ciminelli V., 2004, *Journal of Chemical Technology and Biotechnology*, 79, 816
- Rude R., Coates P., Betz J., et al., 2010a, *Encyclopedia of Dietary Supplements*, Informa Healthcare, New York, New York, 2nd edn.
- Rude R., Ross A., Caballero B., Cousins R., Tucker K., Ziegler T., 2010b, *Modern Nutrition in Health and Disease*, Lippincott Williams and Wilkins, Baltimore, Massachusetts, 11th edn.
- Seager R., Acevedo A., Spill F., Zaman M., 2018, *Scientific Reports*, 8, 1
- Shampine L., Reichelt M., 1997, *SIAM Journal on Scientific Computing*, 18, 1
- Shand M. A., 2006, *The Chemistry and Technology of Magnesia*, John Wiley and Sons, New York, 5th edn.
- Smith R. M., Martell A. E., 1996, *Critical Stability Constants*, vol. 4, Plenum Press, New York

- Smithson G. L., Bakhshi N. N., 1969, *Canadian Journal of Chemical Engineering*, 47, 508
- Snoeyink V., Jenkins D., 1980, *Water Chemistry*, John Wiley & Sons, Inc., New York
- Speece R., 1996, *Anaerobic biotechnology for industrial wastewaters*, Archae Press, Nashville, Tennessee
- Sposito G., 2008, *The Chemistry of Soils*, Oxford University Press, Oxford, UK, 2nd edn.
- Stoltzenburg P., Capdevielle A., Teychene S., Biscans B., 2015, *Chemical Engineering Science*, 133, 9
- Stolzenburg P., Capdevielle A., Teychene S., Biscans B., 2015, *Chemical Engineering Science*, 133, 9
- Stumm W., Morgan J. J., 1994, *Aquatic Chemistry*, John Wiley and Sons, New York
- Talaiekhosani A., Bagheri M., Goli A., Talaei Khoozani M., 2016, *Journal of Environmental Management*, 170, 186
- Tchobanoglous G., Stensel H., Tsuchihashi R., Burton F., 2013, *Wastewater Engineering: Treatment and Resource Recovery*, 5th Edition, McGraw-Hill, New York
- Thomas J., Musso S., Prestini I., 2014, *Journal of the American Ceramic Society*, 97, 275
- Thomopoulos N. T., 2012, *Essentials of Monte Carlo Simulation*, Springer, New York
- Van Den Hul H., Lyklema J., 1967, *Industrial and Engineering Chemistry*, 23, 4, 500
- Vermilyea D. A., 1969, *Journal of the Electrochemistry Society*, 116, 9, 1179
- Walpole R., Myers R., Myers S., Ye K., 2002, *Probability and Statistics for Engineers and Scientists*, Prentice Hall, Upper Saddle River, NJ, 7th edn.
- Wang P., Li C., Gong H., Wang H., Liu J., 2011, *Ceramics International*, 37, 3365
- Wang Y., 2011, *The characterization of dry powder magnesium hydroxide suspensions using sedimentation, thermal analysis and other techniques*, Ph.D. thesis, University of Toledo
- Weber W., DiGiano F., 1996, *Process Dynamics in Environmental Systems*, Wiley-Interscience, Hoboken, NJ, 1st edn.
- Wieland E., Bernhard W., Stumm W., 1988, *Geochimica et Cosmochimica Acta*, 52, 1969
- Ye Y., Ngo H., Guo W., et al., 2017, *Science of the Total Environment*, 576, 159